THESIS FOR THE DEGREE OF DOCTOR OF PHILOSOPHY

Analysis of dc-network stability of VSC-based HVDC grids

GUSTAVO PINARES

Department of Energy and Environment
Division of Electric Power Engineering
CHALMERS UNIVERSITY OF TECHNOLOGY
Göteborg, Sweden 2016

Analysis of dc-network stability of VSC-based HVDC grids
GUSTAVO PINARES
ISBN: 978-91-7597-439-2

©GUSTAVO PINARES, 2016

Doktorsavhandlingar vid Chalmers Tekniska Högskola
Ny serie nr 4120
ISSN 0346-718X

Department of Energy and Environment
Division of Electric Power Engineering
SE-412 96 Göteborg
Sweden
Telephone +46(0)31-772 1000

Chalmers Bibliotek, Reproservice
Göteborg, Sweden 2016

To Karina ♡

Analysis of dc-network stability of VSC-based HVDC grids
GUSTAVO PINARES
Department of Energy and Environment
Chalmers University of Technology

Abstract

This thesis presents a modelling approach for the investigation of dc-network stability in HVDC grids. It consists on dividing the system under analysis into subsystems such that their individual impact on the stability of the overall system can be studied. This principle is first applied to a point-to-point HVDC system and then to a multi-terminal HVDC system.

Preliminary studies in a point-to-point HVDC system show that, under specific conditions, dc-network instabilities can occur. These are dependent on the dc-network resonance, the power flow direction and the Voltage Source Converter (VSC) control parameters. To further investigate these instabilities, the system is divided into the dc-network and the VSC subsystems. The VSC-subsystem can be interpreted as a frequency-dependent admittance whose conductance is positive or negative depending mainly on the power direction. The main characteristic of the dc-network subsystem is its resonance. Thus, if the dc-network resonance coincides with a negative conductance, there is a risk that the resonance becomes amplified, or unstable. Moreover, it has been found that decreasing the VSC ac-system strength and increasing the VSC control system delays turns the VSC conductance more negative, consequently, increasing the risk of instability. The dc-network subsystem is also studied, and it is found that high resonance peaks increase the risk of instability. A stability criterion is proposed, based on limiting the magnitude of the VSC subsystem transfer function to less than the inverse of the resonance peak around the resonance frequency.

The modelling approach is also applied to a multi-terminal HVDC system, where VSC subsystems are defined together with a dc-network subsystem. The main characteristic of the dc-network subsystem is that different resonances are localized in specific terminals. For example, it has been found in a four-terminal HVDC system that one resonance can take place in terminals 1 and 2, while another resonance, with a different frequency, can take place in terminals 3 and 4. This means that, for the first resonance, the VSCs connected to terminals 1 and 2 have the strongest impact on the system stability, and analogously for the second resonance. Moreover, the resonance peak at each terminal determines the level of influence of each VSC meaning that the VSC connected to the terminal with the highest resonance peak will have the greatest impact on the system stability. On the other hand, the VSC-subsystems are, in principle, similar as the ones defined for point-to-point HVDC systems, i.e. they can be interpreted as admittances whose conductances can be negative in certain conditions. Thus, instability occurs when resonances coincides with negative conductances. Finally, simulations and tests in a real time digital simulator show the validity of the theoretical findings of this thesis.

Index Terms: VSC, HVDC, Multi-terminal HVDC system, power dependent admittance, dc-network stability, resonance, passivity.

Acknowledgements

The financial support provided by the Chalmers Area of Advance Energy is gratefully acknowledged.

First of all, I would like to express my sincere gratitude to my main supervisor Prof. Massimo Bongiorno for his invaluable support during the development of this project. I appreciate very much his prompt response whenever his help was needed and also his trademarked meticulousness when reviewing manuscripts. Many thanks to my examiner, Prof. Torbjörn Thiringer for his contribution to this project, especially when finalizing this thesis. I would like to acknowledge as well my former project team, Prof. Lina Bertling-Tjernberg, Dr. Tuan Ahn Le, and Prof. Claes Breitholtz for their support during the initial two and a half years of this project.

My especial thanks also to Assoc. Prof. Subhashish Bhattacharya for hosting me as visiting scholar in the FREEDM center at North Carolina State University. I would like to acknowledge his talented student, Sayan Acharya, for developing the laboratory setup that I have used in this project, and for his help regarding practical matters of living in the US.

Thanks also to the colleagues at the division, especially my roommates Kalid and Yasir, for the warm work environment.

Muchas gracias a mi familia, especialmente a mis papás, Maximiliana y Julián, por su gran ejemplo y constante apoyo. Siempre los tengo presente, y esta pequeña obra esta también dedicada a ustedes!

Finally, my infinite gratitude goes to my lovely wife, Karina^2 Espejo, for her kindness, love and patience, and for teaching me to enjoy live.

Gustavo
Göteborg, Sweden
August 15th, 2016.

List of Abbreviations

CPL	Constant Power Load
dc-side PDA	dc-side Power Dependent Admittance
dc-side PDC	dc-side Power Dependent Conductance
dc-side PDS	dc-side Power Dependent Susceptance
DVC	DC-bus Voltage Controller
DVC$_i$	DC-bus Voltage Controller of the i-th VSC
DVC 1	DC-bus Voltage Droop Controller number 1
DVC 2	DC-bus Voltage Droop Controller number 2
DVC 3	DC-bus Voltage Droop Controller number 3
DVC-VSC	VSC that controls dc-bus voltage also called VSC in DVC mode
EMT	Electromagnetic Transient Program
HVDC	High Voltage Direct Current
large-DT	Large time step
LHP	Left-Half of the s-plane
LPF	Low Pass Filter
LPF$_i$	Low Pass Filter of the i-th VSC
MIMO	Multiple-Input Multiple-Output
MTDC	Multi-Terminal High Voltage Direct Current
OHL	Overhead Transmission Line
PC-VSC	VSC that controls active power also called VSC in PC mode
PDA	Power Dependent Admittance
PDC	Power Dependent Conductance
PDS	Power Dependent Susceptance
PF	Power Flow
PI	Proportional-Integral
PLL	Phase-Locked Loop

PLL$_i$	Phase-Locked Loop of the i-th VSC
PSC	Power Synchronization Control
pu	Per Unit
PWM	Pulse-Width Modulation
RF	Resonance Frequency
RHP	Right-Half of the s-plane
RP	Resonance Peak
RTDS	Real-Time Digital Simulator
SCR	Short Circuit Ratio
SISO	Single-Input Single-Output
small-DT	Small time step
TL	Transmission Line
VCC	Vector Current Controller
VCC$_i$	Vector Current Controller of the i-th VSC
VSC	Voltage Source Converters
VSC-HVDC	Voltage Source Converter based High Voltage Direct Current

List of Symbols

System bases

S_{base}	Power base
U_{acbase}	AC-side voltage base
E_{dcbase}	DC-side voltage base
Z_{acbase}	AC-side impedance base
L_{acbase}	AC-side inductance base
Z_{dcbase}	DC-side impedance base
L_{dcbase}	DC-side inductance base
C_{dcbase}	DC-side capacitance base
f_{base}	Frequency base

VSC$_i$ electrical variables

$\underline{u}_{\mathrm{c}i}$	Converter voltage in the $\alpha\beta$-frame
$\underline{u}_{\mathrm{g}i}$	Grid voltage in the $\alpha\beta$-frame
$\underline{u}_{\mathrm{s}i}$	AC source voltage in the $\alpha\beta$-frame
$\underline{u}_{\mathrm{c}i}^{dq}$	Converter voltage in the VSC *dq* frame
$\underline{u}_{\mathrm{g}i}^{dq}$	AC grid voltage in the VSC *dq* frame
$\underline{u}_{\mathrm{s}i}^{dq}$	AC source voltage in the VSC *dq* frame
$\underline{i}_{\mathrm{f}i}$	VSC phase reactor current in the $\alpha\beta$-frame
$\underline{i}_{\mathrm{s}i}$	AC source current in the $\alpha\beta$-frame
$\underline{i}_{\mathrm{f}i}^{dq}$	VSC phase reactor current in the VSC *dq* frame
$\underline{i}_{\mathrm{s}i}^{dq}$	AC source current in the VSC *dq* frame
e_i	VSC pole-to-neutral voltage
P_i	VSC dc-side power
i_i	VSC dc-side current
$P_{\mathrm{c}i}$	VSC ac-side power
$R_{\mathrm{s}i}$	AC source resistance
$L_{\mathrm{s}i}$	AC source inductance
$R_{\mathrm{f}i}$	VSC phase reactor resistance
$L_{\mathrm{f}i}$	VSC phase reactor inductance
$C_{\mathrm{f}i}$	VSC ac-side capacitor
$C_{\mathrm{vsc}i}$	VSC dc-side capacitor

VSC$_i$ controller variables

$k_{\mathrm{p}i}$	Proportional gain of VCC$_i$
$k_{\mathrm{i}i}$	Integral gain of VCC$_i$
$k_{\mathrm{pl}i}$	Proportional gain of PLL$_i$
$k_{\mathrm{il}i}$	Integral gain of PLL$_i$
$k_{\mathrm{e}i}$	Proportional gain of DVC$_i$
$k_{\mathrm{e}i}$	Integral gain of DVC$_i$
$k_{\mathrm{d}i}$	droop parameter of dc-bus voltage droop controllers
α_i	Closed-loop bandwidth of VCC$_i$
$\alpha_{\mathrm{PLL}i}$	Closed-loop bandwidth of PLL$_i$
$\alpha_{\mathrm{f}i}$	Closed-loop bandwidth of LPF$_i$
$\omega_{\mathrm{n}i}$	Closed-loop natural resonance frequency of DVC$_i$
ξ_i	Closed-loop damping factor of DVC$_i$
m_i^d	d-axis state that accounts for the integrator of VCC$_i$
m_i^q	q-axis state that accounts for the integrator of VCC$_i$
$n_{\mathrm{e}i}$	State that accounts for the integrator of DVC$_i$
$n_{\omega i}$	State that accounts for the integrator of PLL$_i$
$u_{\mathrm{gfil}i}^d$	Filtered voltage of $u_{\mathrm{g}i}^d$
$u_{\mathrm{gfil}i}^q$	Filtered voltage of $u_{\mathrm{g}i}^q$
$u_{\mathrm{c}i}^{d\mathrm{ref}}$	d-axis voltage reference generated by VCC$_i$
$u_{\mathrm{c}i}^{q\mathrm{ref}}$	q-axis voltage reference generated by VCC$_i$
$i_{\mathrm{f}i}^{d\mathrm{ref}}$	d-axis current reference of VCC$_i$
$i_{\mathrm{f}i}^{q\mathrm{ref}}$	q-axis current reference of VCC$_i$
e_i^{ref}	DC-bus voltage reference of DVC$_i$
$\theta_{\mathrm{g}i}$	Phase angle of $\underline{u}_{\mathrm{g}i}$ estimated by PLL$_i$
$\omega_{\mathrm{g}i}$	Angular speed of $\underline{u}_{\mathrm{g}i}$ estimated by PLL$_i$
τ_i	Control system delay of VSC$_i$

State space models

$\mathbf{x}_i$	State vector of VSC$_i$ state space model
$\mathbf{r}_i$	Input reference vector of VSC$_i$ state space model
$\mathbf{w}_i$	Delayed vector of VSC$_i$ state space model
$\mathbf{z}_i$	Output vector of VSC$_i$ state space model
$\mathbf{A}_i$	State matrix of VSC$_i$ state space model
$\mathbf{B}_{1i}$	Input matrix related to references of VSC$_i$ state space model
$\mathbf{B}_{2i}$	Input matrix related to the delayed vector of VSC$_i$ state space model
$\mathbf{B}_{1i}^{\mathrm{e}}$	Input matrix related to the dc-bus voltage of VSC$_i$ state space model
$\mathbf{C}_{1i}$	Output matrix related to i_i of VSC$_i$ state space model
$\mathbf{D}_{11i}$	Feedforward matrix (i_i) related to the input reference vector of VSC$_i$ state space model
$\mathbf{D}_{12i}$	Feedforward matrix (i_i) related to the input reference vector of VSC$_i$ state space model
$\mathbf{D}_{11i}^{\mathrm{e}}$	Feedforward matrix (i_i) related to the dc-bus voltage of VSC$_i$ state space model
$\mathbf{C}_{2i}$	Output matrix related to $\mathbf{z}_i$ of VSC$_i$ state space model
$\mathbf{D}_{21i}$	Feedforward matrix ($\mathbf{z}_i$) related to the input reference vector of VSC$_i$ state space model

$\mathbf{D}_{22i}$	Feedforward matrix ($\mathbf{z}_i$) related to the input reference vector of VSC$_i$ state space model
$\mathbf{D}^{\mathrm{e}}_{21i}$	Feedforward matrix ($\mathbf{z}_i$) related to the dc-bus voltage of VSC$_i$ state space model
$\mathbf{x}_{\mathrm{g}}$	State vector of the dc-cable state space model
$\mathbf{i}_{\mathrm{g}}$	Input vector of currents of the dc-cable state space model
$\mathbf{e}$	Output vector of voltages of the dc-cable state space model
$\mathbf{A}_{\mathrm{g}}$	State matrix of the dc-cable state space model
$\mathbf{B}_{\mathrm{g}}$	Input matrix the dc-cable state space model
$\mathbf{C}_{\mathrm{g}}$	Output matrix the dc-cable state space model
$\mathbf{x}$	State vector of the point-to-point VSC-HVDC state space model
$\mathbf{r}$	Input reference vector of the point-to-point VSC-HVDC state space model
$\mathbf{w}$	Delayed vector of the point-to-point VSC-HVDC state space model
$\mathbf{y}$	First output vector of the point-to-point VSC-HVDC state space model
$\mathbf{z}$	Second output vector of the point-to-point VSC-HVDC state space model
$\mathbf{A}$	State matrix of the point-to-point VSC-HVDC state space model
$\mathbf{B}_1$	Input matrix related to references of the point-to-point VSC-HVDC state space model
$\mathbf{B}_2$	Input matrix related to the delayed vector of the point-to-point VSC-HVDC state space model
$\mathbf{C}_1$	First output matrix of the point-to-point VSC-HVDC state space model
$\mathbf{D}_{11}$	First feedforward matrix of the point-to-point VSC-HVDC state space model
$\mathbf{D}_{12}$	First feedforward matrix of the point-to-point VSC-HVDC state space model
$\mathbf{C}_2$	Second output matrix of the point-to-point VSC-HVDC state space model
$\mathbf{D}_{21}$	Second feedforward matrix of the point-to-point VSC-HVDC state space model
$\mathbf{D}_{22}$	Second feedforward matrix of the point-to-point VSC-HVDC state space model

Transfer functions

s	Laplace operator
R_{t1}	Equivalent resistance $R_{\mathrm{f1}} + R_{\mathrm{s1}}$
L_{t1}	Equivalent inductance $L_{\mathrm{f1}} + L_{\mathrm{s1}}$
i_i^*	Component of the current injected by VSC$_i$ related to power
R_{10}	Equivalent resistance related to steady state VSC$_1$ power
R_{20}	Equivalent resistance related to steady state VSC$_2$ power
$G_1(s)$	DC network subsystem transfer function, option 1
$G_2(s)$	DC network subsystem transfer function, option 2
$G_3(s)$	DC network subsystem transfer function, option 2
$\widetilde{G}_0(s)$	Approximated transfer function of $G_3(s)$
$G_0(s)$	Approximated transfer function of $\widetilde{G}_0$
$F(s)$	VSC subsystem transfer function
$F_{\mathrm{c}}(s)$	Part of the VSC subsystem transfer function corresponding to VCC$_1$
$F_\theta(s)$	Part of the VSC subsystem transfer function corresponding to PLL$_1$

Discrete time VSC model

z	z-transform operator
k	Sampling instant
k-	Sampling instant k- $= k-1$
h	Sampling time
t^*	Time interval between 0 and h
$u_{\mathrm{c}i}^{kd*}$	Delayed d-axis voltage input of VSC$_i$
$u_{\mathrm{c}i}^{kq*}$	Delayed q-axis voltage input of VSC$_i$
$\omega_{\mathrm{g}i}^*$	Delayed angular speed estimated by PLL$_i$
$\mathbf{x}_i^{\mathrm{t}}$	State vector of VSC$_i$ continuous time state space model
$\mathbf{u}_{\mathrm{c}i}$	Input vector of VSC$_i$ continuous time state space model
$\mathbf{A}_i^{\mathrm{t}}$	State matrix of VSC$_i$ continuous time state space model
$\mathbf{B}_{\theta i}^{\mathrm{t}}$	Input matrix related to $\widetilde{\theta}_{\mathrm{g}i}$ of VSC$_i$ continuous time state space model
$\mathbf{B}_{\mathrm{uc}i}^{\mathrm{t}}(t^*)$	Input matrix related to $\mathbf{u}_{\mathrm{c}i}$ of VSC$_i$ continuous time state space model
$\mathbf{B}_{\omega i}^{\mathrm{t}}(t^*)$	Input matrix related to $\omega_{\mathrm{g}i}^*$ of VSC$_i$ continuous time state space model
$\mathbf{A}_i^{\mathrm{k}}$	State matrix of VSC$_i$ discrete time state space model
$\mathbf{B}_{\theta i}^{\mathrm{k}}$	Input matrix related to $\widetilde{\theta}_{\mathrm{g}i}$ of VSC$_i$ discretized state space model
$\mathbf{B}_{\mathrm{uc}i}^{\mathrm{k}}$	Input matrix related to $\mathbf{u}_{\mathrm{c}i}$ of VSC$_i$ discretized state space model
$\mathbf{B}_{\omega i}^{\mathrm{k}}$	Input matrix related to $\omega_{\mathrm{g}i}^*$ of VSC$_i$ discretized state space model
$\mathbf{A}_{\mathrm{k}i}$	State matrix of the closed-loop VSC$_i$ discretized state space model
$\mathbf{B}_{\mathrm{k}i}$	Input reference matrix of the closed-loop VSC$_i$ discretized state space model
$\mathbf{B}_{\mathrm{k}i}^{\mathrm{e}}$	Input matrix related to the dc-bus voltage of the closed-loop VSC$_i$ discretized state space model
$\mathbf{C}_{\mathrm{k}i}$	Output matrix of the closed-loop VSC$_i$ discretized state space model
$\mathbf{D}_{\mathrm{k}i}$	Feedforward matrix of the closed-loop VSC$_i$ discretized state space model
$\mathbf{D}_{\mathrm{k}i}^{\mathrm{e}}$	Feedforward matrix related to the dc-bus voltage of the closed-loop VSC$_i$ discretized state space model

Resonance related variables

ω_i^{r}	Resonance frequency of the i-th resonance
Z_{peak}	Resonance peak
γ	Frequencies around the resonance

MTDC stability analysis

$\mathbf{Z}(s)$	dc-network transfer matrix
$\mathbf{Y}(s)$	VSC subsystem transfer matrix
z_{ij}	ij-elements of matrix $\mathbf{Z}(s)$
y_i	i-diagonal elements of matrix $\mathbf{Y}(s)$
G_{i0}	Equivalent conductance related to the steady state VSC$_i$ power
$F_{\mathrm{e}i}$	Transfer function with input e_i^{ref} and output i_i^* of DVC-VSC$_i$
$F_{\mathrm{r}i}$	Transfer function with input P_i^{ref} and output i_i^* of PC-VSC$_i$

$\mathcal{S}$	Characteristic polynomial of the MTDC system transfer function
$\mathcal{T}$	Polynomial defined as $\mathcal{S} - 1$
$\mathbf{Z}$-terms	Terms defined as determinant of all distinct square submatrices of $\mathbf{Z}$
$\mathbf{Y}$-terms	Each y_i
z_{ii}	Impedance seen from the i-th dc-bus
γ_{ij}	Term defined as the determinant of 2×2 submatrices of $\mathbf{Z}$
γ_{ijk}	Term defined as the determinant of 3×3 submatrices of $\mathbf{Z}$
Z_{C}	Characteristic impedance of a TL
Γ_{H}	Propagation factor of a TL
z_{ii}^{cr}	Encirclement defined by z_{ii}
$\gamma_{ij}^{\mathrm{cr}}$	Encirclement defined by γ_{ij}
$\gamma_{ijk}^{\mathrm{cr}}$	Encirclement defined by γ_{ijk}
$\mathcal{T}_{ii}^{\mathrm{cr}}$	Encirclement defined by $\mathcal{T}$
z_{ii}^{pk}	Resonance peak of z_{ii}
$\gamma_{ij}^{\mathrm{pk}}$	Resonance peak of γ_{ij}
δ	Number that indicates the risk of instability in an MTDC system

Contents

Chapter 1

Introduction

1.1 Background and motivation

Since the first Voltage Source Converter (VSC) based HVDC link, commissioned in 1997 [1] to interconnect the North and the South regions of Gotland, VSC technology has improved tremendously in terms of power ratings, loss reduction, and harmonic performance [2]. An example of that is the development of modular multilevel VSC topologies [3–5], which has allowed to decrease losses to levels comparable to thyristor-based HVDC systems (around 1% [4]). From a power system operation perspective, VSCs have advantageous controllability features compared to thyristor-based converters, such as independent control of active and reactive power [3]. It is also recognized that VSC-based HVDC (VSC-HVDC) systems are suitable for the interconnection of weak ac grids [2, 6]. Moreover, VSCs allow power flow in both direction without the need of reversing the dc-system voltage polarity [2] and can be operated without the need of communications [2]. All these attributes make VSCs convenient for more complex HVDC structures, such as the multi-terminal HVDC (MTDC) systems proposed in [7–12]. Consequently, in recent years, VSC-HVDC systems have been proposed as a solution for the integration of renewable energy sources located far away from the consumption centres [7, 13] and for the integration of electricity markets distributed over large geographical areas [8, 9].

An HVDC project is justified when this option is the most economical for transmitting power between two areas. Aside from its mission of transmitting power, VSC-HVDC systems are also able to contribute to the enhancement of the dynamic performance of existing ac systems. Examples of works that show the use of VSC-HVDC systems for power oscillation damping, and for ac voltage support are [14, 15]. However, it is recognized that VSC do not only bring advantages but also challenges. Good examples are reported in [16, 17] where undesired interactions between VSCs and the connecting ac systems are studied. Regarding the study of dc-network dynamics, only a few examples can be found in the literature for point-to-point VSC-HVDC system. One good example is [18], which investigates dc-network stability in a point-to-point HVDC system through eigenvalue analysis. In this work it is found that instability related to the dc-network resonance, operating points and VSC control parameter can occur. On the other hand, a large number of studies can be

found for more complex dc-network structures, such as dc microgrids and MTDC systems. In order to get an idea of possible dynamic issues that can occur in dc-networks, and to give a frame around the overall scope of the thesis, a brief literature review is presented next.

1.1.1 Dynamic issues in dc microgrids

Multi-converter power electronic systems, in the form of dc microgrids, has been a subject of research for some years. In [19], for instance, definitions and applications of multi-converter power electronics systems are presented. Suggestions for dc microgrids configurations for automotive power systems, electric and hybrid vehicles, aircraft power systems, and space power systems are presented as examples. As shown in Figure 1.1, typically, a dc microgrid is composed of a number of converters connected to a common bus. Those converters interface either power sources or loads or can be used to interconnect systems of different voltage levels. From the dynamics point of view, challenges in multi-converter systems, as stated in [19], ranges from system modelling, dynamic assessment and control.

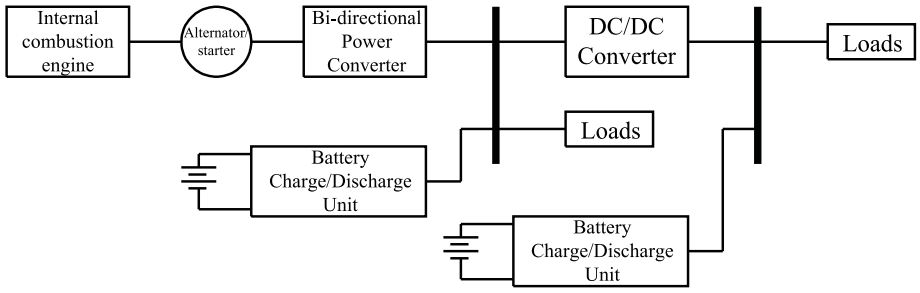

Figure 1.1: Architecture of a series hybrid power electronic system for automotive applications [19].

Constant Power Loads (CPLs) have been recognized as the main source of instability in dc microgrids [19–25]. As pointed out in [21], a CPL can be a DC/DC converter that tightly regulates its output voltage with a resistive load connected to its output. In this case, since the output voltage is maintained constant, the output current is constant as well, therefore, seen from the dc bus, the dc/dc converter acts as a CPL. Although the instantaneous impedance of a CPL is positive, the incremental impedance is negative. Thus, if there is a decrease in voltage at the input dc bus, there will be an increase of current drawn from the converter in order to maintain a constant power at the output bus. As an example, stability of a buck converter supplying power to a CPL is investigated in [20]. In the analysis, the maximum power that a CPL can consume is found to be related to the size of the inductor and capacitor filters, and to the amount of resistive loads connected to the converter. Another interesting work is [23] where load characteristics are investigated in dc microgrids. The load dynamics is studied taking into consideration more details instead of the sole simplification of a CPL. It is found that a load can have poles and zeros located in the Right-Half of the s-plane (RHP) that impose limitations in the control system. A load with unstable poles needs feedback to stabilize the system, while a non-minimum phase load can cause instability if a feedback gain is high.

Frequency domain analysis is usually applied to study stability in dc microgrids. For instance, *immittance* analysis is proposed in [25] and [24]. The method consists, first, on calculating the source impedance Z_S and the load admittance Y_L (see Figure 1.2) as a function of frequency for all operating points. Then, according to Nyquist stability criterion, the contour defined by $Z_S Y_L$ should not clockwise encircle the point -1. If Nyquist stability criterion is not fulfilled, either Z_S or Y_L must be modified.

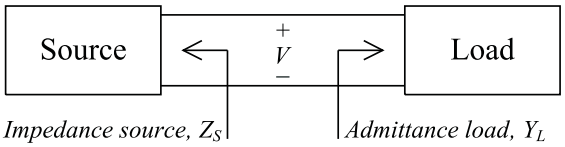

Figure 1.2: Equivalent source and load of a dc microgrid [24].

Although there are significant differences compared with HVDC systems, such as power and voltage ratings, there are similarities on the electrical configuration and control structure. The following aspects, where dc microgrids and HVDC system are comparable, are summarized:

1. The studied dc microgrids are converters connected to a common dc bus, while the converters in HVDC systems are interconnected through dc cables or OHL. However, the filter configuration (composed of inductors and capacitors) of the dc microgrid's converter resembles the dc cables and OHL of HVDC systems;

2. In dc microgrids, CPLs are considered as the main source on instability. Furthermore, the converter control structure and the load characteristic can have destabilizing forms such as poles and zeros in the RHP. In HVDC systems, if the control system and the converter dynamics are considered, the load (inverter) or the source (rectifier) connected to the dc grid (cable or OHL) can also have destabilizing forms in the dc side;

3. Methods developed for the analysis of the dc microgrids, based on the averaging techniques, eigenvalue analysis, and frequency domain analysis can be adapted to HVDC systems.

1.1.2 DC network dynamics in multi-terminal VSC-HVDC

An MTDC system can be defined as an HVDC system where more than two VSCs are interconnected through a common dc-network. In such a system the risk of undesired interactions increases since a number of complex elements will be operating concurrently. Thus, the increased interest in MTDC systems in recent years has also led to an increase of research activities in the area of control intereaction and system stability. Examples of that are works, such as [26–29], which deal with the study of the stability of MTDC systems from a broad perspective. In these works, MTDC systems are modelled and the impact of VSC controller parameters on the system stability is determined through eigenvalue analysis. The risk of dc-side resonances is recognized in [11, 12], where it is mentioned that low

frequency dc-side resonances might introduce issues in complex HVDC structures such as MTDC systems. Examples of more recent studies are [30–35], where the dynamic performance of MTDC is investigated from various perspectives. For instance, [30] investigates the stability of the Cigré dc-grid benchmark system, and oscillatory instabilities related to the dc-bus voltage controllers are found. In addition, [31,32] proposes a method to quantify the level of interaction among VSCs, and situations where poorly damped oscillations take place are identified. Regarding frequency domain analysis, [33] applies impedance analysis, and it is shown that, with a VSC connected to a weak ac system, instability in the form of dc-side oscillations might occur. In, [34] frequency domain analysis has been applied to design dc-bus voltage droop controller parameters considering the dc and ac-side dynamics. Resonance peaks (RPs) in the defined dc-bus voltage error transfer function have been found and damping controllers have been designed. In [35], the impact of a series inductor introduced by a dc breaker is studied and it is shown that large inductances can introduce instability originated from dc-side resonances.

The following can be summarized with regards dc-network dynamics of MTDC systems:

1. There is a risk of instability originated from the dc side of the system. In some works unstable cases are not identified, but poorly damped oscillations in the system's dc-side are reported instead. The results presented in the reviewed works indicated that the instability is related to the dc-side resonance phenomenon, thus, the dc-network configuration has a major impact on the system dynamic performance

2. Instability is also related to the design of the dc-bus voltage controller. It has been seen in some studies that the size of the proportional gain of the some controllers, such as the dc-bus voltage droop setting, also influences on the system dynamic performance. Too low or too high gains can turn the system unstable;

3. Eigenvalue and frequency domain analysis have been applied to show theoretically that poor dc-network dynamic performance might take place under certain scenarios. However, to the best of the author's knowledge, no studies with the aim of explaining the mechanisms that leads to this poor performance, or even instability, has been carried out.

The reviewed studies indicate that undesirable dynamic behavior originated in the dc-network can take place in any type of dc system, especially when considering complex structures. In HVDC systems, it can be argued that dc-side dynamic issues have not been visible since, up to date, most of the existing installations are point-to-point HVDC links. In such systems, the dc-side configuration, composed of cables or Overhead Transmission Lines (OHL), is rather fixed. So, once a dc-side related problem is detected and counteractions are taken, it will be very rare that it takes place again. However, this is not the case in an MTDC system, where several elements are interconnected. In this type of systems, the dc-network configuration is variable since transmission lines (TLs) might be out of service due to maintenance or new TLs can be put into service. In such a case, even if a dc-side related problem is solved for one configuration, it cannot be guaranteed that the implemented solution works if the configuration changes. Moreover, TL transients, which are usually neglected in ac system studies, have to be considered with regards to dc-network dynamic analysis. This is due to the fact that the time response of a VSC is in the order

of the TL time constants. Therefore, in this kind of studies, there is a need to investigate the conditions in which dc-network related instabilities occur and to identify the causes of the unstable cases so that mitigation measures can be more effectively proposed. Thus, this thesis develops a conscientious analysis regarding dc-network stability, with particular focus on dc-network resonances.

1.2 Purpose of the thesis and main contributions

The purpose of this thesis is to explain the mechanisms that lead to instabilities related to dc-network resonances in HVDC systems. To the best author's knowledge, the following are the main contribution of this work:

1. From the dc-side stability point of view, the main factors that limit the power transfer in a point-to-point VSC-HVDC system has been established through eigenvalue analysis. Along with this, a general procedure to obtain a state space model of a generic VSC-HVDC system has been provided (Paper I);

2. A method based on defining subsystems in a point-to-point VSC-HVDC system has been proposed to explain the mechanism that causes dc-network instabilities (Paper VI). Moreover, expressions useful to explain dc-network instabilities in HVDC systems where VSCs are connected to infinitely strong and weak ac sources have been derived (Paper II and III, respectively);

3. The definition of a dc-side power dependent admittance, used to demonstrate the role of VSCs in the system stability has been proposed. Moreover a method to "measure" this dc-side power dependent admittance in Electromagnetic Transient (EMT) models has been presented (Paper IV);

4. The impact of the dc-network configuration has been established. Moreover, the role of dc-side Resonance Peaks (RPs) on the system stability have been explained. A conservative stability condition that can be used as a design criterion has been provided for point-to-point VSC-HVDC (Paper V and VII);

5. DC-network resonance related instabilities in MTDC systems are theoretically explained. Conservative stability conditions are provided (Paper VIII). The findings are validated through tests in a Real Time Digital Simulator (RTDS) (Paper IX).

1.3 Structure of the thesis

This thesis "attempts" to be a summary of the work presented in the appended articles, although details are not spared for the sake of self completeness. Chapter 1 provides the introduction to the topic, where the background, the motivation, the purpose, and contributions of the thesis are presented. In Chapter 2, a preliminary analysis of the dc-network dynamics is performed for a point-to-point VSC-HVDC system and through eigenvalue analysis. In Chapter 3, a modelling approach is presented, where the impact of the dc-

network and the VSCs connected to it can be clearly appreciated. A VSC dc-side power dependent admittance is defined and the impact of different factors on this admittance is investigated. Chapter 4 presents an analysis carried out through Nyquist stability criterion that shows the impact of the dc-side RPs. Moreover, the impact of different dc-network topologies on the system stability is also investigated in this chapter. In Chapter 5, the method is extended to MTDC systems and it clearly reveals the way how VSCs contribute to instability. Chapter 6 presents verifications of the findings in Chapter 5 through tests in RTDS. Finally, the thesis ends with conclusions and ideas for future work, presented in Chapter 7.

1.4 List of publications

The articles originated from this research work are the following

I. G. Pinares, T. A. Le, L. Bertling-Tjernberg, C. Breitholtz, A. Edris, "On the analysis of the dc dynamics of multi-terminal VSC-HVDC systems using small signal modeling," presented at *IEEE Power Tech conference*, Grenoble, France, 16-20, June, 2013.

II. G. Pinares, T. A. Le, L. Bertling-Tjernberg, C. Breitholtz, "Analysis of the dc Dynamics of VSC-HVDC Systems Using a Frequency Domain Approach," presented at *IEEE Asia Pacific Power Energy Engineering Conference*, Hong Kong, China, 8-11, December, 2013.

III. G. Pinares, "Analysis of the dc Dynamics of VSC-HVDC Systems Connected to Weak AC Grids Using a Frequency Domain Approach," presented at *Power Systems Computation Conference (PSCC)*, Wroclaw, Poland, 18-22, August, 2014.

IV. G. Pinares, M. Bongiorno, "Definition of a Voltage-Source Converter dc-side admittance and its impact on dc-network stability," presented at th *International Conference on Power Electronics (ECCE-Asia)*, Seoul, South Korea, 1-5, June, 2015.

V. G. Pinares, M. Bongiorno, "Analysis and mitigation of instabilities originated from dc-side resonances in VSC-HVDC systems," presented at *IEEE Energy Conversion Congress and Exposition*, Montreal, QC, 20-24, September, 2015.

VI. G. Pinares, M. Bongiorno, "Modeling and Analysis of VSC-Based HVDC systems for DC network Stability Studies," published at *IEEE Transaction of Power Delivery*, Vol. 31, No. 2, pp. 848-856, April, 2016.

VII. G. Pinares, M. Bongiorno, "Analysis and mitigation of instabilities originated from dc-side resonances in VSC-HVDC systems," published at *IEEE Transactions on Industry Applications*, Vol. 52, No. 4, pp. 2807-2815, July, 2016.

VIII. G. Pinares, M. Bongiorno, "Investigation of dc-network resonance-related instabilities in VSC-based multi-terminal HVDC systems. Part I: Theoretical Background," submitted to *IEEE Transactions on Power Delivery*, 2016.

IX. G. Pinares, S. Acharya, M. Bongiorno, S. Bhattacharya, "Investigation of dc-network resonance-related instabilities in VSC-based multi-terminal HVDC systems. Part II: RTDS verifications," submitted to *IEEE Transactions on Power Delivery*, 2016.

The author has also contributed with the following papers not included in this thesis:

1. G. Pinares, M. Bollen, "Understanding the Operation of HVDC Grids," presented at Cigré International Symposium The Electric Power System of the Future, Integrating supergrids and microgrids, Bologna, Italy, 13-15, September, 2011.

2. G. Pinares, N. Ullah, P. Brunnegard, M. Lindgren, "Fault Analysis of a Multilevel-Voltage-Source-Converter-based Multi-terminal HVDC system," presented at Cigré HVDC Colloquium, San Francisco, March 7, 2012.

Chapter 2

Preliminary study in a point-to-point VSC-HVDC system

In the previous chapter, investigations carried out by different authors show that instability related to dc-network dynamics and operating conditions can take place in various type of dc network. This is further investigated in this chapter, initially through time domain simulations in a point-to-point HVDC system and then through eigenvalue analysis. The impact of different factors are studied, such as: operating points, controller parameters and electrical characteristics on the system's ac and dc sides to which VSCs are connected. This chapter is based on the work performed in [36] and in the appended papers I and VI.

2.1 System description

The symmetrical monopole point-to-point VSC-HVDC system, illustrated in Figure 2.1, is studied in this chapter. In such a system, typically, the sending VSC is set to control the voltage of its dc-bus while the receiving VSC is set to control the transmitted power. Throughout this thesis, however, VSC_1 controls its dc-bus voltage while VSC_2 controls active power, regardless of the power direction. The VSCs ratings as well as the system bases are shown in Table 2.1. Moreover, the VSCs are interconnected through a dc cable whose parameters are presented in Table 2.2.[1]

2.1.1 Electrical configuration

The i-th VSC station (VSC_i)[2] configuration assumed throughout this thesis is as depicted in Figure 2.2. In the ac side, VSC_i is composed of a phase reactor, a converter transformer and a capacitor.[3] Moreover, the ac system to which the VSC station is connected is rep-

[1] The dc cable parameters presented in Table 2.2 correspond to the lumped parameters Π-model of the cable shown in Figure 4.4 for a frequency of 50 Hz.

[2] In this thesis, subindex "i" means that the variable or controller is related to the i-th VSC.

[3] A description of a typical VSC station with the functionality of each component can be found in [2,6,36].

resented as a impedance. Likewise, in the dc side, VSC_i has a capacitor. The VSC type studied throughout this thesis is a two-level converter that generates an ac voltage through a sinusoidal Pulse Width Modulation (PWM) method, as explained in [36]

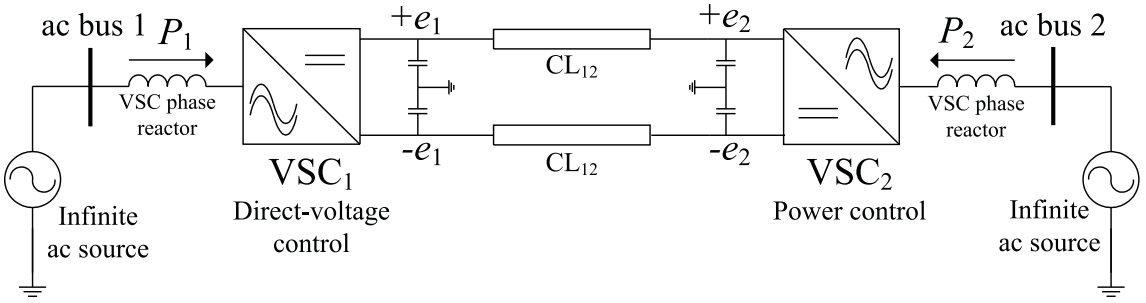

Figure 2.1: Point-to-point VSC-HVDC system under study.

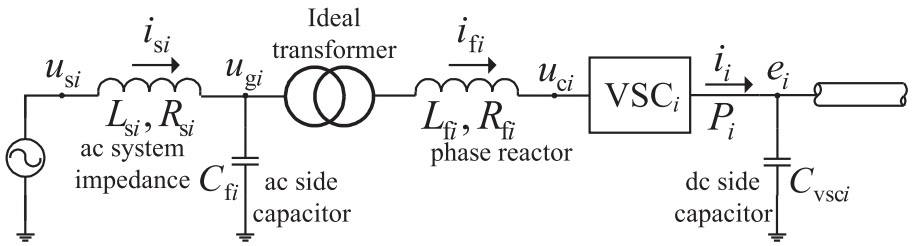

Figure 2.2: Electrical configuration of VSC_i.

Table 2.1: VSCs ratings and system bases

Parameter	Value
VSC rated power (S_{base})	600 MW
VSC rated ac-bus voltage (U_{acbase})	300 kV
VSC rated dc-bus voltage (E_{dcbase})	$\pm$300 kV
AC impedance base (Z_{acbase})	150 Ω
AC inductance base (L_{acbase})	0.477 H
DC impedance base (Z_{dcbase})	300 Ω
DC inductance base (L_{dcbase})	0.954 H
DC capacitance base (C_{dcbase})	10.61 μF
Nominal frequency (f_{base})	50 Hz

The value of the different components are presented in Table 2.3. The following considerations have been taken for the selection of the parameters: the transformer is considered ideal, i.e. it has a zero short circuit impedance, with a transformation ratio of 300 kV/300 kV. Then, the transformer impedance is accounted in the inductance and resistance values of the phase reactor. That is, considering a typical transformer reactance of 0.1 pu, plus a typical VSC phase reactor reactance of 0.15 pu [37], the value of $L_{\text{f}i}$ is 0.25 pu. The resistance is assumed as 1 % of the reactance. The dc-side converter capacitor is selected such that the charging time constant (defined in [36]) is 5 ms.[1] The value of the ac side

[1] In [6] a charging time constant of 2 ms is while suggested while 30-40 ms is recommended in [4].

Table 2.2: CL_{12} Cable Data (calculated for a cable such as the one in Figure 4.4 for 50 Hz)

Parameter	Value
Cable cap. per length, $c_{1,2}$	0.207 μF/km (0.0195 pu/km)
Cable ind. per length, l_{12}	0.189 mH/km ($1.975 \cdot 10^{-4}$pu/km)
Cable res. per length, r_{12}	0.038 Ω/km ($1.253 \cdot 10^{-4}$pu/km)

Table 2.3: VSC_i component parameters

Parameter	**Value**
Reactor inductance, $L_{\mathrm{f}i}$	119.4 mH (0.25 pu)
Reactor resistance, $R_{\mathrm{f}i}$	0.375 Ω (0.0025 pu)
Converter capacitor, $C_{\mathrm{vsc}i}$	33 μF (3.14 pu)

capacitor and the ac side system impedance are to be specified later in the thesis, since they are varied to evaluate different conditions.

2.1.2 Control system

The control loops of VSC_i are depicted in Figure 2.3. The core of the control system is the Vector Current Controller (VCC_i). In this controller, three-phase ac quantities are transformed into two-component dc quantities, in the so-called *rotating dq frame*, with the *d* axis aligned to the rotating voltage vector $\underline{u}_{\mathrm{g}i}$.[1] In this way, active power can be controlled independently from reactive power through the control of the phase reactor current in the *d* axis, $i_{\mathrm{f}i}^{d}$, and in the *q* axis, $i_{\mathrm{f}i}^{q}$, respectively. As illustrated in Figure 2.3, VCC_i is a Proportional-Integral (PI) controller with a voltage feedforward of $\underline{u}_{\mathrm{g}i}^{dq}$ and a current cross-coupling compensation of $\underline{i}_{\mathrm{f}i}^{dq}$. The angle of the voltage $\underline{u}_{\mathrm{g}i}$, $\theta_{\mathrm{g}i}$, required for the *dq* transformation, is estimated through the Phase-Locked Loop (PLL_i) depicted in Figure 2.3. PLL_i is also a PI controller and it is based on [38,39]. A dc-bus Voltage Controller (DVC_i), depicted in Figure 2.3, is implemented for a VSC that controls its dc-bus voltage.[2] The DVC_i is an outer loop and it consists of a PI controller whose output is the reference $i_{\mathrm{f}i}^{d\mathrm{ref}}$ that goes to the VCC_i. Note also that voltages $u_{\mathrm{g}i}^{d}$ and $u_{\mathrm{g}i}^{q}$ are pre-processed through a Low-Pass Filter (LPF_i).

In this thesis, active and reactive power controller loops are not implemented for the sake of simplicity. Instead, active power and reactive power are directly controlled through the references $i_{\mathrm{f}i}^{d\mathrm{ref}}$ and $i_{\mathrm{f}i}^{q\mathrm{ref}}$, respectively, as depicted in Figure 2.3. The controller parameters are presented in Table 2.4. For VCC_i the PI gains are selected as [40]

$$k_{\mathrm{p}i} = \alpha_i L_{\mathrm{f}i} \quad \text{and} \quad k_{\mathrm{i}i} = \alpha_i R_{\mathrm{f}i} \tag{2.1}$$

[1] Underlined variables without superscript denote two-component vectors in the so-called stationary $\alpha\beta$ frame. Underlined variables with a dq superscript denote two-component vectors in the *dq* frame. For instance $\underline{z}^{dq} = z^d + \mathrm{j}z^q$.

[2] A VSC that controls its dc-bus voltage is called in this thesis DVC-VSC or VSC in DVC mode. Likewise, a VSC that controls active power is called PC-VSC or VSC in PC mode.

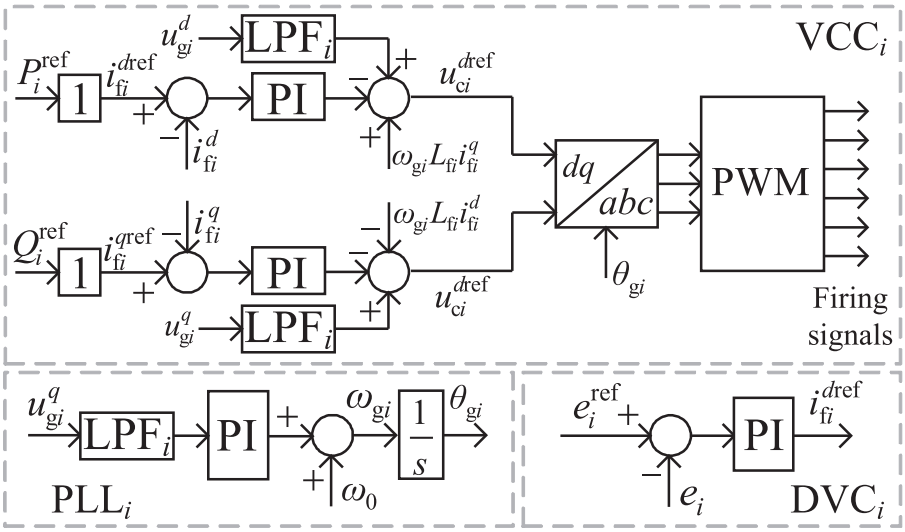

Figure 2.3: VSC control loops.

where α_i is the closed-loop bandwidth of VCC$_i$, selected as 4 pu. The PI gains of PLL$_i$ are selected as [40]

$$k_{\text{pl}i} = 2\alpha_{\text{pl}i} \quad \text{and} \quad k_{\text{il}i} = \alpha_{\text{pl}i}^2 \tag{2.2}$$

where $\alpha_{\text{pl}i}$ is the closed-loop bandwidth of PLL$_i$, selected as 0.1 pu. The PI gains of DVC$_i$ are selected as [41]

$$k_{\text{pe}i} = \sqrt{1.5}\,\omega_{\text{n}i}\xi_i C_{\text{vsc}i}\frac{U_{\text{acbase}}}{E_{\text{dcbase}}} \quad \text{and} \quad k_{\text{ie}i} = \frac{\sqrt{1.5}}{2}\omega_{\text{n}i}^2 C_{\text{vsc}i}\frac{U_{\text{acbase}}}{E_{\text{dcbase}}} \tag{2.3}$$

where $\omega_{\text{n}i}$ and ξ_i are the the closed-loop natural oscillation frequency and the damping factor of DVC$_i$.[1] Observe that the DVC$_i$ gains $k_{\text{pe}i}$ and $k_{\text{ie}i}$ are varied in later tests.

Table 2.4: Controller parameters

Parameter	**Value [pu]**
VCC$_i$ Prop. gain ($k_{\text{p}i}$)	1.00
VCC$_i$ Int. gain ($k_{\text{i}i}$)	0.01
PLL$_i$ Prop. gain ($k_{\text{pl}i}$)	0.20
PLL$_i$ Int. gain ($k_{\text{il}i}$)	0.01
LPF$_i$ bandwidth ($\alpha_{\text{f}i}$)	4.00

Finally, the output of VCC$_i$ are transformed to three-phase voltage references and pulses are generated through the PWM block as shown in Figure 2.3.

[1] Expressions for $k_{\text{pe}i}$ and $k_{\text{ie}i}$ have been derived assuming that the VSC is connected only to a capacitor in its dc-side and the the inner VCC is much faster than the DVC.

2.2 Preliminary study

The purpose of this section is to explore the impact of different operating points, controller parameters, and dc-network topologies on the stability of a point-to-point VSC-HVDC system through time domain simulations. The study is performed in the system described in Section 2.1. Switching models of two-level converters are implemented for the VSCs. The dc-cable is modelled as a lumped-parameter Π-section with the data presented in Table 2.2. The ac sources to which VSC_1 and VSC_2 are connected are assumed to be infinitely strong (i.e. $L_{si} = 0$ and $R_{si} = 0$), thus, the unstable cases found are not related to the ac system strength neither the PLL dynamics.

The impact of the operating point is evaluated through varying the power flow in both directions. The impact of controller parameters is evaluated for two sets of values of the DVC_1 PI gains, k_{pe1} and k_{ie1}, and the impact of the dc-network configuration is evaluated for different lengths of the dc cable. The studied cases are as follow:

Case 1.1 Ramp up of power from zero to 600 MW with the direction of the power from VSC_1 to VSC_2, with $k_{\text{pe1}} = 4.62$ pu, $k_{\text{ie1}} = 0.31$ pu and the cable length is 50 km;

Case 1.2 Ramp up of power from zero to 600 MW with the direction of the power from VSC_2 to VSC_1, with $k_{\text{pe1}} = 4.62$ pu, $k_{\text{ie1}} = 0.31$ pu and the cable length is 50 km;

Case 2.1 Repetition of Case 1.1 with increased gains k_{pe1} = 9.23 pu and k_{ie1} = 1.23 pu;

Case 2.2 Repetition of Case 1.2 with increased gains k_{pe1} = 9.23 pu and k_{ie1} = 1.23 pu;

Case 3.1 Repetition of Case 2.1 with a cable length of 100 km;

Case 3.2 Repetition of Case 2.2 with a cable length of 100 km.

The results are shown in Figures 2.4, 2.5, and 2.6 where the dc-bus voltage, e_1, and the active power, P_1, are plotted for each case. Figure 2.4 shows Cases 1.1 and 1.2 where the instant before reaching 600 MW (in both directions) is shown. It can be seen that the system is able to reach the final setpoint without inconveniences. Figure 2.5 shows Cases 2.1 and 2.2, where k_{pe1} and k_{ie1} have been increased. The figure shows that, in Case 2.1, the system turns unstable when the power reaches almost 600 MW, with the direction of the power from VSC_1 to VSC_2. However, when the power flows in the opposite direction, the system reaches 600 MW without problems. Finally, the results from the Cases 3.1 and 3.2 are shown in Figure 2.6. It can be seen that the unstable case that occurs in Case 2.1 with increased DVC gains, does not occur in Case 3.1 when the dc cable is longer.

Figure 2.7 depicts a zoomed picture of voltage e_1 between 2.20 s and 2.21 s. Oscillations can be observed in the figure with a period of approximately 2.8 ms, which corresponds to a frequency of around 357 Hz. Considering a lossless Π model for the dc cable, the Resonance Frequency (RF) is given by

$$f_0 = \frac{1}{2\pi\sqrt{L_{12}\frac{C_{\text{eq}}}{2}}} \tag{2.4}$$

where L_{12} is the equivalent inductance of the cable, and $C_{\text{eq}} = C_1 + C_{\text{vsc1}}$ is the equivalent cable capacitance plus the VSC capacitor per pole. For a cable length of 50 km, L_{12} is 9.43 mH, and C_{eq} is 43.67 µF. With these values, the RF, f_0, is around 350.7 Hz, which is very close to the frequency found from Figure 2.7. This coincidence indicates that instability might be related to the dc-network resonance and that it is triggered by the VSC through a mechanism investigated in the upcoming sections.

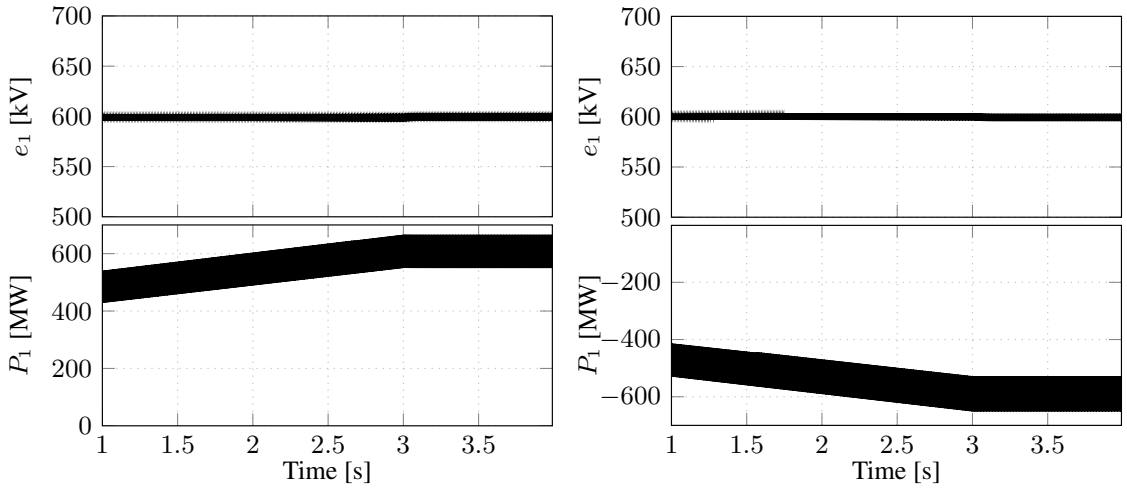

Figure 2.4: Simulation results of Case 1. (a) VSC_1 dc-bus voltage and power for Case 1.1. (b) VSC_1 dc-bus voltage and power for Case 1.2

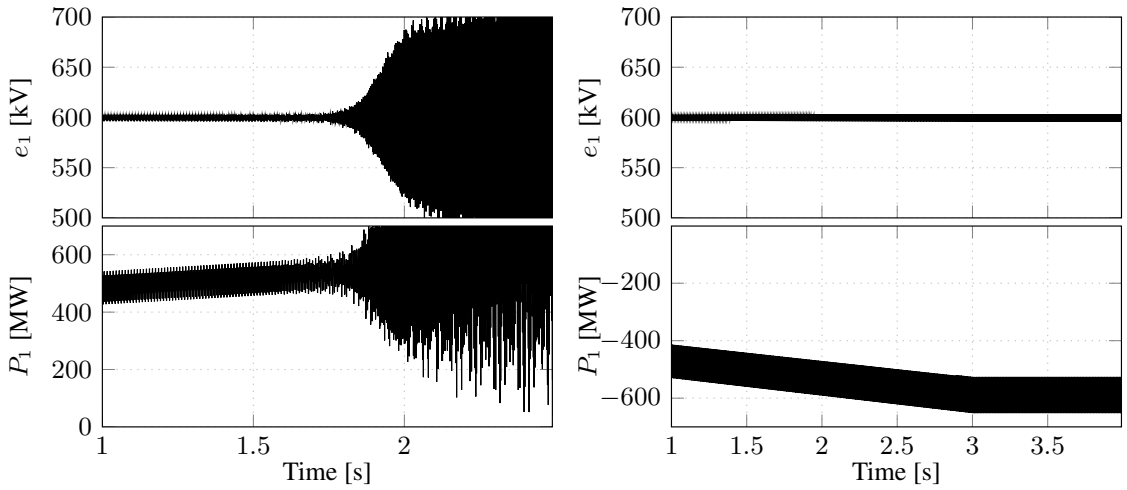

Figure 2.5: Simulation results of Case 2. (a) VSC_1 dc-bus voltage and power for Case 2.1. (b) VSC_1 dc-bus voltage and power for Case 2.2

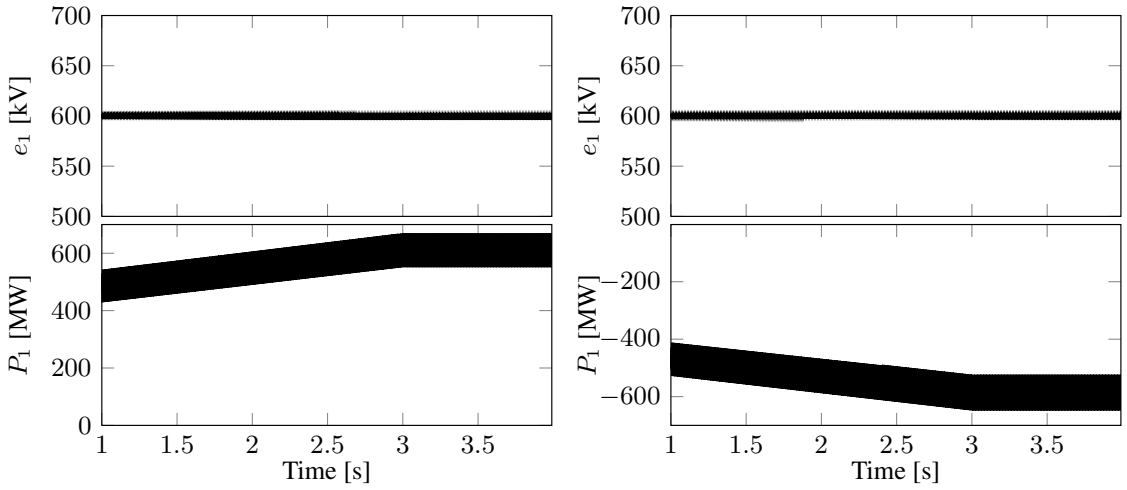

(a) (b)

Figure 2.6: Simulation results of Case 1. (a) VSC_1 dc-bus voltage and power for Case 3.1. (b) VSC_1 dc-bus voltage and power for Case 3.2

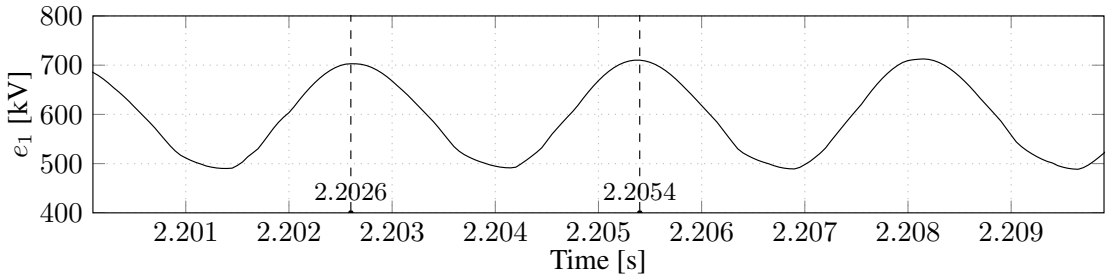

Figure 2.7: Detailed e_1 from Case 2.1. The oscillation period is 2.8 ms (RF of 357 Hz or 7.14 pu)

2.3 Eigenvalue analysis of the VSC-HVDC system

The objective of this section is to theoretically confirm the findings obtained through the simulations performed in Section 2.2. In order to perform the theoretical analysis, VSC$_i$ is modelled in the ac side as a ideal controllable three-phase voltage source connected to the ac system through the phase reactor, as depicted in Figure 2.8. In the dc side, VSC$_i$ is modelled as a current source, where the magnitude of the current is such that the power in the ac side and the dc side of the converter are equal (i.e. $P_{ci} = P_i$). The VSC dc-side

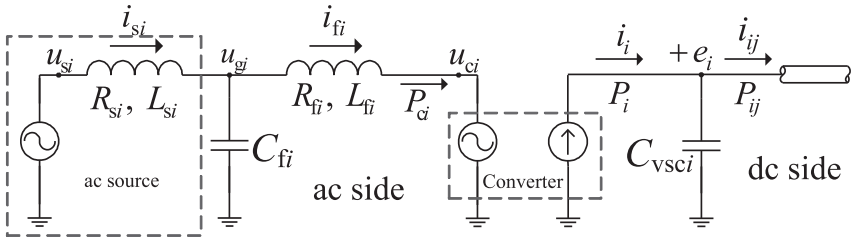

Figure 2.8: Model of the i-th VSC system

capacitor is considered as part of the dc grid,[1] then, it is not modelled as part of the VSC system. From Figure 2.8, the expression that describes the current injected by the i-th VSC to the i-th dc node, i_i, is

$$i_i = \frac{P_i}{e_i} = \frac{u_{ci}^d i_{fi}^d + u_{ci}^q i_{fi}^q}{e_i} \tag{2.5}$$

where ac-side voltages and currents are expressed in the *VSC dq* frame.[2] The expressions that describe the dynamics of the phase reactor current, $\underline{i}_{fi}^{dq}$, the voltage, $\underline{u}_{gi}^{dq}$, and the ac system current, $\underline{i}_{si}^{dq}$, are

$$\frac{\mathrm{d}i_{fi}^d}{\mathrm{d}t} = -\frac{R_{fi}}{L_{fi}} i_{fi}^d + \omega_{gi} i_{fi}^q + \frac{1}{L_{fi}} u_{gi}^d - \frac{1}{L_{fi}} u_{ci}^d \tag{2.6a}$$

$$\frac{\mathrm{d}i_{fi}^q}{\mathrm{d}t} = -\frac{R_{fi}}{L_{fi}} i_{fi}^q - \omega_{gi} i_{fi}^d + \frac{1}{L_{fi}} u_{gi}^q - \frac{1}{L_{fi}} u_{ci}^q \tag{2.6b}$$

$$\frac{\mathrm{d}i_{si}^d}{\mathrm{d}t} = -\frac{R_{si}}{L_{si}} i_{si}^d + \omega_{gi} i_{si}^q + \frac{1}{L_{si}} u_{si}^d - \frac{1}{L_{si}} u_{gi}^d \tag{2.6c}$$

$$\frac{\mathrm{d}i_{si}^q}{\mathrm{d}t} = -\frac{R_{si}}{L_{si}} i_{si}^q - \omega_{gi} i_{si}^d + \frac{1}{L_{si}} u_{si}^q - \frac{1}{L_{si}} u_{gi}^q \tag{2.6d}$$

$$\frac{\mathrm{d}u_{gi}^d}{\mathrm{d}t} = -\frac{1}{C_{fi}} i_{fi}^d + \frac{1}{C_{fi}} i_{si}^d + \omega_{gi} u_{gi}^q \tag{2.6e}$$

$$\frac{\mathrm{d}u_{gi}^q}{\mathrm{d}t} = -\frac{1}{C_{fi}} i_{fi}^q + \frac{1}{C_{fi}} i_{si}^q - \omega_{gi} u_{gi}^d. \tag{2.6f}$$

where ω_{gi} is the angular frequency estimated by the PLL$_i$. It should be noted that $\underline{u}_{si}$ is a constant vector in a *synchronous dq* frame.[3] This is due to the fact that the frequency of

[1] This is because the VSC dc-side capacitor also influence on the dc-network resonance characteristic.

[2] In the VSC *dq* frame, the angle estimated by the PLL is used to perform the transformations.

[3] Such synchronous *dq* frame rotates at a constant speed ω_0. A superscript ^{sdq} indicates that the variable is in the synchronous *dq* frame.

$\underline{u}_{\mathrm{s}i}$ is constant. Then, from [36, 42], the following is the relationship between variables in a VSC *dq* frame and a synchronous *dq* frame

$$\underline{z}_i^{dq} = \underline{z}_i^{sdq} e^{-\mathrm{j}\Delta\theta_{\mathrm{g}i}} \tag{2.7}$$

where $\Delta\theta_{\mathrm{g}i}$ is the deviation of angle calculated by the PLL$_i$ from the synchronous angle. Note that, initially, both, the PLL$_i$'s and the synchronous' angles are the same. In small signal terms, (2.7) becomes

$$\Delta\underline{z}_i^{dq} = \Delta\underline{z}_i^{sdq} - \mathrm{j}\underline{z}_0^{sdq}\Delta\theta_{\mathrm{g}i} \tag{2.8}$$

Using (2.8), then $\underline{u}_{\mathrm{s}i}^{dq} = -\mathrm{j}\underline{u}_{i0}^{sdq}\Delta\theta_{\mathrm{g}i}$. Therefore, (2.6) can be linearized as

$$\frac{\mathrm{d}\Delta i_{\mathrm{f}i}^d}{\mathrm{d}t} = -\frac{R_{\mathrm{f}i}}{L_{\mathrm{f}i}}\Delta i_{\mathrm{f}i}^d + \omega_{\mathrm{g}i0}\Delta i_{\mathrm{f}i}^q + i_{\mathrm{f}i0}^q\Delta\omega_{\mathrm{g}i} + \frac{1}{L_{\mathrm{f}i}}\Delta u_{\mathrm{g}i}^d - \frac{1}{L_{\mathrm{f}i}}\Delta u_{\mathrm{c}i}^d \tag{2.9a}$$

$$\frac{\mathrm{d}\Delta i_{\mathrm{f}i}^q}{\mathrm{d}t} = -\omega_{\mathrm{g}i0}\Delta i_{\mathrm{f}i}^d - \frac{R_{\mathrm{f}i}}{L_{\mathrm{f}i}}\Delta i_{\mathrm{f}i}^q - i_{\mathrm{f}i0}^d\Delta\omega_{\mathrm{g}i} + \frac{1}{L_{\mathrm{f}i}}\Delta u_{\mathrm{g}i}^q - \frac{1}{L_{\mathrm{f}i}}\Delta u_{\mathrm{c}i}^q \tag{2.9b}$$

$$\frac{\mathrm{d}\Delta i_{\mathrm{s}i}^d}{\mathrm{d}t} = -\frac{R_{\mathrm{s}i}}{L_{\mathrm{s}i}}\Delta i_{\mathrm{s}i}^d + \omega_{\mathrm{g}i0}\Delta i_{\mathrm{s}i}^q + i_{\mathrm{s}i0}^q\Delta\omega_{\mathrm{g}i} + \frac{u_{\mathrm{s}i0}^q}{L_{\mathrm{s}i}}\Delta\theta_{\mathrm{g}i} - \frac{1}{L_{\mathrm{s}i}}\Delta u_{\mathrm{g}i}^d \tag{2.9c}$$

$$\frac{\mathrm{d}\Delta i_{\mathrm{s}i}^q}{\mathrm{d}t} = -\frac{R_{\mathrm{s}i}}{L_{\mathrm{s}i}}\Delta i_{\mathrm{s}i}^q - \omega_{\mathrm{g}i0}\Delta i_{\mathrm{s}i}^d - i_{\mathrm{s}i0}^d\Delta\omega_{\mathrm{g}i} - \frac{u_{\mathrm{s}i0}^d}{L_{\mathrm{s}i}}\Delta\theta_{\mathrm{g}i} - \frac{1}{L_{\mathrm{s}i}}\Delta u_{\mathrm{g}i}^q \tag{2.9d}$$

$$\frac{\mathrm{d}\Delta u_{\mathrm{g}i}^d}{\mathrm{d}t} = -\frac{1}{C_{\mathrm{f}i}}\Delta i_{\mathrm{f}i}^d + \frac{1}{C_{\mathrm{f}i}}\Delta i_{\mathrm{s}i}^d + u_{\mathrm{g}i0}^q\Delta\omega_{\mathrm{g}i} + \omega_{\mathrm{g}i0}\Delta u_{\mathrm{g}i}^q \tag{2.9e}$$

$$\frac{\mathrm{d}\Delta u_{\mathrm{g}i}^q}{\mathrm{d}t} = -\frac{1}{C_{\mathrm{f}i}}\Delta i_{\mathrm{f}i}^q + \frac{1}{C_{\mathrm{f}i}}\Delta i_{\mathrm{s}i}^q - u_{\mathrm{g}i0}^d\Delta\omega_{\mathrm{g}i} - \omega_{\mathrm{g}i0}\Delta u_{\mathrm{g}i}^d \tag{2.9f}$$

$$\Delta i_i = \frac{u_{\mathrm{c}i0}^d}{e_{i0}}\Delta i_{\mathrm{f}i}^d + \frac{u_{\mathrm{c}i0}^q}{e_{i0}}\Delta i_{\mathrm{f}i}^q + \frac{i_{\mathrm{f}i0}^d}{e_{i0}}\Delta u_{\mathrm{c}i}^d + \frac{i_{\mathrm{f}i0}^q}{e_{i0}}\Delta u_{\mathrm{c}i}^q - \frac{P_{i0}}{e_{i0}^2}\Delta e_i \tag{2.9g}$$

Observe that (2.9) is a state space model of VSC$_i$ where the inputs are $u_{\mathrm{c}i}^d$, $u_{\mathrm{c}i}^q$, $\Delta\omega_{\mathrm{g}i}$ and $\Delta\theta_{\mathrm{g}i}$, and the output is i_i.

Regarding the control system, in continuous time, LPF$_i$ shown in Figure 2.3 can be represented with the following linearized state space model

$$\frac{\Delta u_{\mathrm{gfil}i}^d}{dt} = -\alpha_{\mathrm{f}i}\Delta u_{\mathrm{gfil}i}^d + \alpha_{\mathrm{f}i}u_{\mathrm{g}i}^d \tag{2.10a}$$

$$\frac{\Delta u_{\mathrm{gfil}i}^q}{dt} = -\alpha_{\mathrm{f}i}\Delta u_{\mathrm{gfil}i}^q + \alpha_{\mathrm{f}i}u_{\mathrm{g}i}^q \tag{2.10b}$$

where $\alpha_{\mathrm{f}i}$ is the closed-loop bandwidth of LPF$_i$, and $u_{\mathrm{gfil}i}^d$ and $u_{\mathrm{gfil}i}^q$ are the filtered voltages. VCC$_i$ described earlier can be expressed as

$$\frac{\mathrm{d}m_i^d}{\mathrm{d}t} = k_{\mathrm{i}i}(i_{\mathrm{f}i}^{d\mathrm{ref}} - i_{\mathrm{f}i}^d) \tag{2.11a}$$

$$\frac{\mathrm{d}m_i^q}{\mathrm{d}t} = k_{\mathrm{i}i}(i_{\mathrm{f}i}^{q\mathrm{ref}} - i_{\mathrm{f}i}^q) \tag{2.11b}$$

$$u_{\mathrm{c}i}^{d\mathrm{ref}} = u_{\mathrm{gfil}i}^d + \omega_{\mathrm{g}i}L_{\mathrm{f}i}i_{\mathrm{f}i}^q - k_{\mathrm{p}i}(i_{\mathrm{f}i}^{d\mathrm{ref}} - i_{\mathrm{f}i}^d) - m_i^d \tag{2.11c}$$

$$u_{\mathrm{c}i}^{q\mathrm{ref}} = u_{\mathrm{gfil}i}^q - \omega_{\mathrm{g}i}L_{\mathrm{f}i}i_{\mathrm{f}i}^d - k_{\mathrm{p}i}(i_{\mathrm{f}i}^{q\mathrm{ref}} - i_{\mathrm{f}i}^q) - m_i^q \tag{2.11d}$$

where m_i^d and m_i^q are states that account for the integral term of VCC$_i$. Expression (2.11) can be linearized as

$$\frac{\mathrm{d}\Delta m_i^d}{\mathrm{d}t} = k_{\mathrm{i}i}(\Delta i_{\mathrm{f}i}^{d\mathrm{ref}} - \Delta i_{\mathrm{f}i}^d) \tag{2.12a}$$
$$\frac{\mathrm{d}\Delta m_i^q}{\mathrm{d}t} = k_{\mathrm{i}i}(\Delta i_{\mathrm{f}i}^{q\mathrm{ref}} - \Delta i_{\mathrm{f}i}^q) \tag{2.12b}$$
$$\Delta u_{\mathrm{c}i}^{d\mathrm{ref}} = \Delta u_{\mathrm{gfil}i}^d + k_{\mathrm{p}i}\Delta i_{\mathrm{f}i}^d + \omega_{\mathrm{g}i0}L_{\mathrm{f}i}\Delta i_{\mathrm{f}i}^q + i_{\mathrm{f}i0}^q L_{\mathrm{f}i}\Delta\omega_{\mathrm{g}i} - \Delta m_i^d - k_{\mathrm{p}i}\Delta i_{\mathrm{f}i}^{d\mathrm{ref}} \tag{2.12c}$$
$$\Delta u_{\mathrm{c}i}^{q\mathrm{ref}} = \Delta u_{\mathrm{gfil}i}^q - \omega_{\mathrm{g}i0}L_{\mathrm{f}i}\Delta i_{\mathrm{f}i}^d + k_{\mathrm{p}i}\Delta i_{\mathrm{f}i}^q - i_{\mathrm{f}i0}^d L_{\mathrm{f}i}\Delta\omega_{\mathrm{g}i} - \Delta m_i^q - k_{\mathrm{p}i}\Delta i_{\mathrm{f}i}^{q\mathrm{ref}}. \tag{2.12d}$$

If it is assumed that the VSC operates in its linear range and that the VSC is modeled as a linear amplifier (i.e. VSC averaged model), the VCC$_i$ output, $\underline{u}_{\mathrm{c}i}^{dq\mathrm{ref}}$, and the VSC voltage, $\underline{u}_{\mathrm{c}i}^{dq}$, are related by

$$\Delta\underline{u}_{\mathrm{c}i}^{dq}(t) = \Delta\underline{u}_{\mathrm{c}i}^{dq\mathrm{ref}}(t-\tau_i). \tag{2.13}$$

where τ_i represents control system delays. PLL$_i$ is expressed, in small signal terms, as

$$\frac{\mathrm{d}\Delta n_{\omega i}}{\mathrm{d}t} = k_{\mathrm{il}i}\Delta u_{\mathrm{gfil}i}^q \tag{2.14a}$$
$$\frac{\mathrm{d}\Delta\theta_{\mathrm{g}i}}{\mathrm{d}t} = \Delta n_{\omega i} + k_{\mathrm{pl}i}\Delta u_{\mathrm{gfil}i}^q. \tag{2.14b}$$

where $n_{\omega i}$ accounts for the integral term of PLL$_i$. Finally, DVC$_i$ expressed in small signal terms is

$$\frac{\mathrm{d}\Delta n_i}{\mathrm{d}t} = k_{\mathrm{ie}i}(\Delta e_i^{\mathrm{ref}} - \Delta e_i) \tag{2.15a}$$
$$\Delta i_{\mathrm{f}i}^{d\mathrm{ref}} = k_{\mathrm{pe}i}(\Delta e_i^{\mathrm{ref}} - \Delta e_i) + \Delta n_i \tag{2.15b}$$

where n_i is a state that accounts for the integral term of DVC$_i$. In this case, a control system state space model can be derived from (2.10), (2.12), (2.14) and (2.15), where the inputs are $i_{\mathrm{f}i}^{d\mathrm{ref}}$ and $i_{\mathrm{f}i}^{q\mathrm{ref}}$ for a PC-VSC, or e_i^{ref} and $i_{\mathrm{f}i}^{q\mathrm{ref}}$ for a DVC-VSC, and the outputs are $\Delta u_{\mathrm{c}i}^{d\mathrm{ref}}$, $\Delta u_{\mathrm{c}i}^{q\mathrm{ref}}$, $\Delta\omega_{\mathrm{g}i}$ and $\Delta\theta_{\mathrm{g}i}$. Considering a Π-section model for the dc cable, as shown in Figure 2.9 the dynamics of the voltages e_1, e_2 and the current i_{12} are described, in small signal terms, by

$$\frac{\mathrm{d}\Delta e_1}{\mathrm{d}t} = -\frac{1}{C_{\mathrm{eq}}}\Delta i_{12} + \frac{1}{C_{\mathrm{eq}}}\Delta i_1 \tag{2.16a}$$
$$\frac{\mathrm{d}\Delta e_2}{\mathrm{d}t} = \frac{1}{C_{\mathrm{eq}}}\Delta i_{12} + \frac{1}{C_{\mathrm{eq}}}\Delta i_2 \tag{2.16b}$$
$$\frac{\mathrm{d}\Delta i_{12}}{\mathrm{d}t} = -\frac{R_{12}}{L_{12}}\Delta i_{12} + \frac{1}{L_{12}}\Delta e_1 - \frac{1}{L_{12}}\Delta e_2 \tag{2.16c}$$

with $C_{\mathrm{eq}} = C_1 + C_{\mathrm{vsc1}}$. System (2.16) represents the state space model of the dc grid where the inputs are the currents Δi_1 and Δi_2 and the outputs are Δe_1 and Δe_2. Using (2.9), (2.10), (2.12), (2.13), (2.15), (2.14) and (2.16), a state state space in the following form can be written for each VSC

$$\dot{\mathbf{x}}_i = \mathbf{A}_i\mathbf{x}_i + \mathbf{B}_{1i}\mathbf{r}_i + \mathbf{B}_{2i}\mathbf{w}_i + \mathbf{B}_{1i}^{\mathrm{e}}\Delta e_i \tag{2.17a}$$
$$\Delta i_i = \mathbf{C}_{1i}\mathbf{x}_i + \mathbf{D}_{11i}\mathbf{r}_i + \mathbf{D}_{12i}\mathbf{w}_i + \mathbf{D}_{11i}^{\mathrm{e}}\Delta e_i \tag{2.17b}$$
$$\mathbf{z}_i = \mathbf{C}_{2i}\mathbf{x}_i + \mathbf{D}_{21i}\mathbf{r}_i + \mathbf{D}_{22i}\mathbf{w}_i + \mathbf{D}_{21i}^{\mathrm{e}}\Delta e_i \tag{2.17c}$$
$$\mathbf{w}_i = \mathbf{z}_i(t-\tau) \tag{2.17d}$$

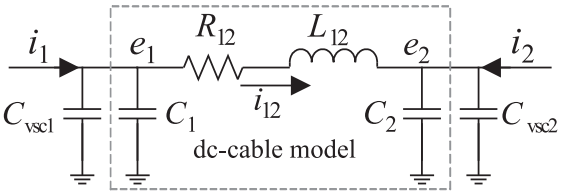

Figure 2.9: Π-section model of a dc cable.

where

$$\mathbf{x}_1 = \left[\Delta i_{\mathrm{f1}}^d \ \Delta i_{\mathrm{sf}}^q \ \Delta i_{\mathrm{s1}}^d \ \Delta i_{\mathrm{s1}}^q \ \Delta u_{\mathrm{g1}}^d \ \Delta u_{\mathrm{g1}}^q \ \Delta u_{\mathrm{gfil1}}^d \ \Delta u_{\mathrm{gfil1}}^q \ \Delta m_1^d \ \Delta m_1^q \ \Delta n_{\omega 1} \ \Delta \theta_{\mathrm{g1}} \ \Delta n_1\right]^{\mathrm{T}}$$
$$\mathbf{x}_2 = \left[\Delta i_{\mathrm{f2}}^d \ \Delta i_{\mathrm{f2}}^q \ \Delta i_{\mathrm{s2}}^d \ \Delta i_{\mathrm{s2}}^q \ \Delta u_{\mathrm{g2}}^d \ \Delta u_{\mathrm{g2}}^q \ \Delta u_{\mathrm{gfil2}}^d \ \Delta u_{\mathrm{gfil2}}^q \ \Delta m_2^d \ \Delta m_2^q \ \Delta n_{\omega 2} \ \Delta \theta_{\mathrm{g2}}\right]^{\mathrm{T}}$$
$$\mathbf{r}_1 = \left[\Delta e_1^{\mathrm{ref}} \ \Delta i_{\mathrm{f1}}^{q\mathrm{ref}}\right]^{\mathrm{T}} \quad \mathbf{r}_2 = \left[\Delta i_{\mathrm{f2}}^{d\mathrm{ref}} \ \Delta i_{\mathrm{f2}}^{q\mathrm{ref}}\right]^{\mathrm{T}}$$
$$\mathbf{w}_i = \left[\Delta u_{\mathrm{c}i}^d \ \Delta u_{\mathrm{c}i}^q\right]^{\mathrm{T}} \quad \mathbf{z}_i = \left[\Delta u_{\mathrm{c}i}^{d\mathrm{ref}} \ \Delta u_{\mathrm{c}i}^{q\mathrm{ref}}\right]^{\mathrm{T}}$$

Matrices $\mathbf{A}_i$, $\mathbf{B}_{1i}$, $\mathbf{B}_{2i}$, $\mathbf{B}_{1i}^{\mathrm{e}}$, $\mathbf{C}_{1i}$, $\mathbf{D}_{11i}$, $\mathbf{D}_{12i}$, $\mathbf{D}_{11i}^{\mathrm{e}}$, $\mathbf{C}_{2i}$, $\mathbf{D}_{21i}$, $\mathbf{D}_{22i}$ and $\mathbf{D}_{21i}^{\mathrm{e}}$ can be obtained using computational mathematical tools. Moreover, considering (2.16), the following state space model can be defined for the dc cable

$$\dot{\mathbf{x}}_{\mathrm{g}} = \mathbf{A}_{\mathrm{g}}\mathbf{x}_{\mathrm{g}} + \mathbf{B}_{\mathrm{g}}\mathbf{i}_{\mathrm{g}} \tag{2.18a}$$
$$\mathbf{e} = \mathbf{C}_{\mathrm{g}}\mathbf{x}_{\mathrm{g}} \tag{2.18b}$$

where

$$\mathbf{x}_{\mathrm{g}} = [\Delta e_1 \ \Delta e_2 \ \Delta i_{12}]^{\mathrm{T}} \quad \mathbf{i}_{\mathrm{g}} = [\Delta i_1 \ \Delta i_2]^{\mathrm{T}} \quad \mathbf{e} = [\Delta e_1 \ \Delta e_2]^{\mathrm{T}}$$
$$\mathbf{A}_{\mathrm{g}} = \begin{bmatrix} 0 & 0 & -\frac{1}{C_{\mathrm{eq}}} \\ 0 & 0 & \frac{1}{C_{\mathrm{eq}}} \\ \frac{1}{L_{12}} & -\frac{1}{L_{12}} & -\frac{R_{12}}{L_{12}} \end{bmatrix} \quad \mathbf{B}_{\mathrm{g}} = \begin{bmatrix} \frac{1}{C_{\mathrm{eq}}} & 0 \\ 0 & \frac{1}{C_{\mathrm{eq}}} \\ 0 & 0 \end{bmatrix} \quad \mathbf{C}_{\mathrm{g}} = \begin{bmatrix} 1 & 0 & 0 \\ 0 & 1 & 0 \end{bmatrix}$$

Finally, using (2.18) and (2.17) the closed loop stated space model, in the form indicated in [43], is

$$\dot{\mathbf{x}} = \ \mathbf{A}\mathbf{x} + \ \mathbf{B}_1\mathbf{r} + \ \mathbf{B}_1\mathbf{w} \tag{2.19a}$$
$$\mathbf{y} = \mathbf{C}_1\mathbf{x} + \mathbf{D}_{11}\mathbf{r} + \mathbf{D}_{12}\mathbf{w} \tag{2.19b}$$
$$\mathbf{z} = \mathbf{C}_2\mathbf{x} + \mathbf{D}_{21}\mathbf{r} + \mathbf{D}_{22}\mathbf{w} \tag{2.19c}$$
$$\mathbf{w} = \mathbf{z}(t-\tau) \tag{2.19d}$$

where

$$\mathbf{x} = [\mathbf{x}_1 \ \mathbf{x}_2 \ \mathbf{x}_{\mathrm{g}}]^{\mathrm{T}} \quad \mathbf{r} = [\mathbf{r}_1 \ \mathbf{r}_2]^{\mathrm{T}} \quad \mathbf{w} = [\mathbf{w}_1 \ \mathbf{w}_2]^{\mathrm{T}} \quad \mathbf{z} = [\mathbf{z}_1 \ \mathbf{z}_2]^{\mathrm{T}}$$
$$\mathbf{A} = \begin{bmatrix} \mathbf{A}_{\mathrm{c}} & \mathbf{B}_{1\mathrm{c}}^{\mathrm{e}}\mathbf{C}_{\mathrm{g}} \\ \mathbf{B}_{\mathrm{g}}\mathbf{C}_{1\mathrm{c}} & \mathbf{A}_{\mathrm{g}} + \mathbf{B}_{\mathrm{g}}\mathbf{D}_{11c}^{\mathrm{e}}\mathbf{C}_{\mathrm{g}} \end{bmatrix} \quad \mathbf{B}_1 = \begin{bmatrix} \mathbf{B}_{1\mathrm{c}} \\ \mathbf{B}_{\mathrm{g}}\mathbf{D}_{11\mathrm{c}} \end{bmatrix} \quad \mathbf{B}_2 = \begin{bmatrix} \mathbf{B}_{2\mathrm{c}} \\ \mathbf{B}_{\mathrm{g}}\mathbf{D}_{12\mathrm{c}} \end{bmatrix}$$
$$\mathbf{C}_2 = [\mathbf{C}_{2\mathrm{c}} \ \mathbf{D}_{21\mathrm{c}}^{\mathrm{e}}\mathbf{C}_{\mathrm{g}}] \quad \mathbf{D}_{21} = \mathbf{D}_{21\mathrm{c}} \quad \mathbf{D}_{22} = \mathbf{D}_{22\mathrm{c}}$$

and $\mathbf{C}_1$, $\mathbf{D}_{11}$ and $\mathbf{D}_{12}$ can be selected such that $\mathbf{y}$ is conformed by certain desired outputs. For example

$$\mathbf{C}_1 = \mathbf{I} \quad \mathbf{D}_{11} = \mathbf{0} \quad \mathbf{D}_{12} = \mathbf{0}$$

Moreover, matrices $\mathbf{A}_{\rm c}$, $\mathbf{B}_{1\rm c}$, $\mathbf{B}_{2\rm c}$, $\mathbf{B}^{\rm e}_{1\rm c}$... etc, are composed by matrices from (2.17), as follow

$$\mathbf{A}_{\rm c} = \begin{bmatrix} \mathbf{A}_1 & \mathbf{0} \\ \mathbf{0} & \mathbf{A}_2 \end{bmatrix} \quad \mathbf{B}_{1\rm c} = \begin{bmatrix} \mathbf{B}_{11} & \mathbf{0} \\ \mathbf{0} & \mathbf{B}_{12} \end{bmatrix} \quad \mathbf{B}_{2\rm c} = \begin{bmatrix} \mathbf{B}_{21} & \mathbf{0} \\ \mathbf{0} & \mathbf{B}_{22} \end{bmatrix} ...$$

and the same procedure is used for the other matrices. Using (2.19), the poles of the VSC-HVDC system can be obtained using mathematical computational tools.

2.3.1 Analysis of an ideal system

Let us now find the system poles for Cases 1.1 and 1.2, and Cases 2.1 and 2.2 from Section 2.2. In these cases, the VSCs are connected to infinitely strong ac grids, so the dynamics of $\text{PLL}_{1,2}$ can be neglected. This also means that, since $\underline{u}_{{\rm g}i}^{dq}$ is constant, the LPF bandwidth has no impact on the VSC dynamics. Assume also that there are no delays in the control system, i.e. $\tau_{1,2} = 0$. Moreover, remember that VSC_1 is in DVC mode and VSC_2 is in PC mode regardless of the power direction. The system poles are calculated using (2.19) for changes of $i_{\rm f2}^{d\rm ref}$ from $+1$ pu to -1 pu[1] in steps of -0.1 pu, keeping $i_{\rm f1}^{q\rm ref} = i_{\rm f2}^{q\rm ref} = 0$ (references are used to find initial values). This is performed for two cases: Low DVC gains case, with $k_{\rm pe1} = 4.62$ pu and $k_{\rm ie1} = 0.31$ pu (which corresponds to Cases 1.1 and 1.2 of Section 2.2); high DVC gains case, with $k_{\rm pe1} = 9.23$ pu and $k_{\rm ie1} = 1.23$ pu (which corresponds to Cases 2.1 and 2.2 of Section 2.2).

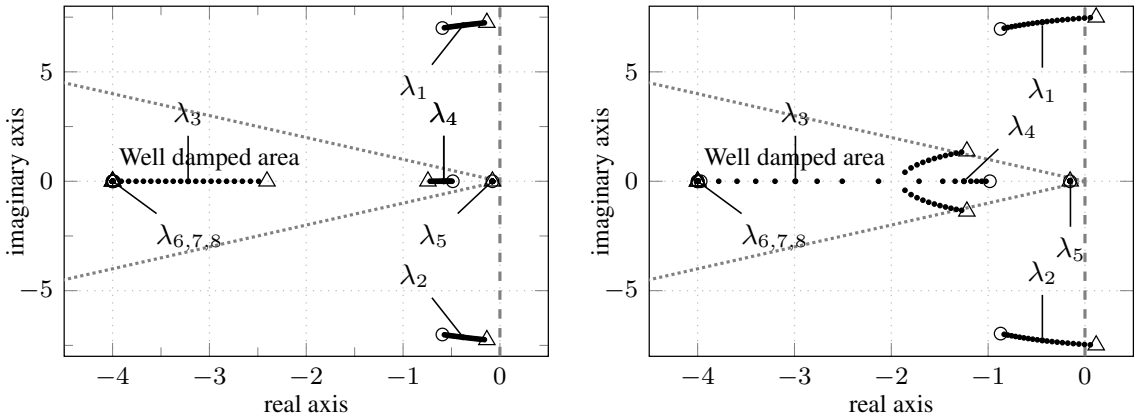

Figure 2.10: Poles as $i_{\rm f2}^{d\rm ref}$ changes from $-1(\circ)$ to $+1(\triangle)$. Left: Low DVC gains: $k_{\rm pe1} = 4.62$ pu and $k_{\rm ie1} = 0.31$ pu. Right: High DVC gains: $k_{\rm pe1} = 9.23$ pu and $k_{\rm ie1} = 1.23$ pu.

Figure 2.10 shows that, in both cases, there is a pole pair, $\lambda_{1,2}$, that moves towards the unstable region as $i_{\rm f2}^{d\rm ref}$ becomes more negative. In the low DVC gains case, all poles are stable for the considered values of $i_{\rm f2}^{d\rm ref}$, while in high DVC gains case, $\lambda_{1,2}$ are unstable for $i_{\rm f2}^{d\rm ref} < -0.8$ pu. Participation factors, presented in Table 2.5,[2] show that $\lambda_{1,2}$ are related to the dc-network dynamics, $\lambda_{3,4,5}$ to the DVC, λ_6 to VCC_1 and $\lambda_{7,8}$ to the VCC_2. The oscillation frequency of $\lambda_{1,2}$ is around 7 pu (350 Hz), which coincides with the dc-network

[1] $i_{\rm f2}^{d\rm ref} < 0$ means power flowing from VSC_1 to VSC_2.

[2] Note that, under the assumptions made, states m_i^d and m_i^q are cancelled.

Table 2.5: Participation factor absolute values for the low DVC gains case and $i_{\mathrm{f2}}^{d\mathrm{ref}} = -1$ pu

	λ_1	λ_2	λ_3	λ_4	λ_5	λ_6	λ_7	λ_8
$\Delta i_{\mathrm{f1}}^{d}$	0.039	0.039	1.728	0.786	0.007	0	0	0
$\Delta i_{\mathrm{f1}}^{q}$	0	0	0	0	0	1	0	0
Δn_1	0.000	0.000	0.026	0.200	1.175	0	0	0
$\Delta i_{\mathrm{f2}}^{d}$	0	0	0	0	0	0	1	0
$\Delta i_{\mathrm{f2}}^{q}$	0	0	0	0	0	0	0	1
Δe_1	0.289	0.289	0.502	1.018	0.091	0	0	0
Δe_2	0.219	0.219	0.354	1.009	0.092	0	0	0
Δi_{12}	0.470	0.470	0.101	0.040	0.000	0	0	0

resonance found in Section 2.2. This analysis identifies that $\lambda_{1,2}$ have the highest impact on the system stability since they are poorly damped and become unstable under certain conditions. In addition, it is shown in [36] that $\lambda_{1,2}$ are independent of the speed of VCC_2. This implies that VSC_2 can be modeled as a constant power device, since a very fast VCC_2 does not impact $\lambda_{1,2}$. Reference [36] also shows that the impact of lower values of k_{ie1} on $\lambda_{1,2}$ is very small. Therefore, the integral term of the DVC can be neglected if instabilities related to dc-network resonances are investigated.

2.3.2 Analysis of a more complex system

The analysis presented in Section 2.3.1 shows that, for a given setup, the system becomes unstable if the power transfer in the VSC-HVDC system exceeds a certain limit. This limit can be used as an indicator of the VSC-HVDC system strength for a given configuration. Then, the power transfer limit is further investigated when considering weak ac sources, delays in the control system and other dc cable lengths.[1] Again, poles are calculated using (2.19). Figure 2.11 (middle) shows the power limit for the high and low DVC gains cases

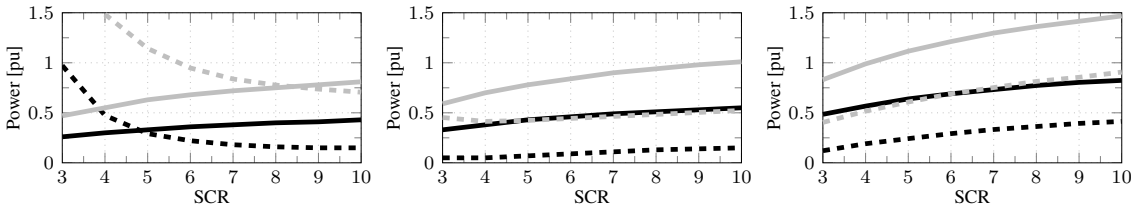

Figure 2.11: Power transfer limit for different SCRs, DVC gains, for 25 km (left), 50 km (middle) and 100 km (right) dc cable, without (solid) and with delay (dashed) in the control system. DVC gains are set as low (gray) and high (black).

investigated Section 2.3.1 for a 50 km dc cable. The first thing to note is that, in most of the cases, the system stability[2] deteriorates when the SCR decreases and also when high gains of DVCs are considered. Moreover, Figure 2.11 (middle) shows that delays have a detrimental impact in the system stability decreasing further the allowed power limit ($\tau =$

[1] Nor ac side capacitor neither LPF is considered yet in this section.

[2] The term stability is always related to dc-network resonances, unless the contrary is specified.

0.25 ms, corresponding to a sampling frequency of 4 kHz). Figure 2.11 (right) shows the power limit for the same cases analyzed previously, but for a 100 km dc cable. The figure shows that the system is more robust compared to the cases when the length is 50 km. The case with a 25 km cable (left), with no delays, shows consistent results with the previous ones, i.e. the power limit decreases with the decrease of the ac system SCR and with increased DVC gains. However, interestingly, the case with delays show contradictory results, i.e. the VSC-HVDC system is stronger when the DVC-VSC is connected to a weaker ac system.

2.4 Conclusions

In this chapter, time-domain simulations have been performed for a point-to-point VSC-HVDC system. For the sake of decreasing the system complexity, it has been assumed initially that the VSCs is connected to infinitely strong ac systems. The simulations have shown that instabilities related to the dc-network resonance phenomenon can take place, and that they depend on the power flow direction as well as the DVC controller gains. A linear model has been then derived for the studied system and eigenvalue analysis has been performed. The theoretical study shows that there are two poorly damped poles that are related to the dc-cable resonance phenomenon and that they are strongly influenced by the amount of power flow (and direction) and controller parameters. Then, more complexity has been added into the linear model, such as considering finite strength for the ac systems and delays in the control system. Considering these additional factors, the power transfer limit is studied for different scenarios. The main conclusion from the study was that power stability limit depended on:

1. Power direction. Instability only takes place when the power direction is from the DVC-VSC to the PC-VSC;
2. DVC controller gains. The higher the DVC gains, the less the power transfer limit;
3. AC system strength. When delays are not considered, the weaker the ac system to which a DVC-VSC is connected, the less the power transfer limit;
4. Control system delays. In some cases, considering delays in the control system leads to a decrease on the power stability limit. However, this cannot be generalized, as shown in Figure 2.11.

Although eigenvalue analysis has been helpful in establishing the impact of different parameters on the system stability, it does not clearly show the causes of instability. For instance, it is not clear why the direction of the power flow matter, or why the dc-network resonance becomes undamped when the DVC gains are increased or when the ac system is weaker. Moreover, the “non consistent” impact of the control system delays is unclear. In order to gain a better understanding of the origin of the instability, a frequency domain modelling approach is presented in the upcoming chapters.

Chapter 3

Frequency domain modelling approach

In Chapter 2, it has been found through simulations and eigenvalue analysis that, in some particular situations, a point-to-point VSC-HVDC system turns unstable. Factors that impact on the system stability are the dc-network resonance, DVC design, ac system strength and control system delays. However, the mechanism that triggers the instability has not been clearly identified. In this chapter, some of the questions from Chapter 2 are investigated through a frequency domain modelling approach. The approach consists of dividing the system into subsystems, such that their impact on the system stability can be studied individually. The dc-network subsystem and the VSC subsystem are defined. The study of the VSC subsystem is stressed in this chapter since it has been found to be the main cause of instability. The frequency response of the VSC subsystem is called dc-side power dependent admittance and a procedure to obtain it both, theoretically and through measurements in EMT models is presented. This chapter is based on the work presented in Papers II, III, IV and IV

3.1 Selection of subsystems – VSC-HVDC modelled as a SISO system

One advantage of applying frequency domain analysis is that a system can be divided into subsystems whose properties can be individually studied. The analysis is easier when the complexity of the system model is reduced by disregarding features that do not impact the studied problem. As concluded in [36], VSC_2 can be assumed as a constant power device when studying instabilities related to dc-network resonances. This means that the linearized system can be represented as shown in Figure 3.1, where the resistances R_{10} and R_{20} and the current Δi_1^* come from the linearization of the currents injected by VSC_1 and VSC_2, i_1 and i_2 (see (2.5)) as follows

$$\Delta i_1 = -(P_{10}/e_{10}^2)\Delta e_1 + (1/e_{10})\Delta P_1 \tag{3.1a}$$
$$\Delta i_2 = -(P_{20}/e_{20}^2)\Delta e_2 \tag{3.1b}$$

from where

$$R_{10} = \frac{e_{10}^2}{P_{10}}, \quad R_{20} = \frac{e_{20}^2}{P_{20}}, \quad \Delta i_1^* = \frac{\Delta P_1}{e_{10}}. \tag{3.2}$$

Note that R_{10} and R_{20} are of opposite signs, and that $\Delta P_2 = 0$ since VSC_2 is a constant power device. Moreover, a useful identity is $R_{10} + R_{20} = R_{12}$ [36].

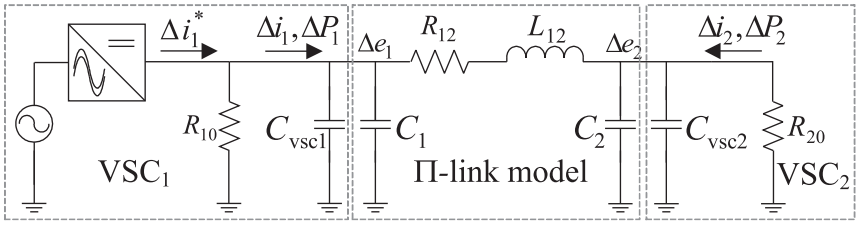

Figure 3.1: Linearized system where VSC_2 is modeled as a constant power device.

There are several ways in which subsystems can be selected in the system shown in Figure 3.1. However, in our framework, the question is how to select subsystems such that the identified resonance related instability is best understood. Figure 3.2 displays three possible

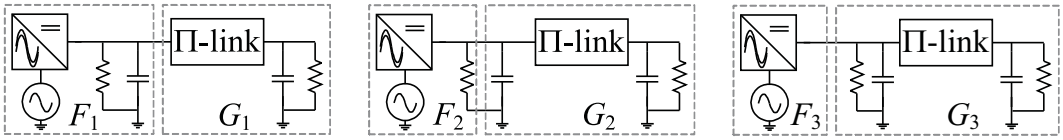

(a) Option 1 (b) Option 2 (c) Option 3

Figure 3.2: Options for selection of subsystem.

options where two subsystems are considered in each, *F* and *G*. Note that the resistances in Figure 3.2 are R_{10} and R_{20}. From the figure, the transfer functions corresponding to option 1, 2 and 3 are

$$G_1(s) = \frac{C_1^{-1} n(s)}{s(n(s) + \omega_{\text{lc1}}^2) + \omega_{\text{c2}}\omega_{\text{lc1}}^2} \tag{3.3}$$

$$G_2(s) = \frac{C_{\text{eq}}^{-1} n(s)}{s(n(s) + \omega_{\text{lc}}^2) + \omega_{\text{c2}}\omega_{\text{lc}}^2} \tag{3.4}$$

$$G_3(s) = \frac{C_{\text{eq}}^{-1} n(s)}{(s + \omega_{\text{c1}} + \omega_{\text{c2}})(d(s) + \omega_{\text{c1}}\omega_{\text{c2}}) + \epsilon} \tag{3.5}$$

where

$$d(s) = s^2 + \omega_{\text{rl}} s + 2\omega_{\text{lc}}^2, \tag{3.6}$$

$$n(s) = s^2 + (\omega_{\text{rl}} + \omega_{\text{c2}})s + \omega_{\text{lc}}^2 + \omega_{\text{rl}}\omega_{\text{c2}}, \tag{3.7}$$

$$\epsilon \quad = -\omega_{\text{c1}}\omega_{\text{c2}}(\omega_{\text{c1}} + \omega_{\text{c2}}), \tag{3.8}$$

$$\omega_{\text{c1}} = \frac{1}{R_{10}C_{\text{eq}}}, \ \omega_{\text{c2}} = \frac{1}{R_{20}C_{\text{eq}}}, \ \omega_{\text{lc}}^2 = \frac{1}{L_{12}C_{\text{eq}}}, \ \omega_{\text{lc1}}^2 = \frac{1}{L_{12}C_1}, \ \omega_{\text{rl}} = \frac{R_{12}}{L_{12}}. \tag{3.9}$$

Option 1 has been typically adopted in works such as [44, 45]. In those choices, it can be shown that G_1, as well as G_2, are unstable if VSC_2 acts as a dc load, while G_3 is unstable for $P_{20} \neq 0$. In addition, G_1 does not represent the resonance identified in Section 2.3.1 as C_{vsc1} is not included in G_1. G_2 and G_3 represent the resonance; however, the main advantage of G_3 over G_2 is that the unstable pole of G_3 is very small so it can be approximated to a pole in the origin.[1] The poles of G_3 can be approximated to

$$p_1 = -(\omega_{\text{c1}} + \omega_{\text{c2}}), \quad p_{2,3} = -\frac{\omega_{\text{rl}}}{2} \pm \sqrt{2}\omega_{\text{lc}}\sqrt{\frac{\omega_{\text{rl}}^2}{8\omega_{\text{lc}}^2} - 1} \tag{3.10}$$

if ϵ can be neglected in (3.5). This is possible if it is shown that

$$|\epsilon| \ll |2\omega_{lc}^2(\omega_{\text{c1}} + \omega_{\text{c2}})| \quad \text{and} \quad |\omega_{\text{c1}}\omega_{\text{c2}}| \ll 2\omega_{\text{lc}}^2. \tag{3.11}$$

Considering that typically voltages are maintained within nominal values in VSC-HVDC systems, then we can make $e_{10} \approx 1$ pu, $e_{20} \approx 1$ pu. Moreover, active power at both VSCs should be within limits, thus, $|P_{10}| \leq 1$, $|P_{20}| \leq 1$, and also that $R_{10} + R_{20} = R_{12}$, then, the following inequalities hold

$$-1 \leq \frac{1}{R_{10}R_{20}} \leq 0 \implies -\frac{R_{12}}{C_{\text{eq}}} \leq \omega_{\text{c1}} + \omega_{\text{c2}} \leq 0 \tag{3.12}$$

which shows that p_1 is positive and upper bounded by R_{12}/C_{eq}, being zero for $P_{20} = 0$. It can be also shown that

$$\omega_{\text{c1}} + \omega_{\text{c2}} = R_{12}C_{\text{eq}}\omega_{\text{c1}}\omega_{\text{c2}}. \tag{3.13}$$

Using (3.8) and (3.13), and considering $|\omega_{\text{c1}}\omega_{\text{c2}}| \neq 0$, the left expression in (3.11) becomes

$$|\omega_{\text{c1}} + \omega_{\text{c2}}| \ll |2\omega_{lc}^2 R_{12}C_{\text{eq}}|. \tag{3.14}$$

Considering (3.12), (3.14) is fulfilled if

$$|\frac{R_{12}}{C_{\text{eq}}}| \ll |2\omega_{lc}^2 R_{12}C_{\text{eq}}|. \tag{3.15}$$

Moreover, since $C_{\text{eq}} = C_1 + C_{\text{vsc1}}$, then (3.15) yields

$$\frac{L_{12}}{C_{\text{eq}}} < \frac{L_{12}}{C_{12}} \ll 2 \text{ pu}. \tag{3.16}$$

This means that if the square of the cable characteristic impedance is much lower than 2 pu, then, G_3 poles can be approximated to (3.10). From Table 2.1, $L_{12}/C_{12} = 0.01$ pu which is 200 times smaller than 2 pu, meaning that the poles can be approximated to (3.10).

As mentioned earlier, p_1 is upper bounded by R_{12}/C_{eq}, which gives $p_{1\max} = 0.0015$ pu. This means that, for a sufficiently high controller gain, considering $p_1 = 0$ will have a very small impact on the closed-loop system poles, as shown in [46]. Then, G_3 can be approximated to a marginally stable transfer function

$$\widetilde{G}_0(s) = \frac{C_{\text{eq}}^{-1}}{s}\left(\frac{n(s)}{d(s)}\right) \tag{3.17}$$

[1] The importance of obtaining stable F and G is that bode plots cannot be used in case of unstable systems.

Figure 3.3 shows a comparison between $\widetilde{G}_0$ for $P_{20} = +1$ pu, $P_{20} = -1$ pu and the transfer function of the Π-link together with the VSC capacitors without R_{10} and R_{20}, given by

$$G_0(s) = \frac{C_{\text{eq}}^{-1}(s^2 + \omega_{\text{rl}}s + \omega_{\text{lc}}^2)}{s(s^2 + \omega_{\text{rl}}s + 2\omega_{\text{lc}}^2)}. \tag{3.18}$$

Although not rigorously proved, the comparison shows that $\widetilde{G}_0$ can be approximated to G_0 since their differences are very small. Therefore, considering $i_{\text{fl}}^{\text{qref}}$ constant, the HVDC system can be modeled as the Single-Input, Single-Output (SISO) feedback system illustrated in Figure 3.4, where F_3 has been renamed to F.

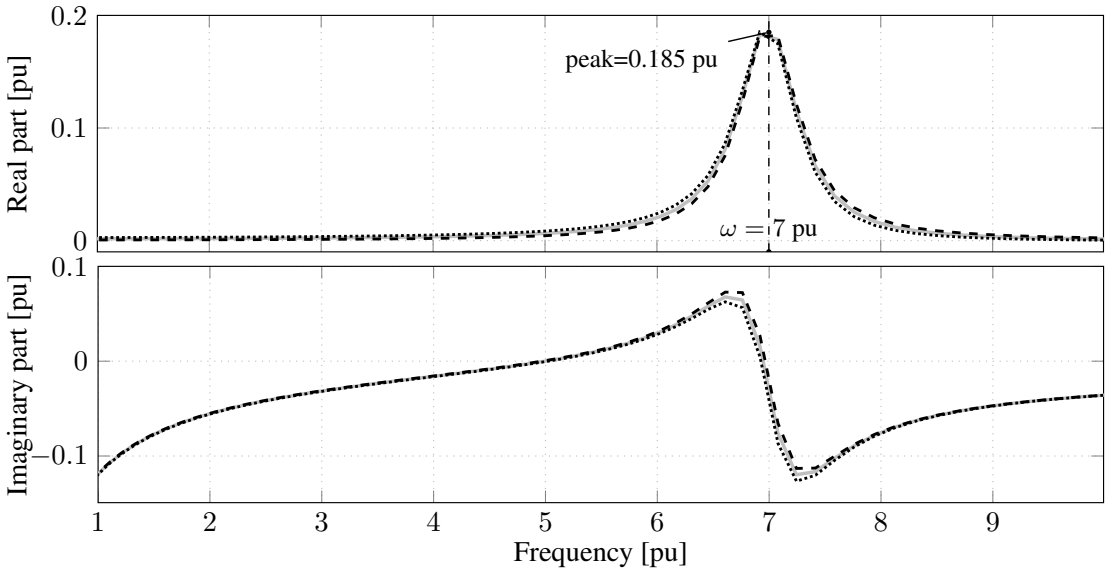

Figure 3.3: Real (upper) and imaginary (bottom) parts of $\widetilde{G}_0$ for $i_{\text{fl}}^{\text{dref}} = +1$ pu (dashed), $\widetilde{G}_0$ for $i_{\text{fl}}^{\text{dref}} = -1$ pu (dotted), and G_0 (gray solid).

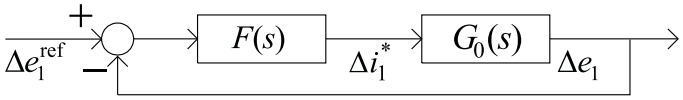

Figure 3.4: VSC-HVDC system represented as a SISO system.

The conclusion that G_3 can be approximated to G_0 has been deduced considering that the dc cable is modeled as a lumped-parameter Π-section. A Π-section has been chosen here since its simplicity allows analytical derivations and due to the fact that it still represents the resonance of a dc TL. In Chapter 5, which deals with stability analysis in HVDC grids, the analysis is extended for distributed parameter models of dc TLs.

Regarding F, the transfer function can be obtained from (2.17) but considering that the output is now Δi_i^* instead of Δi_i. Then the VSC subsystem state space can be written as

$$\dot{\mathbf{x}}_i = \mathbf{A}_i\mathbf{x}_i + \mathbf{B}_{1i}\mathbf{r}_i + \mathbf{B}_{2i}\mathbf{w}_i + \mathbf{B}_{1i}^{\text{e}}\Delta e_i \tag{3.19a}$$

$$\Delta i_i^* = \mathbf{C}_{1i}\mathbf{x}_i + \mathbf{D}_{11i}\mathbf{r}_i + \mathbf{D}_{12i}\mathbf{w}_i \tag{3.19b}$$

$$\mathbf{z}_i = \mathbf{C}_{2i}\mathbf{x}_i + \mathbf{D}_{21i}\mathbf{r}_i + \mathbf{D}_{22i}\mathbf{w}_i + \mathbf{D}_{21i}^{\text{e}}\Delta e_i \tag{3.19c}$$

$$\mathbf{w}_i = \mathbf{z}_i(t - \tau) \tag{3.19d}$$

where all the matrices are as defined in (2.17). The frequency response of F can be obtained through mathematical computation tools.

3.2 Passivity analysis in the SISO system

The convenience of modeling the VSC-HVDC system as in Figure 3.4 is that passivity properties of G_0 and F can be studied individually in order to determine if the system is stable. A stable system $H(s)$ is passive if [47]

$$\forall\omega \geq 0, \;\; \mathrm{Re}\left[H(\mathrm{j}\omega)\right] \geq 0. \tag{3.20}$$

Considering the SISO system of Figure 3.4, and according to [47], if both, G_0 and F, are passive, then, the closed-loop system is passive, and therefore stable. On the other hand, the converse is not necessarily true. That is, if either G_0 or F is passive while the other is non-passive, then, the closed-loop system is not necessarily non-passive neither unstable. However, this indicates that there is a risk of instability. To determine if the system is unstable, Nyquist stability criterion can be applied in the SISO system as in [44, 45].

In the SISO system of Figure 3.4, the G_0 is actually the dc-network impedance seen from the bus where VSC_1 is connected. Since the dc-network is only composed of passive elements, then, it can be confidently claimed that G_0 is passive. This means that, if F is stable, the unstable cases shown previously are due to the fact that F is non-passive. Then, let us derive an expression F considering a DVC-VSC system with no delays, no ac-side capacitor, and no filtering of the measured quantities (i.e no LPF). Consider first that the current Δi_1^*, defined in (3.19b), is expressed as

$$\Delta i_1^* = \frac{1}{e_{10}}\left(u^d_{\mathrm{c}10}\Delta i^d_{\mathrm{f}1} + u^q_{\mathrm{c}10}\Delta i^q_{\mathrm{f}1} + i^d_{\mathrm{f}10}\Delta u^d_{\mathrm{c}1} + i^q_{\mathrm{f}10}\Delta u^q_{\mathrm{c}1}\right). \tag{3.21}$$

Since there is no ac-side capacitor in the VSC shown in Figure 2.8, then, $\underline{i}^{dq}_{\mathrm{f}i} = \underline{i}^{dq}_{\mathrm{s}i}$. Therefore, voltages $u^d_{\mathrm{c}1}$ and $u^q_{\mathrm{c}1}$ in the VSC *dq* frame can be expressed in the Laplace domain as

$$u^d_{\mathrm{c}1} = u^d_{\mathrm{s}1} - (R_{\mathrm{t}1} + sL_{\mathrm{t}1})i^d_{\mathrm{f}1} + \omega_{\mathrm{g}1}L_{\mathrm{t}1}i^q_{\mathrm{f}1} \tag{3.22a}$$
$$u^q_{\mathrm{c}1} = u^q_{\mathrm{s}1} - (R_{\mathrm{t}1} + sL_{\mathrm{t}1})i^q_{\mathrm{f}1} - \omega_{\mathrm{g}1}L_{\mathrm{t}1}i^d_{\mathrm{f}1} \tag{3.22b}$$

where $L_{\mathrm{t}1} = L_{\mathrm{f}1} + L_{\mathrm{s}1}$ and $R_{\mathrm{t}1} = R_{\mathrm{f}1} + R_{\mathrm{s}1}$. Furthermore, considering (2.7), $u^d_{\mathrm{s}1}$ and $u^q_{\mathrm{s}1}$ can be expressed as $u^d_{\mathrm{s}1} = u^q_{\mathrm{s}10}\Delta\theta_{\mathrm{g}1}$ and $u^q_{\mathrm{s}1} = -u^d_{\mathrm{s}10}\Delta\theta_{\mathrm{g}1}$. Then, (3.22) can be linearized and expressed in the VSC *dq*-frame as

$$\Delta u^d_{\mathrm{c}1} = \;\; u^q_{\mathrm{s}10}\Delta\theta_{\mathrm{g}1} - (R_{\mathrm{t}1} + sL_{\mathrm{t}1})\Delta i^d_{\mathrm{f}1} + \omega_{\mathrm{g}1}L_{\mathrm{t}1}\Delta i^q_{\mathrm{f}1} + i^q_{\mathrm{f}10}L_{\mathrm{t}1}\Delta\omega_{\mathrm{g}1} \tag{3.23a}$$
$$\Delta u^q_{\mathrm{c}1} = -u^d_{\mathrm{s}10}\Delta\theta_{\mathrm{g}1} - (R_{\mathrm{t}1} + sL_{\mathrm{t}1})\Delta i^q_{\mathrm{f}1} - \omega_{\mathrm{g}1}L_{\mathrm{t}1}\Delta i^d_{\mathrm{f}1} - i^d_{\mathrm{f}10}L_{\mathrm{t}1}\Delta\omega_{\mathrm{g}1} \tag{3.23b}$$

and, in steady state $u^d_{\mathrm{c}10}$ and $u^q_{\mathrm{c}10}$ are

$$u^d_{\mathrm{c}10} = u^d_{\mathrm{s}10} - R_{\mathrm{t}1}i^d_{\mathrm{f}10} + \omega_{\mathrm{g}10}L_{\mathrm{t}1}i^q_{\mathrm{f}10} \tag{3.24a}$$
$$u^q_{\mathrm{c}10} = u^q_{\mathrm{s}10} - R_{\mathrm{t}1}i^q_{\mathrm{f}10} - \omega_{\mathrm{g}10}L_{\mathrm{t}1}i^d_{\mathrm{f}10} \tag{3.24b}$$

replacing (3.23) and (3.24) into (3.21) and factorizing accordingly, the following is obtained

$$\Delta i_1^* = -\frac{i_{\mathrm{f10}}^d L_{\mathrm{t1}}}{e_{10}}(s+z_1^d)\Delta i_{\mathrm{f1}}^d - \frac{i_{\mathrm{f10}}^q L_{\mathrm{t1}}}{e_{10}}(s+z_1^q)\Delta i_{\mathrm{f1}}^q + \frac{u_{\mathrm{s10}}^q i_{\mathrm{f10}}^d - u_{\mathrm{s10}}^d i_{\mathrm{f10}}^q}{e_{10}}\Delta\theta_{\mathrm{g1}} \tag{3.25}$$

where z_1^d and z_1^q are

$$z_1^d = 2\frac{R_{\mathrm{t1}}}{L_{\mathrm{t1}}} - \frac{u_{\mathrm{s10}}^d}{i_{\mathrm{f10}}^d L_{\mathrm{t1}}}, \qquad z_1^q = 2\frac{R_{\mathrm{t1}}}{L_{\mathrm{t1}}} - \frac{u_{\mathrm{s10}}^q}{i_{\mathrm{f10}}^q L_{\mathrm{t1}}}. \tag{3.26}$$

Moreover, under the assumptions made, the transfer functions the VCC_1 are [36]

$$\Delta i_{\mathrm{f1}}^d = \frac{\alpha_1}{s+\alpha_1}\Delta i_{\mathrm{f1}}^{d\mathrm{ref}}, \quad \Delta i_{\mathrm{f1}}^q = \frac{\alpha_1}{s+\alpha_1}\Delta i_{\mathrm{f1}}^{q\mathrm{ref}}. \tag{3.27}$$

Replacing (3.27) into (3.25) and assuming that $i_{\mathrm{f1}}^{q\mathrm{ref}}$ is constant ($\Delta i_{\mathrm{f}}^{q\mathrm{ref}} = 0$), then, (3.25) becomes

$$\Delta i_1^* = -\frac{\alpha_1 i_{\mathrm{f10}}^d L_{\mathrm{t1}}}{e_{10}}\left(\frac{s+z_1^d}{s+\alpha_1}\right)\Delta i_{\mathrm{f1}}^{d\mathrm{ref}} + \frac{Q_{\mathrm{s10}}}{e_{10}}\Delta\theta_{\mathrm{g1}} \tag{3.28}$$

where Q_{s0} is $u_{\mathrm{s0}}^q i_{\mathrm{f0}}^d - u_{\mathrm{s0}}^d i_{\mathrm{f0}}^q$. Moreover, the open loop transfer function of the DVC is

$$\Delta i_{\mathrm{f1}}^{d\mathrm{ref}} = \left(k_{\mathrm{pe1}} + \frac{k_{\mathrm{ie1}}}{s}\right)\Delta u_1 = F_{\mathrm{dvc1}}(s)\Delta u_1 \tag{3.29}$$

with $\Delta u = \Delta e_1^{\mathrm{ref}} - \Delta e_1$. Putting (3.29) into (3.28) then Δi_1^* becomes

$$\Delta i_1^* = F_c(s)\Delta u + \frac{Q_{\mathrm{s10}}}{e_{10}}\Delta\theta_{\mathrm{g1}} \tag{3.30}$$

where

$$F_c(s) = -\frac{\alpha_1 i_{\mathrm{f10}}^d L_{\mathrm{t1}}}{e_{10}}\left(\frac{s+z_1^d}{s+\alpha_1}\right)F_{\mathrm{dvc1}}(s). \tag{3.31}$$

Continuing with (3.30), the angle $\Delta\theta_{\mathrm{g1}}$ and the frequency $\Delta\omega_{\mathrm{g1}}$ are estimated by the PLL defined by (2.14). In the Laplace domain, (2.14) is expressed as

$$\Delta\theta_{\mathrm{g1}} = \frac{k_{\mathrm{pl1}}s + k_{\mathrm{il1}}}{s^2}\Delta u_{\mathrm{g1}}^q = F_{\mathrm{pll}}(s)\Delta u_{\mathrm{g1}}^q. \tag{3.32}$$

Considering the voltage drop over the ac source impedance and that $\Delta\omega_{\mathrm{g1}} = s\theta_{\mathrm{g1}}$, then, Δu_{g1}^q can be expressed as

$$\Delta u_{\mathrm{g1}}^q = -(u_{s10}^d + s i_{\mathrm{f10}}^d L_{\mathrm{s1}})\Delta\theta_{\mathrm{g1}} - (R_{\mathrm{s1}} + sL_{\mathrm{s1}})\Delta i_{\mathrm{f1}}^q - \omega_{\mathrm{g10}}L_{\mathrm{s1}}\Delta i_{\mathrm{f1}}^d. \tag{3.33}$$

Combining (3.32) and (3.33), the following expression for the angle $\Delta\theta_{\mathrm{g1}}$ is obtained

$$\Delta\theta_{\mathrm{g1}} = -\frac{(R_{\mathrm{s1}} + sL_{\mathrm{s1}})F_{\mathrm{pll}}(s)}{1 + (u_{s10}^d + s i_{\mathrm{f10}}^d L_{\mathrm{s1}})F_{\mathrm{pll}}(s)}\Delta i_{\mathrm{f1}}^q - \frac{\omega_{\mathrm{g10}}L_{\mathrm{s1}}F_{\mathrm{pll}}(s)}{1 + (u_{s10}^d + s i_{\mathrm{f10}}^d L_{\mathrm{s1}})F_{\mathrm{pll}}(s)}\Delta i_{\mathrm{f1}}^d. \tag{3.34}$$

Considering (3.27), and that $\Delta i_{\mathrm{f}}^{q\mathrm{ref}}$ is zero, (3.34) becomes

$$\Delta\theta_{\mathrm{g1}} = \frac{e_{10}}{Q_{\mathrm{s10}}}F_\theta(s)\Delta u_1. \tag{3.35}$$

where

$$F_\theta(s) = -\frac{\omega_{\mathrm{g10}} Q_{\mathrm{s10}} L_{\mathrm{s1}} \alpha_1 F_{\mathrm{pll}}(s) F_{\mathrm{vdc1}}(s)}{e_{10}(1 + (u^d_{s10} + s i^d_{\mathrm{f10}} L_{\mathrm{s1}}) F_{\mathrm{pll}}(s))(s + \alpha_1)}. \tag{3.36}$$

Finally, the expression of $F(s)$ for VSC_1 connected to a weak ac systems is

$$F(s) = F_{\mathrm{c}}(s) + F_\theta(s) \tag{3.37}$$

with $F_{\mathrm{c}}(s)$ and $F_\theta(s)$ as defined above. Note that the assumption of neglecting the PLL made in Section 2.3.1 cannot be made anymore for a weak ac system. This is reflected by the transfer function $F_\theta(s)$, described by (3.36), which includes the PLL dynamics through the transfer function $F_{\mathrm{pll}}(s)$.

3.3 Study of F for a VSC connected to an infinite ac source

In the case of DVC-VSCs connected to infinitely strong ac systems, and considering a proportional DVC, then, $F_\theta = 0$, $L_{\mathrm{s1}} = R_{\mathrm{s1}} = 0$ and $u^d_{\mathrm{s10}} = u^d_{\mathrm{g10}}$, yielding

$$F(s) = -\frac{\alpha_1 i^d_{\mathrm{f10}} L_{\mathrm{f1}} k_{\mathrm{pe1}}}{e_{10}} \left(\frac{s + z^d_1}{s + \alpha_1} \right). \tag{3.38}$$

Note that it is assumed $k_{\mathrm{ie1}} = 0$. First of all, F is stable since its only pole is $-\alpha_1$. Moreover, F has a zero, $-z^d_1$. Neglecting R_{f1}, this revealing expression shows that F is passive when $i^d_{\mathrm{f10}} < 0$[1] due to the fact that the zero, $-z^d_1$, is located in the Left Half of the s-plane (LHP). This is also shown in Figure 3.5, where $F(\mathrm{j}\omega)$ is plotted for different i^d_{f10} and considering $k_{\mathrm{pe1}} = 9.23$ pu. For negative values of i^d_{f10}, $\mathrm{re}[F(\mathrm{j}\omega)]$ is positive for all frequencies, ω. In this case, both, F and G_0 are passive, meaning that the closed-loop system is stable. This implies that, when VSC_1 absorbs power from the dc network, the system is stable for any positive value of k_{pe1} and α_1.[2] On the other hand, (3.38) shows that $-z^d_1$ lies in the RHP when $i^d_{\mathrm{f10}} > 0$, i.e. F is non-passive (non-minimum phase) i.e. when VSC_1 injects power into the dc network. This can also be seen in Figure 3.5 where $\mathrm{re}[F(\mathrm{j}\omega)]$ is positive for a low ω and it becomes negative as ω increases. Interestingly, at $\omega = 7$ pu (RF of G_0), $\mathrm{re}[F(\mathrm{j}\omega)]$ is negative, which means that the dc-network resonance can be amplified due to the non-passive behavior of F at this frequency. In addition, (3.38) shows that, if α_1, k_{pe}, L_{f1} and $|i^d_{\mathrm{f10}}|$ increase, $\mathrm{re}[F(\mathrm{j}\omega)]$ becomes more negative, increasing also the risk of instability. This explains why high DVC gains decrease the power transfer limit, and also why instability depends on the amount of power that VSC_1 injects into the dc network (see Figure 2.5). In addition, a PI DVC has a phase shift of 90° for low ω and goes to 0° as ω increases. For $\omega = 7$, and considering $k_{\mathrm{ie1}} = 1.31$ pu, $F_{\mathrm{dvc1}}(\mathrm{j}7) = 9.23 + \mathrm{j}0.18$, hence the negligible impact of the DVC integrator stated in [36].

In Section 2.3.2 the impact of considering more complex VSC systems on the system stability is investigated through eigenvalue analysis. The causes of instability for more complex VSC models can be better explained then with the definition adopted in next section.

[1] Negative i^d_{f10} means that power flows from VSC_2 to VSC_1.

[2] Actually, $\alpha_1 k_{\mathrm{pe}}$ should be higher than a certain value since $G_3(s)$ has a small unstable pole.

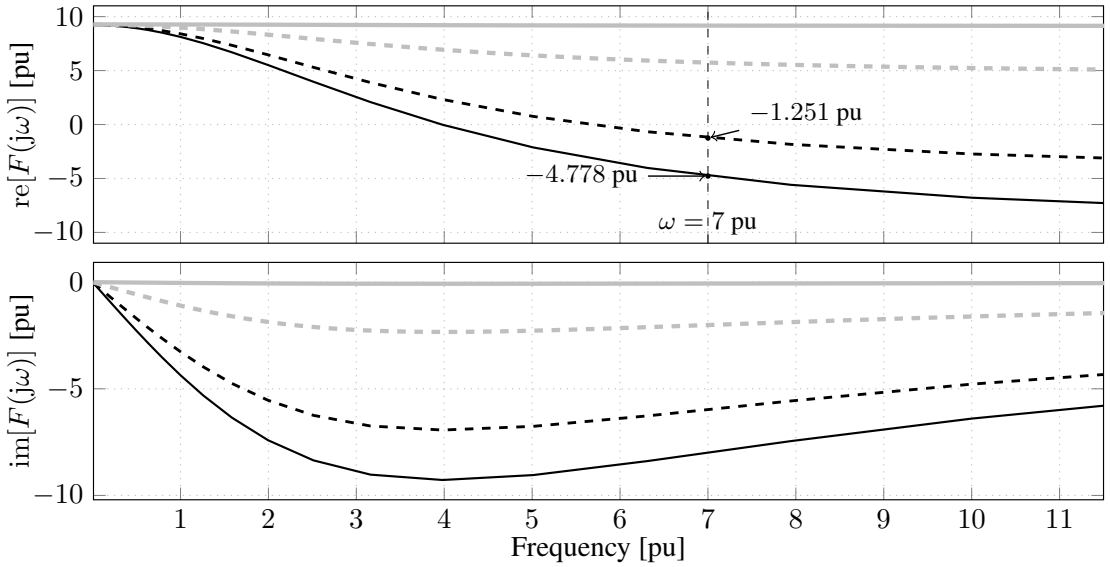

Figure 3.5: $\mathrm{re}[F(\mathrm{j}\omega)]$ (upper) and $\mathrm{im}[F(\mathrm{j}\omega)]$ (bottom) for $i^d_{\mathrm{f10}} = +1$ pu (black solid), $i^d_{\mathrm{f10}} = +0.5$ pu (black dashed), $i^d_{\mathrm{f10}} = -0.5$ pu (gray dashed), and $i^d_{\mathrm{f10}} = +1$ pu (gray solid). AC source is infinite and $k_{\mathrm{pe1}} = 9.23$ pu.

3.4 Defining F as a dc-side power dependent admittance

As discussed previously, $G_0(s)$ is, in practice, the impedance seen from the bus where the VSC is connected, meaning that frequency scan can be applied to obtain $G_0(\mathrm{j}\omega)$ for more complex dc networks. The same idea can be applied to $F(\mathrm{j}\omega)$ since, due to the dimensions of its input and output, it can be interpreted as an admittance defined by

$$F(\mathrm{j}\omega) = -\frac{\Delta i_1^*(\mathrm{j}\omega)}{\Delta e_1(\mathrm{j}\omega)} \tag{3.39}$$

or, making $\Delta i_1^* = \Delta P_1 / e_{10}$, and considering $e_{10} = 1$ pu, then, the admittance defined in (3.39) can be expressed as

$$F(\mathrm{j}\omega) = -\frac{\Delta P_1}{\Delta e_1} \tag{3.40}$$

This means that, if $F(\mathrm{j}\omega)$ is to be measured, this can be done by superimposing a sinusoidal signal in e_1, and then, measuring the corresponding sinusoidal component of P_1. Hence, the term dc-side Power Dependent Admittance (dc-side PDA) is adopted in this thesis to refer to $F(\mathrm{j}\omega)$. Likewise, dc-side Power Dependent Conductance (dc-side PDC) refers to $\mathrm{Re}[F(\mathrm{j}\omega)]$,[1] while dc-side Power Dependent Susceptance (dc-side PDS) refers to $\mathrm{Im}[F(\mathrm{j}\omega)]$. Observe that this definition is valid for any control system, as long as the input and the output are defined as in (3.40). With the definition of F as a dc-side PDA, the results in Section 3.2 can be interpreted as follow:

1. If a dc-network resonance coincides with a positive dc-side PDC, then, the resonance will be attenuated;

[1] In this thesis, the term dc-side PDC and $\mathrm{re}(F(\mathrm{j}\omega))$ are used without distinction.

2. If the resonance coincides with a negative dc-side PDC, there is a risk that the resonance becomes amplified;

3. For a given resonance, the more negative the dc-side PDC, the weaker the system. This means that the power limit with regards to stability decreases.

This explains why instability takes place at a higher power transfer when the dc cable length is 100 km (see Section 2.3.2) since the resonance occurs at a lower frequency (4.46 pu), where the dc-side PDC is less negative.

The analysis performed in Section 3.3 shows that, for a given dc-network configuration, the system stability depends on the characteristics of the dc-side PDC. In Section 3.3, the investigation is carried out on an ideal model of VSC_1 connected to a strong ac system with no delays. The impact of less ideal conditions on the dc-side PDC, and their connection to the power transfer limits presented in Section 2.3.2 are investigated next.

3.5 Impact of non-infinite SCRs and delays on the dc-side PDC

Consider $k_{\text{pe1}} = 4.62$ pu and $k_{\text{ie1}} = 0$ for the cases studied in this section. First, the impact of DVC-VSCs connected to weak ac grids on the dc-side PDC is studied without considering system delays. This means that the dc-side PDA is given by (3.37). Figure 3.6 shows the dc-side PDC for SCRs of 3, 5 and infinity with $i^d_{\text{f10}} = 1$ pu in all the cases. The dc-side PDC becomes more negative as the SCR decreases, and for $\omega = 7$ pu and an SCR of 5 it is -5.567 pu. This is even lower than the corresponding case shown in Figure 3.5 (-4.778 pu), which is known to be unstable. Therefore, the decrease of power transfer limit studied in Section 2.3.2 for low SCR is associated to the fact that the dc-side PDC is more negative in such cases.

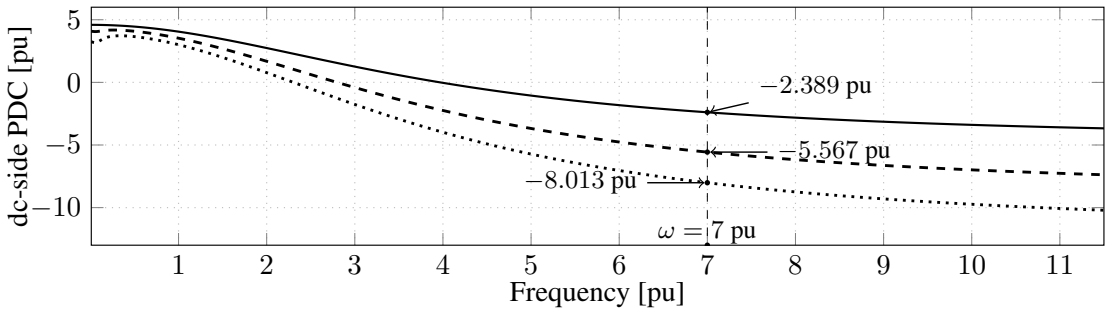

Figure 3.6: DC-side PDC for $i^d_{\text{f10}} = +1$ pu and SCR = infinity (solid), SCR = 5 (dashed) and SCR = 3 (dotted).

The dc-side PDA considering delays can be calculated using (3.19). Figure 3.7 shows the dc-side PDA for delays of 0.25ms and 0.5ms, for an SCR of 5, and for $i^d_{\text{f10}} = 1$ pu. It can be seen when delays are considered that the dc-side PDC decreases even further, but only in some specific frequency ranges. In fact, the figure shows that, with delays, the dc-side PDC

also increases at certain frequencies. At $\omega = 7$ pu (which corresponds to the RF of the 50 km dc cable) and with a delay of 0.25 ms, the dc-side PDC actually decreases to -10.51 pu, which is considerably lower compared to the case with no delays. This is in connection with the decrease of the power transfer limit shown in Section 2.3.2. Observe, however, when a delay of 0.5 ms is considered, the dc-side PDC actually increases for $\omega = 7$ pu, which suggests that the power stability limit increases for such a configuration. Note also that the minimum value of the dc-side PDC decreases with the increase of the delay time. This means that, while stability improves at some frequencies, at the same time, stability has also worsened at other frequencies.

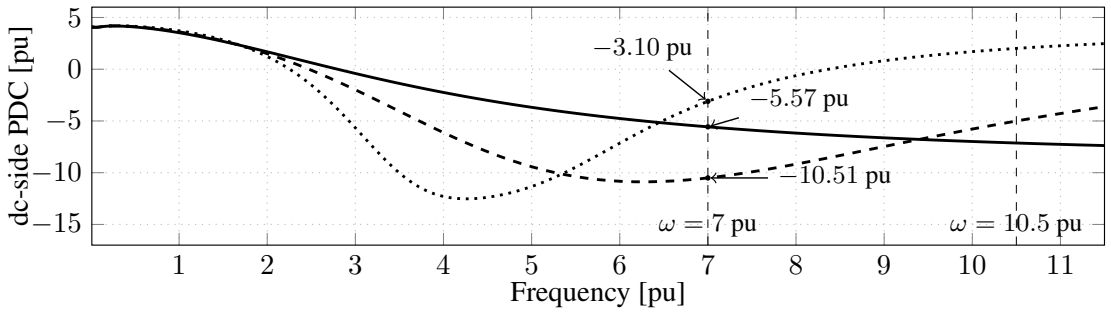

Figure 3.7: DC-side PDC for $i^d_{\text{fl0}} = +1$ pu and SCR $= 5$. No delay (Solid). Delay of 0.25 ms (dashed). Delay of 0.5 ms (dotted).

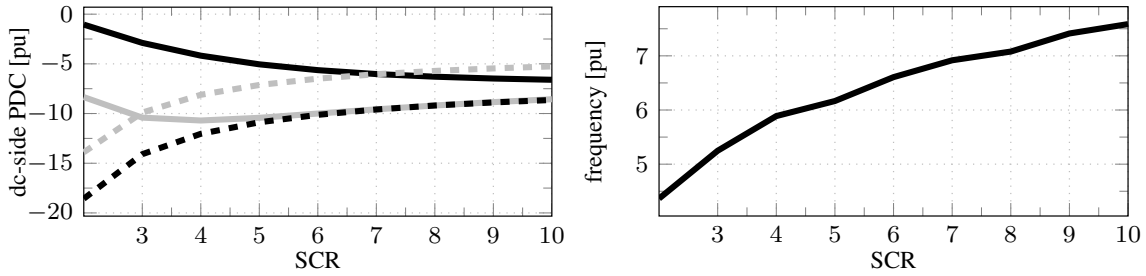

Figure 3.8: Left: Impact of a delay of 0.25ms and different SCRs on the dc-side PDC for $\omega = 10.5$ pu (black solid), $\omega = 7$ pu (gray solid), and the minimum dc-side PDC (black dashed). For comparison, dc-side PDC for $\omega = 10.5$ pu with no delays (gray dashed) is also plotted. Right: frequency corresponding to the minimum dc-side PDC.

Bear in mind that, as discussed previously, the more negative the dc-side PDC, the lower the power transfer limit, and that, in the cases with no delays, the dc-side PDC is more negative with lower SCRs (i.e. a weaker ac system limits further the power transfer limit). Now, the contradictory results in Figure 2.11(Left) for a 25 km dc cable (RF of 10.5 pu) considering delays can be best understood by observing the dc-side PDC for $\omega = 10.5$ pu. This is plotted in Figure 3.8 (left, black solid) where it can be seen that, contrary to the cases with no delays, the dc-side PDC becomes more negative with the increase of the SCR. For this setup, this means that the system stability deteriorates when the DVC-VSC is connected to a stronger ac system, which is in agreement with the results shown in Figure 2.11(Left). Figure 3.8 also shows the minimum dc-side PDC and its corresponding frequency for different SCRs and with a delay of 0.25ms. The figure shows that the minimum dc-side PDC decreases with weaker ac systems, as well as the corresponding frequencies. Let us still

consider the 25 km dc cable as an example (RF of 10.5 pu), Figure 3.8 indicates that, for an SCR of 3, with delays, the dc-side PDC is -2.9 pu, which is an improvement compared to the case with no delays, with a dc-side PDC of -9.9 pu. However, for the same SCR and delay, the minimum dc-side PDC has decreased to -14 pu for a $\omega = 5.25$ pu. This means that, although stability has improved for a VSC with a 25 km cable ($\omega^{\mathrm{r}} = 10.5$ pu), instability can take place if dc-network upgrades lead to a new RF of 5.25 pu.

3.6 Impact of different DVC structure

In previous sections, it has been shown that the instability is introduced by the VSC controlling the dc-bus voltage. Thus, it is also important to study the impact of other DVC structures, such as the voltage droop controllers proposed for MTDC systems [26]. Although these controllers are proposed for MTDC systems, they are studied in the point-to-point VSC-HVDC system investigated in this chapter for the sake of simplicity. Later, when MTDC systems are analyzed in this thesis, the droop controller that contributes the most on increasing the dc-side PDC is implemented. The impact on the dc-side PDC of the DVCs shown in Figure 3.9 are studied in this section. A controller delay of 0.25 ms, SCR of 5, $k_{\mathrm{pe}} = 4.62$ pu and $k_{\mathrm{ie}} = 0.31$ pu, with no LPFs, and no ac side capacitor are considered. These parameters are selected due to the fact that they are going to used later on the simulation studies in Section 3.7. In order to investigate the impact of the droop setting, the dc-side PDC is calculated for two values of k_{d}, 0.05 pu and 0.1 pu.

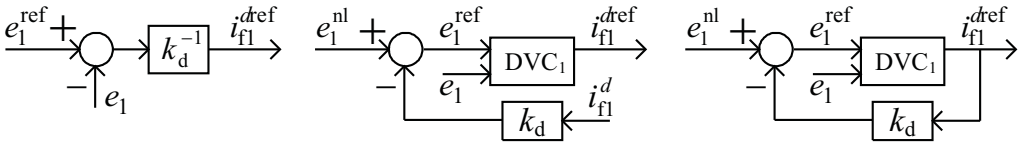

Figure 3.9: DVC 1 (left), DVC 2 (middle) and DVC 3 (right).

The following expressions define the droop controllers in Figure 3.9

$$\text{DVC 1:} \quad i_{\mathrm{f}i}^{d\mathrm{ref}} = k_{\mathrm{d}i}^{-1}\left(e_i^{\mathrm{nl}} - e_i\right) \tag{3.41a}$$

$$\text{DVC 2:} \quad e_i^{\mathrm{ref}} = e_i^{\mathrm{nl}} - k_{\mathrm{d}i} i_{\mathrm{f}i}^{d} \tag{3.41b}$$

$$\text{DVC 3:} \quad e_i^{\mathrm{ref}} = e_i^{\mathrm{nl}} - k_{\mathrm{d}i} i_{\mathrm{f}i}^{d\mathrm{ref}} \tag{3.41c}$$

where e_i^{nl} is the no load voltage reference. These expressions, combined with (3.19) can be used to obtain a new state space model, and hence, $F(\mathrm{j}\omega)$. Note that the output of DVC 1 is $i_{\mathrm{f}i}^{d\mathrm{ref}}$, which means that the PI DVC studied earlier is not included. Then DVC 1 can be interpreted as a proportional controller with a gain of $k_{\mathrm{d}i}$. On other hand, the output of DVC 1 and DVC 2 is e_i^{ref}, which is an input to PI DVC, so, the earlier studied PI DVC is included in these cases.

Figure 3.10 shows the dc-side PDC for the cases stated above and compared with the DVC defined by (2.15). It can be seen that DVC 1 is the less convenient choice since it turns the dc-side PDC more negative. This is expected since $k_{\mathrm{d}} = 0.05$ pu and $k_{\mathrm{d}} = 0.10$ pu

corresponds to $k_{\mathrm{pe1}} = 20$ pu and $k_{\mathrm{pe1}} = 10$ pu, respectively. These values are higher than the case with no droop setting i.e. $k_{\mathrm{pe1}} = 4.62$ pu. With DVC 2, the dc-side PDC decreases slightly at $\omega = 7$ pu and also decreases further at a higher frequency. This is not the case with DVC 3, where the dc-side PDC increases in most of the frequency ranges. Among the three DVCs studied, DVC 3 is the one which contributes the most to the enhancement of the system stability, as it decreases the magnitude of the dc-side PDC.

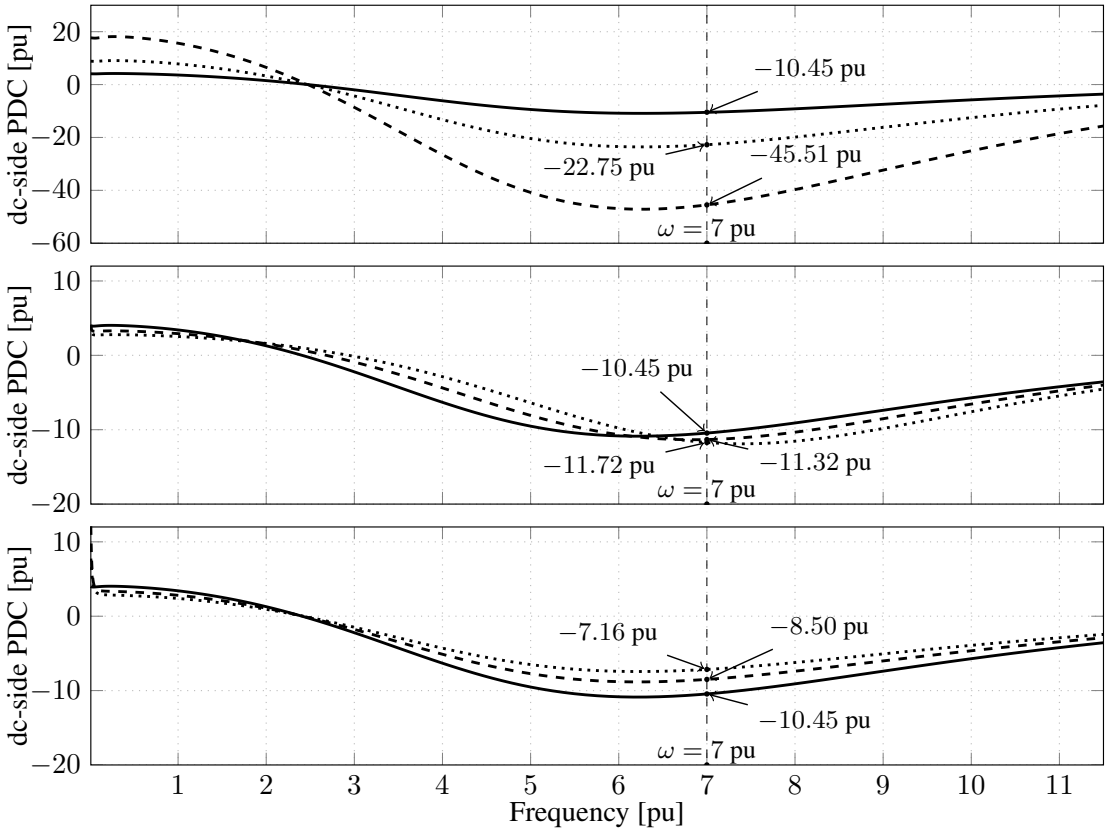

Figure 3.10: Impact of DVC 1 (upper), DVC 2 (middle), DVC3 (bottom). No droop setting (solid), $k_{\mathrm{d}} = 0.05$ (dashed) and $k_{\mathrm{d}} = 0.10$ (dotted).

3.7 Verifications through simulations

In order to verify the findings presented so far, simulations in a point-to-point VSC-HVDC system are performed. The VSC electrical and control parameters are set as specified in Section 3.6. Moreover, the VSCs are interconneted through a 50 km cable. The following cases are simulated:

Test case 1 VSCs modeled as ideal amplifiers with no delays, SCR = 5 and DVC gains set as $k_{\mathrm{pe1}} = 4.62$ pu $k_{\mathrm{ie1}} = 0.31$ pu;

Test case 2 VSCs modeled as switching devices (two level converters with a switching frequency of 2 kHz). Controller implemented with a delay time (τ) of 0.25 ms, SCR = 5, DVC gains set as $k_{\mathrm{pe1}} = 4.62$ pu $k_{\mathrm{ie1}} = 0.31$ pu;

Test case 3 Same as test case 2, but with SCR $= 3$;

Test case 4 Same as test case 2, with DVC 3 implemented ($k_{\mathrm{d}} = 0.05$ pu);

Test case 5 Same as test case 2, with lower k_{pe}.

Note that no ac-side capacitors neither LPF are considered are considered in the simulations. In all cases, VSC_2 decreases its reference $i_{\mathrm{f2}}^{d\mathrm{ref}}$ from 0 to -1 pu at a rate of -0.5 pu/s. DC-side powers and voltages of VSC_1 are plotted in Figure 3.11. In case 1, with ideal VSCs and no delays, the system turns unstable after reaching 1 pu. In case 2, when delays are considered, the figure shows that instability takes place at a lower power (around 0.8 pu), which confirms the detrimental impact of delays on the system stability. The negative impact of a lower SCR is tested in case 3. In this case the figure shows that instability occurs at an even lower power, as indicated earlier in this section. As discussed in Section 3.6, DVC 3 reduces the risk of instability, and that is confirmed with simulation case 4, where it can be seen that instability takes place at a higher power transfer. One of the conclusions from this chapter is that instability can be avoided if the size of the dc-side PDC is decreased. In case 5, this is achieved by reducing k_{pe} to 1.54 pu with $k_{\mathrm{ie}} = 0.31$ pu. Figure 3.11 shows that the system indeed becomes stable for the simulated case. Finally, Figure 3.12 shows a detailed view of e_1 and P_1 during instability conditions. The figure shows that the oscillation frequency is 352 Hz (7.04 pu), which is very close to the RF of the considered cable. This confirms again that the instability originates from the dc-network resonance.

Test case 5 shows the usefulness of the proposed modeling approach. A procedure to mitigate instability related to dc-side resonances can be: 1) Identify dc-side resonances through impedance frequency scan of the dc network. 2) Develop mitigation measures such that, at the identified frequencies, a negative dc-side PDC is avoided or at least increased.

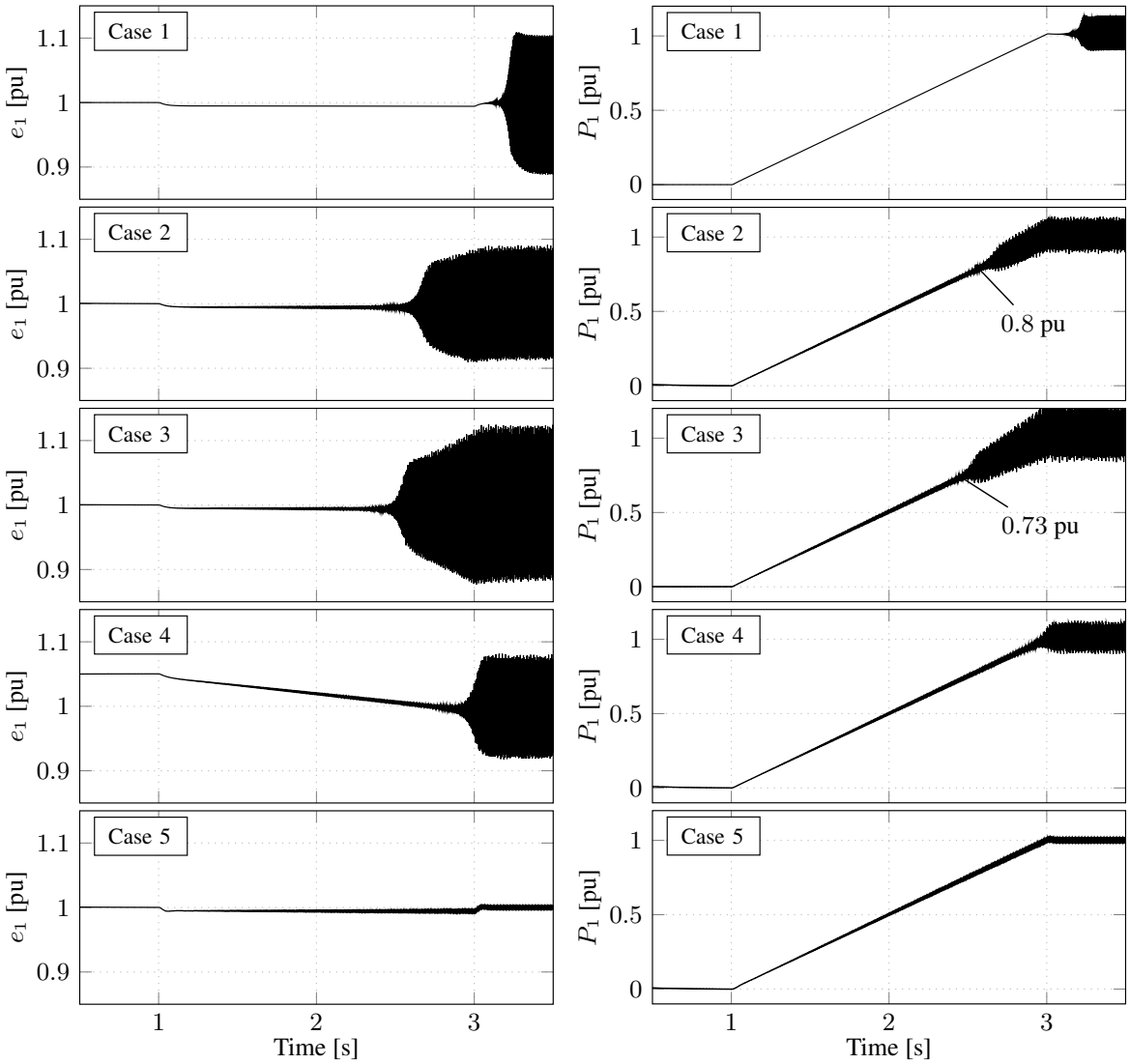

Figure 3.11: DC side voltages and powers of VSC_1 from the simulation cases.

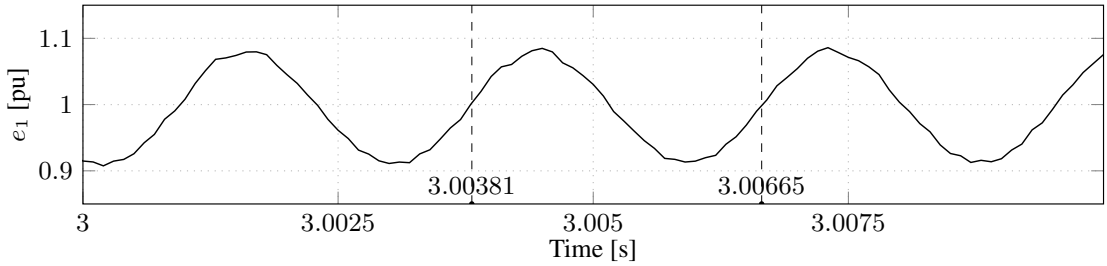

Figure 3.12: Detailed e_1 from case 2. The oscillation period is 2.84 ms (RF of 352 Hz or 7.04 pu).

3.8 Deriving F for a discrete time controller

Most control systems are implemented in digital controllers, thus, in this section, the dc-side PDC for a DVC-VSC driven by a discrete time controller is derived. Let us begin fist with the vector form of (2.6) in the synchronous *dq*-frame

$$\frac{\mathrm{d}\underline{i}_{\mathrm{f}i}^{sdq}(t)}{\mathrm{d}t} = -\frac{R_{\mathrm{f}i}}{L_{\mathrm{f}i}}\underline{i}_{\mathrm{f}i}^{sdq}(t) - \mathrm{j}\omega_0\underline{i}_{\mathrm{f}i}^{sdq}(t) + \frac{\underline{u}_{\mathrm{g}i}^{sdq}}{L_{\mathrm{f}i}} - \frac{\underline{u}_{\mathrm{c}i}^{sdq}(t)}{L_{\mathrm{f}i}} \tag{3.42a}$$

$$\frac{\mathrm{d}\underline{i}_{\mathrm{s}i}^{sdq}(t)}{\mathrm{d}t} = -\frac{R_{\mathrm{s}i}}{L_{\mathrm{s}i}}\underline{i}_{\mathrm{s}i}^{sdq}(t) - \mathrm{j}\omega_0\underline{i}_{\mathrm{s}i}^{sdq}(t) + \frac{\underline{u}_{\mathrm{s}i}^{sdq}}{L_{\mathrm{s}i}} - \frac{\underline{u}_{\mathrm{g}i}^{sdq}(t)}{L_{\mathrm{s}i}} \tag{3.42b}$$

$$\frac{\mathrm{d}\underline{u}_{\mathrm{g}i}^{sdq}(t)}{\mathrm{d}t} = -\frac{1}{C_{\mathrm{s}i}}\underline{i}_{\mathrm{f}i}^{sdq}(t) + \frac{1}{C_{\mathrm{f}i}}\underline{i}_{\mathrm{s}i}^{sdq}(t) - \mathrm{j}\omega_0\underline{u}_{\mathrm{g}i}^{sdq}(t) \tag{3.42c}$$

where ω_0 is the synchronous speed. Remember that $\underline{u}_{\mathrm{s}i}^{sdq}$ is a constant vector in the synchronous *dq*-frame. Before continuing, let us define some reference frames that are used in this section. Figure 3.13 shows the $\alpha\beta$-frame which is a stationary frame, and, as mentioned earlier, variables in this reference frame are represented as $\underline{z}$. The figure also shows the kdq-frame, which is also a stationary frame, and uses the angle estimated by the discrete-time PLL$_i$ (zPLLi), $\theta_{\mathrm{g}i}(k)$.[1] Moreover, a dq-frame is shown in Figure 3.13 whose reference

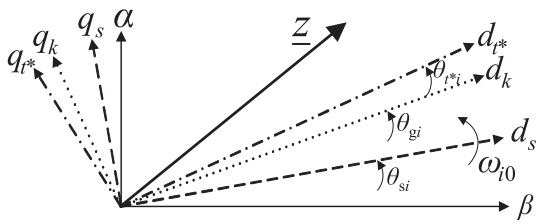

Figure 3.13: Reference frames: $\alpha\beta$-frame (solid), sdq-frame (dashed). kdq-frame (dotted). dq-frame (dashed-dotted).

frame rotates at the synchronous speed, i.e. ω_0 and its transformation angle is defined as

$$\theta_{t*i}(k, t^*) = \theta_{\mathrm{g}i}(k) + \omega_0 t^* \quad \text{with} \quad 0 \leq t^* < h \tag{3.43}$$

Finally, the earlier defined synchronous sdq-frame is also shown in Figure 3.13. This reference frame uses the angle $\theta_{\mathrm{s}i} = \theta_{i0} + t\omega_0$, which can be redefined as

$$\theta_{\mathrm{s}i}(k, t^*) = \theta_{i0} + kh\omega_0 + t^*\omega_0 \tag{3.44}$$

Then, variables in their respective reference frames can be expressed as

$$\underline{z} = \underline{z}^{sdq} e^{\mathrm{j}\theta_{\mathrm{s}i}(k,t^*)} \tag{3.45a}$$

$$\underline{z} = \underline{z}^{kdq} e^{\mathrm{j}\theta_{\mathrm{g}i}(k)} \tag{3.45b}$$

$$\underline{z} = \underline{z}^{dq} e^{\mathrm{j}\theta_{\mathrm{g}i}(k)} e^{\mathrm{j}\omega_0 t^*} \tag{3.45c}$$

[1] Note that $\theta_{\mathrm{g}i}(k)$ is constant in the time interval $kh \leq t < (k+1)h$, after which the kdq-frame is updated with the angle $\theta_{\mathrm{g}i}(k+1)$. $k \in 0, 1, 2, \ldots$, represents every step in the discrete domain.

Using (3.45), relationships between the *sdq*-frame and *dq*-frame, and *sdq* and *kdq*-frame can be obtained as follow

$$\underline{z}^{sdq} = \underline{z}^{dq} e^{\mathrm{j}\widetilde{\theta}_{\mathrm{g}}(k)} \tag{3.46a}$$

$$\underline{z}^{sdq} = \underline{z}^{kdq} e^{\mathrm{j}\widetilde{\theta}_{\mathrm{g}}(k)} e^{-\mathrm{j}\omega_0 t^*} \tag{3.46b}$$

$$\text{where} \quad \widetilde{\theta}_{\mathrm{g}i}(k) = \theta_{\mathrm{g}i}(k) - \theta_{\mathrm{g}i0} - kh\omega_0 \tag{3.46c}$$

Using (3.46), (3.42) can be expressed in the *dq*-frame as

$$\frac{\mathrm{d}\underline{i}_{\mathrm{f}i}^{dq}(t)}{\mathrm{d}t} = -\frac{R_{\mathrm{f}i}}{L_{\mathrm{f}i}}\underline{i}_{\mathrm{f}i}^{dq}(t) - \mathrm{j}\omega_0\underline{i}_{\mathrm{f}i}^{dq}(t) + \frac{\underline{u}_{\mathrm{g}i}^{dq}}{L_{\mathrm{f}i}} - \frac{\underline{u}_{\mathrm{c}i}^{kdq}(k)}{L_{\mathrm{f}i}} e^{-\mathrm{j}\omega_0 t^*} \tag{3.47a}$$

$$\frac{\mathrm{d}\underline{i}_{\mathrm{s}i}^{dq}(t)}{\mathrm{d}t} = -\frac{R_{\mathrm{s}i}}{L_{\mathrm{s}i}}\underline{i}_{\mathrm{s}i}^{dq}(t) - \mathrm{j}\omega_0\underline{i}_{\mathrm{s}i}^{dq}(t) + \frac{\underline{u}_{\mathrm{s}i}^{sdq}}{L_{\mathrm{s}i}} e^{-\mathrm{j}\widetilde{\theta}_{\mathrm{g}i}(k)} - \frac{\underline{u}_{\mathrm{g}i}^{dq}(t)}{L_{\mathrm{s}i}} \tag{3.47b}$$

$$\frac{\mathrm{d}\underline{u}_{\mathrm{g}i}^{dq}(t)}{\mathrm{d}t} = -\frac{1}{C_{\mathrm{f}i}}\underline{i}_{\mathrm{f}i}^{dq}(t) + \frac{1}{C_{\mathrm{f}i}}\underline{i}_{\mathrm{s}i}^{dq}(t) - \mathrm{j}\omega_0\underline{u}_{\mathrm{g}i}^{dq}(t) \tag{3.47c}$$

Expression (3.47) can be discretized as explained in [48]. However, let us consider some practical aspects of the controller implementation in discrete time. In EMT and RTDS models developed in this thesis, firing signals are generated through a carrier PWM method called asymmetric and synchronous sampling with an update rate twice per cycle [49]. This can be explained with the help of Figure 3.14. At t_1, samples are obtained by an analog to

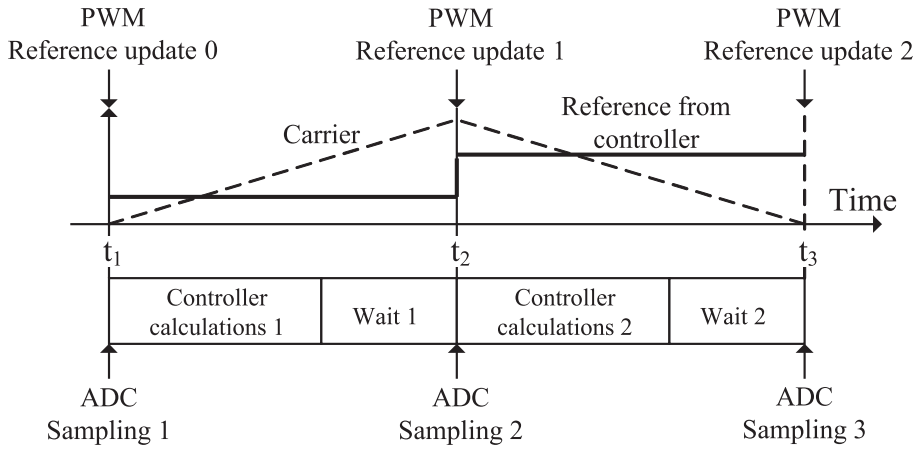

Figure 3.14: Asymmetric Synchronous PWM [49]

digital converter. With these samples, the controller performs calculations within a finite time and it waits until t_2 (half of the period) to issue the corresponding firing signals to the VSC. New samples are obtained at t_2 and the process is repeated. What this means for our model is that, voltage $\underline{u}_{\mathrm{g}i}^{kdq}(k)$ has actually been generated by the controller in the previous sampling instant, i.e. $\underline{u}_{\mathrm{c}i}^{(k-1)dq\mathrm{ref}}(k-1)$. One thing to note, however, is that, $\underline{u}_{\mathrm{c}i}^{(k-1)dq\mathrm{ref}}(k-1)$ is in the "*(k-1)dq*-frame", which uses the angle $\theta_{\mathrm{g}i}(k-1)$, while in (3.47), $\underline{u}_{\mathrm{c}i}^{kdq}(k)$ should be given in the *kdq*-frame. Therefore, $\underline{u}_{\mathrm{c}i}^{(k-1)dq\mathrm{ref}}(k-1)$ should be transformed to the *kdq*-frame as follows

$$\underline{u}_{\mathrm{c}i}^{kdq}(k) = \underline{u}_{\mathrm{c}i}^{(k\text{-})dq\mathrm{ref}}(k\text{-}) e^{-\mathrm{j}[\theta_{\mathrm{g}i}(k) - \theta_{\mathrm{g}i}(k\text{-})]} \tag{3.48}$$

where the index $k-1$ is represented as k- for the ease of notation. Let us remember that $\theta_{\mathrm{g}i}(k)$ is generated by PLL$_i$, then

$$\theta_{\mathrm{g}i}(k) - \theta_{\mathrm{g}i}(k-1) = h(\omega_0 + \omega_{\mathrm{g}i}(k-1)) \tag{3.49}$$

where $\omega_{\mathrm{g}i}(k-1)$ is the angular speed estimated by PLL$_i$ at the sampling instant $k-1$. Finally, (3.47) can be rewritten as

$$\frac{\mathrm{d}\underline{i}_{\mathrm{f}i}^{dq}(t)}{\mathrm{d}t} = -\frac{R_{\mathrm{f}i}}{L_{\mathrm{f}i}}\underline{i}_{\mathrm{f}i}^{dq}(t) - \mathrm{j}\omega_0\underline{i}_{\mathrm{f}i}^{dq}(t) + \frac{\underline{u}_{\mathrm{g}i}^{dq}}{L_{\mathrm{f}i}} - \frac{\underline{u}_{\mathrm{c}i}^{(k\text{-})dq\mathrm{ref}}(k\text{-})}{L_{\mathrm{f}i}}e^{-\mathrm{j}\omega_0(t^*+h)}e^{-\mathrm{j}h\omega_{\mathrm{g}i}(k\text{-})} \tag{3.50a}$$

$$\mathrm{d}\underline{i}_{\mathrm{s}i}^{dq}(t)\mathrm{d}t = -\frac{R_{\mathrm{s}i}}{L_{\mathrm{s}i}}\underline{i}_{\mathrm{s}i}^{dq}(t) - \mathrm{j}\omega_0\underline{i}_{\mathrm{s}i}^{dq}(t) + \frac{\underline{u}_{\mathrm{s}i}^{sdq}}{L_{\mathrm{s}i}}e^{-\mathrm{j}\widetilde{\theta}_{\mathrm{g}i}(k)} - \frac{\underline{u}_{\mathrm{g}i}^{dq}(t)}{L_{\mathrm{s}i}} \tag{3.50b}$$

$$\frac{\mathrm{d}\underline{u}_{\mathrm{g}i}^{dq}(t)}{\mathrm{d}t} = -\frac{1}{C_{\mathrm{s}i}}\underline{i}_{\mathrm{f}i}^{dq}(t) + \frac{1}{C_{\mathrm{f}i}}\underline{i}_{\mathrm{s}i}^{dq}(t) - \mathrm{j}\omega_0\underline{u}_{\mathrm{g}i}^{dq}(t) \tag{3.50c}$$

In matrix form, the linearized version of (3.50) can be expressed as

$$\frac{\mathrm{d}\mathbf{x}_i^{\mathrm{t}}}{\mathrm{d}t} = \mathbf{A}_i^{\mathrm{t}}\mathbf{x}_i^{\mathrm{t}} + \mathbf{B}_{\theta i}^{\mathrm{t}}\Delta\widetilde{\theta}_{\mathrm{g}i}(k) + \mathbf{B}_{\mathrm{uc}i}^{\mathrm{t}}(t^*)\mathbf{u}_{\mathrm{c}i}(k) + \mathbf{B}_{\omega i}^{\mathrm{t}}(t^*)\Delta\omega_{\mathrm{g}i}^*(k) \tag{3.51}$$

with

$$\mathbf{x}_i^{\mathrm{t}} = \left[\Delta i_{\mathrm{f}i}^d\ \Delta i_{\mathrm{f}i}^q\ \Delta i_{\mathrm{s}i}^d\ \Delta i_{\mathrm{s}i}^q\ \Delta u_{\mathrm{g}i}^d\ \Delta u_{\mathrm{g}i}^q\right]^{\mathrm{T}}, \quad \mathbf{u}_{\mathrm{c}i}(k) = \left[\Delta u_{\mathrm{c}i}^{kd*}\ \Delta u_{\mathrm{c}i}^{kq*}\right]^{\mathrm{T}},$$

$$\mathbf{A}_i^{\mathrm{t}} = \begin{bmatrix} -\frac{R_{\mathrm{f}i}}{L_{\mathrm{f}i}} & \omega_0 & 0 & 0 & \frac{1}{L_{\mathrm{f}i}} & 0 \\ -\omega_0 & -\frac{R_{\mathrm{f}i}}{L_{\mathrm{f}i}} & 0 & 0 & 0 & \frac{1}{L_{\mathrm{f}i}} \\ 0 & 0 & -\frac{R_{\mathrm{s}i}}{L_{\mathrm{s}i}} & \omega_0 & \frac{1}{L_{\mathrm{s}i}} & 0 \\ 0 & 0 & -\omega_0 & -\frac{R_{\mathrm{s}i}}{L_{\mathrm{s}i}} & 0 & \frac{1}{L_{\mathrm{s}i}} \\ -\frac{1}{C_{\mathrm{f}i}} & 0 & \frac{1}{C_{\mathrm{f}i}} & 0 & 0 & \omega_0 \\ 0 & -\frac{1}{C_{\mathrm{f}i}} & 0 & \frac{1}{C_{\mathrm{f}i}} & -\omega_0 & 0 \end{bmatrix}, \quad \mathbf{B}_{\theta i}^{\mathrm{t}} = \begin{bmatrix} 0 \\ 0 \\ \frac{u_{\mathrm{s}i0}^{sq}}{L_{\mathrm{s}i}} \\ -\frac{u_{\mathrm{s}i0}^{sd}}{L_{\mathrm{s}i}} \\ 0 \\ 0 \end{bmatrix},$$

$$\mathbf{B}_{\mathrm{uc}i}^{\mathrm{t}}(t^*) = \begin{bmatrix} -\frac{\cos(\omega_0[t^*+h])}{L_{\mathrm{f}i}} & -\frac{\sin(\omega_0(t^*+h))}{L_{\mathrm{f}i}} \\ \frac{\sin(\omega_0[t^*+h])}{L_{\mathrm{f}i}} & -\frac{\cos(\omega_0(t^*+h))}{L_{\mathrm{f}i}} \\ 0 & 0 \\ 0 & 0 \\ 0 & 0 \\ 0 & 0 \end{bmatrix}, \ \mathbf{B}_{\omega i}^{\mathrm{t}}(t^*) = \begin{bmatrix} -h\left(\frac{u_{\mathrm{c}i0}^q\cos(\omega_0[t^*+h]) - u_{\mathrm{c}i0}^d\sin(\omega_0[t^*+h])}{L_{\mathrm{f}i}}\right) \\ h\left(\frac{u_{\mathrm{c}i0}^q\sin(\omega_0[t^*+h]) + u_{\mathrm{c}i0}^d\cos(\omega_0[t^*+h])}{L_{\mathrm{f}i}}\right) \\ 0 \\ 0 \\ 0 \\ 0 \end{bmatrix}$$

where $u_{\mathrm{c}i}^{kd*}(k) = u_{\mathrm{c}i}^{(k-1)d}(k-1)$, $u_{\mathrm{c}i}^{kq*}(k) = u_{\mathrm{c}i}^{(k-1)q}(k-1)$, and $\omega_{\mathrm{g}i}^*(k) = \omega_{\mathrm{g}i}(k-1)$. Then, (3.51) can be discretized as [48]

$$\mathbf{x}_i^{\mathrm{k}}(k+1) = \mathbf{A}_i^{\mathrm{k}}\mathbf{x}_i^{\mathrm{k}}(k) + \mathbf{B}_{\theta i}^{\mathrm{k}}\Delta\widetilde{\theta}_{\mathrm{g}i}(k) + \mathbf{B}_{\mathrm{uc}i}^{\mathrm{k}}\mathbf{u}_{\mathrm{c}i}(k) + \mathbf{B}_{\omega i}^{\mathrm{k}}\Delta\omega_{\mathrm{g}i}^*(k) \tag{3.52}$$

with

$$\mathbf{x}_i^{\mathrm{k}}(k) = \left[\Delta i_{\mathrm{f}i}^d(k)\ \Delta i_{\mathrm{f}i}^q(k)\ \Delta i_{\mathrm{s}i}^d(k)\ \Delta i_{\mathrm{s}i}^q(k)\ \Delta u_{\mathrm{g}i}^d(k)\ \Delta u_{\mathrm{g}i}^q(k)\right]^{\mathrm{T}},$$

$$\mathbf{A}_i^{\mathrm{k}} = e^{\mathbf{A}_i^{\mathrm{t}}h}, \quad \mathbf{B}_{\theta i}^{\mathrm{k}} = \left[\mathbf{A}_i^{\mathrm{t}}\right]^{-1}\left(e^{\mathbf{A}_i^{\mathrm{t}}h} - \mathbf{I}\right)\mathbf{B}_{\theta i}^{\mathrm{t}}, \quad \mathbf{B}_{\mathrm{uc}i}^{\mathrm{k}} = \int_0^h e^{\mathbf{A}_i^{\mathrm{t}}t^*}\mathbf{B}_{\mathrm{uc}i}^{\mathrm{t}}(t^*)dt^*$$

$$\mathbf{B}_{\omega i}^{\mathrm{k}} = \int_0^h e^{\mathbf{A}_i^{\mathrm{t}}t^*}\mathbf{B}_{\omega i}^{\mathrm{t}}(t^*)dt^*$$

Now, let us continue with the discrete time controller. The PLL shown in (2.14) can be discretized using the Forward-Euler method. Then, the angle $\theta_{\mathrm{g}i}(k)$ is

$$\theta_{\mathrm{g}i}(k+1) = \theta_{\mathrm{g}i}(k) + h(\omega_0 + k_{\mathrm{pl}i}u^q_{\mathrm{g}i}(k) + n_{\omega i}(k)) \tag{3.53a}$$
$$n_{\omega i}(k+1) = n_{\omega i}(k) + hk_{\mathrm{il}i}u^q_{\mathrm{g}i}(k). \tag{3.53b}$$

Replacing (3.53) into (3.46c) for $k+1$, the following is obtained in small signal terms

$$\Delta\tilde{\theta}_{\mathrm{g}i}(k+1) = \Delta\tilde{\theta}_{\mathrm{g}i}(k) + h(k_{\mathrm{pl}i}\Delta u^q_{\mathrm{g}i}(k) + \Delta n_{\omega i}(k)) \tag{3.54a}$$
$$\Delta n_{\omega i}(k+1) = \Delta n_{\omega i}(k) + hk_{\mathrm{il}i}\Delta u^q_{\mathrm{g}i}(k). \tag{3.54b}$$
$$\Delta\omega_{\mathrm{g}i}(k) = k_{\mathrm{pl}i}\Delta u^q_{\mathrm{g}i}(k) + \Delta n_{\omega i}(k) \tag{3.54c}$$

Likewise, VCC_i shown in Figure 2.3 can be discretized as

$$m^d_i(k+1) = m^d_i(k) + hk_{\mathrm{i}i}\big(\Delta i^{d\mathrm{ref}}_{\mathrm{f}i}(k) - \Delta i^d_{\mathrm{f}i}(k)\big) \tag{3.55a}$$
$$m^q_i(k+1) = m^q_i(k) + hk_{\mathrm{i}i}\big(\Delta i^{q\mathrm{ref}}_{\mathrm{f}i}(k) - \Delta i^q_{\mathrm{f}i}(k)\big) \tag{3.55b}$$
$$\begin{aligned}\Delta u^{kd\mathrm{ref}}_{\mathrm{c}i}(k) = {} & -k_{\mathrm{p}i}\Delta i^d_{\mathrm{f}i}(k) + \omega_0 L_{\mathrm{f}i}\Delta i^q_{\mathrm{f}i}(k) + \Delta u^d_{\mathrm{gfil}i}(k) - m^d_i(k) \\ & + i^q_{\mathrm{f}i0}L_{\mathrm{f}i}\Delta\omega_{\mathrm{g}i}(k) - k_{\mathrm{p}}\Delta i^{d\mathrm{ref}}_{\mathrm{f}i}(k)\end{aligned} \tag{3.56a}$$
$$\begin{aligned}\Delta u^{kq\mathrm{ref}}_{\mathrm{c}i}(k) = {} & -\omega_0 L_{\mathrm{f}i}\Delta i^d_{\mathrm{f}i}(k) - k_{\mathrm{p}i}\Delta i^q_{\mathrm{f}i}(k) + \Delta u^q_{\mathrm{gfil}i}(k) - m^q_i(k) \\ & - i^d_{\mathrm{f}i0}L_{\mathrm{f}i}\Delta\omega_{\mathrm{g}i}(k) - k_{\mathrm{p}i}\Delta i^{q\mathrm{ref}}_{\mathrm{f}i}(k)\end{aligned} \tag{3.56b}$$

To connect (3.56) with (3.52), the following can be made

$$\Delta u^{kd*}_{\mathrm{c}i}(k+1) = \Delta u^{d\mathrm{ref}}_{\mathrm{c}i}(k) \tag{3.57a}$$
$$\Delta u^{kq*}_{\mathrm{c}i}(k+1) = \Delta u^{q\mathrm{ref}}_{\mathrm{c}i}(k) \tag{3.57b}$$
$$\Delta\omega^*_{\mathrm{g}i}(k+1) = \Delta\omega_{\mathrm{g}i}(k) \tag{3.57c}$$

The DVC is defined by

$$\Delta i^{d\mathrm{ref}}_{\mathrm{f}i}(k) = k_{\mathrm{pe}i}\big(\Delta e^{\mathrm{ref}}_i(k) - \Delta e_i(k)\big) + n_{\mathrm{e}i}(k) \tag{3.58a}$$
$$n_{\mathrm{e}i}(k+1) = n_{\mathrm{e}i}(k) + hk_{\mathrm{ie}}\big(\Delta e^{\mathrm{ref}}_i(k) - \Delta e_i(k)\big). \tag{3.58b}$$

and the discretized LPF is

$$u^d_{\mathrm{gfil}i}(k+1) = u^d_{\mathrm{gfil}i}(k) + h\alpha_{\mathrm{f}i}\big(u^d_{\mathrm{g}i}(k) - u^d_{\mathrm{gfil}i}(k)\big) \tag{3.59a}$$
$$u^q_{\mathrm{gfil}i}(k+1) = u^q_{\mathrm{gfil}i}(k) + h\alpha_{\mathrm{f}i}\big(u^q_{\mathrm{g}i}(k) - u^q_{\mathrm{gfil}i}(k)\big) \tag{3.59b}$$

The current Δi^*_i injected by VSC_i is expressed as

$$\Delta i^*_i(k) = \frac{u^d_{\mathrm{c}i0}}{e_{i0}}\Delta i^d_{\mathrm{f}i}(k) + \frac{u^q_{\mathrm{c}i0}}{e_{i0}}\Delta i^q_{\mathrm{f}i}(k) + \frac{i^d_{\mathrm{f}i0}}{e_{i0}}\Delta u^{kd*}_{\mathrm{c}i}(k) + \frac{i^q_{\mathrm{f}i0}}{e_{i0}}\Delta u^{kq*}_{\mathrm{c}i}(k) \tag{3.60}$$

Finally, using (3.52), (3.54), (3.55), (3.56), (3.57),(3.58), (3.59) and (3.60) a discrete time state space model can be formed as

$$\mathbf{x}_i(k+1) = \mathbf{A}_{ki}\mathbf{x}_i(k) + \mathbf{B}_{ki}\mathbf{r}_i(k) + \mathbf{B}^{\mathrm{e}}_{ki}\Delta e_i(k) \tag{3.61}$$
$$\Delta i^*_i = \mathbf{C}_{ki}\mathbf{x}_i(k) + \mathbf{D}_{ki}\mathbf{r}_i(k) + \mathbf{D}^{\mathrm{e}}_{ki}\Delta e_i(k) \tag{3.62}$$

with $\mathbf{x}_i = \left[[\mathbf{x}_i^k]^{\mathrm{T}}\ \Delta i_{\mathrm{f}}^d\ \Delta i_{\mathrm{f}}^d\ \Delta m_i^d\ \Delta m_i^q\ \ \Delta n_{\omega i}\ \Delta\tilde{\theta}_{\mathrm{g}i}\ \Delta n_{\mathrm{e}i}\ \Delta u_{\mathrm{c}i}^{kd*}\ \Delta u_{\mathrm{c}i}^{kq*}\ \Delta\omega_{\mathrm{g}i}^*\ u_{\mathrm{gfil}i}^d\ u_{\mathrm{gfil}i}^d\right]^{\mathrm{T}}$ and $\mathbf{r} = [\Delta e_i^{\mathrm{ref}}\ \Delta i_{\mathrm{f}i}^{q\mathrm{ref}}]$ (the argument (k) is dropped for the sake of simplicity). $\mathbf{A}_k$, $\mathbf{B}_k$, $\mathbf{B}_k^{\mathrm{e}}$, $\mathbf{C}_k$, $\mathbf{D}_k$ and $\mathbf{D}_k^{\mathrm{e}}$ can be found by manipulating the above expressions and using tools such as Matlab®. Then, the transfer function that defines the dc-side PDA is

$$-\frac{\Delta i_i^*}{\Delta e_i} = -\frac{\Delta P_i}{\Delta e_i} = -\left[\mathbf{C}_{ki}\big(z\mathbf{I} - \mathbf{A}_{ki}\big)^{-1}\mathbf{B}_{ki}^{\mathrm{e}}\right] \tag{3.63}$$

where z is the z-transform operator.[1] The frequency response of (3.63) is obtained by making $z = e^{\mathrm{j}\omega}$.

3.9 Measurement of the dc-side PDA in an EMT model

In order to verify the validity of the mathematical derivation of the dc-side PDA, comparisons with measurements in EMT models are performed. In the EMT models, the digital controller described in the previous section is implemented and the VSC electrical configuration is as described in Section 2.1.1. To measure the dc-side PDA, the setup depicted in Figure 3.15 is implemented in the EMT model. As illustrated in the figure, the reference to the DVC is set to zero, and a sinusoidal signal is applied to the feedback input, e_1. The dc-side PDA depends on the amount of power injected by VSC_1; therefore, a constant signal, $i_{\mathrm{f}10}^d$, is added to the VCC input to make VSC_1 to inject power. This signal has no impact on the measured dc-side PDA since, when considering small signal terms, $\Delta i_{\mathrm{f}10}^d$ is zero. The power injected by VSC_1, P_1, is measured, and the corresponding sinusoidal component is obtained through Discrete Fourier Transform. Finally, the VSC dc-side is connected to a constant dc source in order to speed up the simulation.

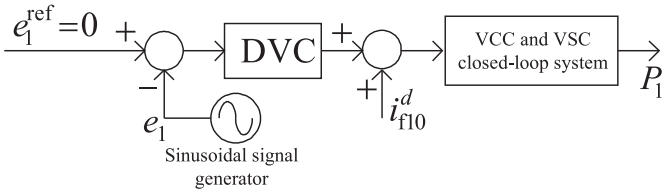

Figure 3.15: DC-side PDA measurement setup.

The dc-side PDA is measured for two EMT models. The first one, called ideal EMT model, is a VSC system, including discretized controllers, where the converter is modelled as an ideal linear amplifier only, as in Figure 2.8. The second one, called nonideal EMT model, is a VSC system where a two-level VSC, with switches, is implemented. In both cases, the ac system SCR is 5, $i_{\mathrm{f}10}^d$ is $+1$ pu, there is no ac side capacitor, no LPF, and the sampling frequency is 4 kHz. The controller is modelled as in Section 3.8 with parameters as indicated in Table 2.4, and $k_{\mathrm{pe1}} = 9.23$ and $k_{\mathrm{ie1}} = 1.23$. Measurements are performed for frequencies from 1 pu to 10 pu, in steps of 1 pu. A comparison between the measurements and the corresponding theoretical dc-side PDA is shown in Figure 3.16. As expected,

[1] Do not confuse the z operator with $\underline{z}$ used previously to denote an arbitrary two component vector.

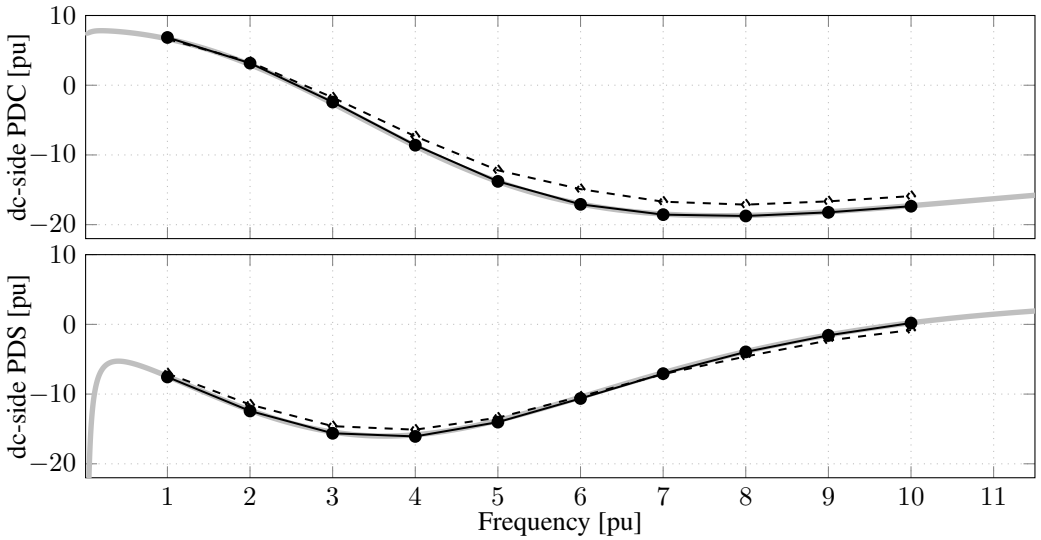

Figure 3.16: DC-side PDA measurement for a DVC-VSC with an ac system of SCR = 5, no ac-side capacitor, no LPF, and $i^d_{\mathrm{f10}} = +1$ pu. Theoretical model (gray solid), ideal VSC (black solid), switching model VSC (black dashed).

the dc-side PDA from the ideal EMT model of the VSC matches very closely with the theoretical model since they are, in principle, the same. That is, the ideal EMT model is nonlinear, while the theoretical model is a linearized version of the former. The dc-side PDA of the nonideal EMT model shows small deviations from the theoretical model. This is due to the fact that anti-aliasing filters are introduced in the nonideal EMT model. Moreover, the switching actions do not take place immediately after the controller changes its output reference. This causes a small delay that also impacts on the dc-side PDA. Other factors that might cause the observed differences are extra losses in the converter.

Another comparison is now performed considering an SCR $= 5$, an ac-side capacitor $C_{\mathrm{f1}} = 0.4$ pu, and a LPF with $\alpha_{\mathrm{f1}} = 4$ pu. The controller is set as mentioned above, but with the DVC gains set as $k_{\mathrm{pe1}} = 1.54$ pu and $k_{\mathrm{ei1}} = 0.31$ pu. Similarly to the previous case, the dc-side PDA is calculated theoretically, and then measured in an ideal EMT and a nonideal EMT model. Results are shown in Figure 3.17 for the case with $i^d_{\mathrm{f10}} = +1$ pu. Again, excellent agreement is observed between the theoretical dc-side PDA and the ideal EMT model. However, differences can be appreciated with the nonideal EMT model, especially between the frequencies of 1–2 pu and for frequencies over 6 pu. One more comparison is made for this same setup is shown in Figure 3.18, but with $i^d_{\mathrm{f10}} = -1$ pu. Again, good agreement is seen between the theoretical and the ideal EMT model, but differences are observed with the nonideal EMT model between frequencies of 0.5–2 pu and for frequencies beyond 6 pu. I should be mentioned that, aside from the reasons for these differences explained above, the signals obtained from the measurements for this particular electrical configuration (SCR $= 5$ and $C_{\mathrm{f1}} = 0.4$ pu) contains high levels of harmonics so post processing filtering is performed. This might also cause differences in the cases compared.

The comparisons show a very good agreement between the theoretical dc-side PDC and PDS obtained using (3.63) and through measurements in the corresponding ideal EMT model. The nonideal EMT model presents some differences, but, they are due to the fact

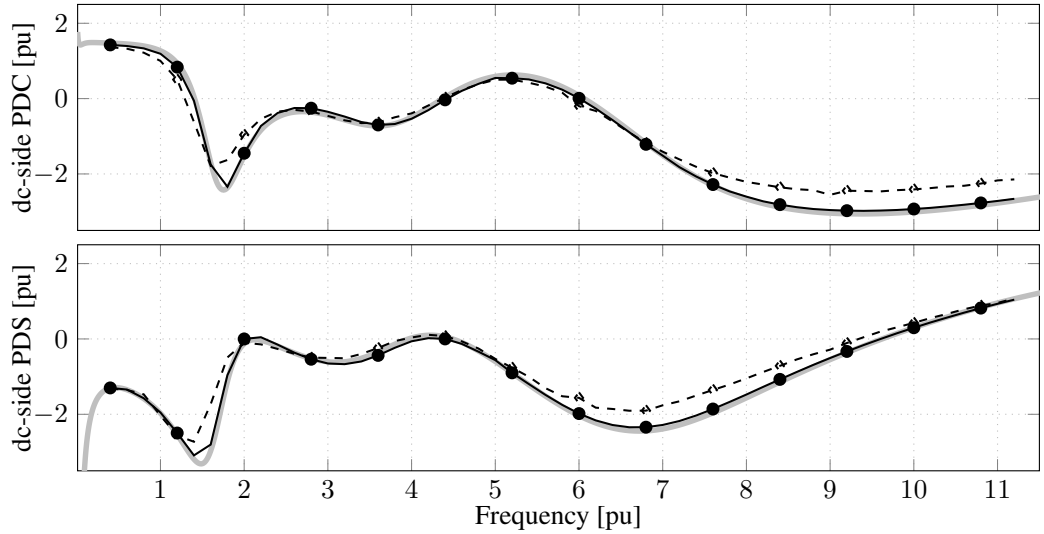

Figure 3.17: DC-side PDA measurement for a DVC-VSC with an ac system of SCR $= 5$, ac-side capacitor $C_{\mathrm{f1}} = 0.4$ pu, LPF with $\alpha_{\mathrm{f1}} = 4$ pu, and $i^d_{\mathrm{f10}} = +1$ pu. Theoretical model (gray solid), ideal VSC (black solid), switching model VSC (black dashed).

that they reflect additional complexity not considered in the theoretical model. Moreover, especially in the case where an ac-side capacitor is included, differences are appreciated in some frequencies. High harmonic levels are observed and this might be causing the differences. While there are differences, the nonideal EMT model still follows the trend and it is relatively close to the theoretical ones. The reasons observed, especially at low frequencies, should be further investigated. Then, from the comparison, it can be concluded that the dc-side PDA can be measured in an EMT model with a high degree confidence. The converse is also true, i.e. theoretical models can be used to derived the dc-side PDA, and then used in stability studies, with verifications performed accordingly.

For more complex control systems, stability analysis can be carried out by measuring the dc-side PDA, especially for frequencies around the dc-network resonance. The advantage of obtaining the dc-side PDA of one single VSC, compared to modelling the full point-to-point VSC-HVDC system to perform stability studies is obvious. On the one hand, to perform a stability study in a traditional way, several simulations must be carried out, where all elements, VSCs and transmission lines, are included. On the other hand, it is shown in this chapter that stability analysis can be performed by obtaining the dc-side PDA and compare it with frequency response of G_0. For measuring the dc-side PDA only one single VSC needs to be modelled, which avoids the cumbersome task of performing simulations on a full model of a point-to-point HVDC system. Another advantage is that, even if the dc-network characteristics are unknown, the dc-side PDC still clearly shows frequencies at which there is a risk of instability (i.e. when $\mathrm{re}[F(\mathrm{j}\omega)] < 0$). Thus, at the design stage, modifications can be performed such that the dc-side PDC is "lifted" at certain frequencies of interest. Moreover, if a mathematical model cannot be derived due to lack of knowledge of the VSC system, measurement can still be performed in black box models in order to obtain the VSC dc-side PDA.

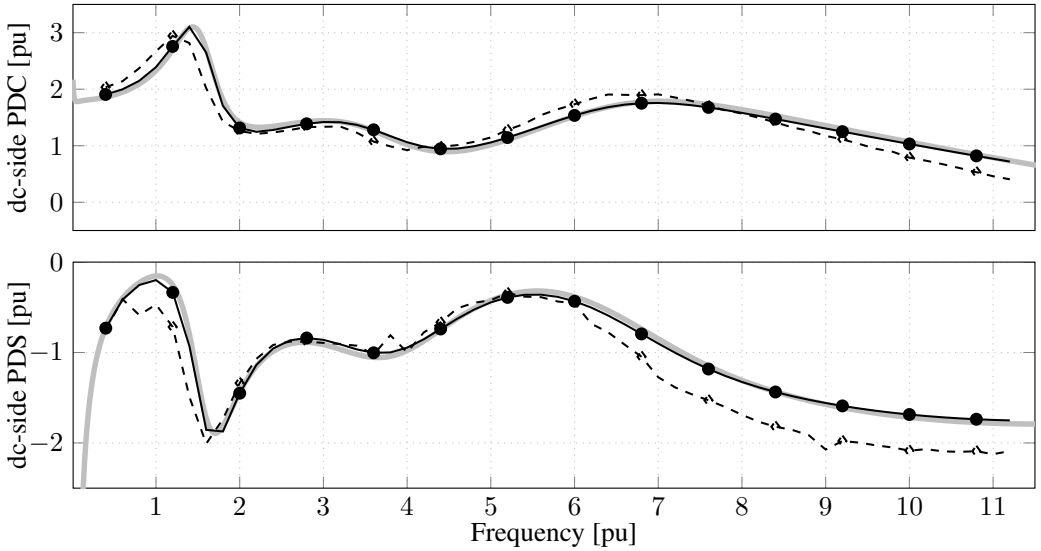

Figure 3.18: DC-side PDA measurement for a DVC-VSC with an ac system of SCR $= 5$, ac-side capacitor $C_{\mathrm{f1}} = 0.4$ pu, LPF with $\alpha_{\mathrm{f1}} = 4$ pu, and $i^d_{\mathrm{f10}} = -1$ pu. Theoretical model (gray solid), ideal VSC (black solid), switching model VSC (black dashed).

3.10 Conclusions

In this chapter, the dc-side dynamics of the point-to-point VSC-HVDC system has been studied using a frequency domain approach. The VSC-HVDC system has been modelled as a SISO feedback system, in which two subsystems have been defined: the VSC and the dc-network subsystems. The corresponding transfer functions have been derived and their passivity properties have been studied. It has been shown that the dc-network subsystem is an unstable system which can be approximated to a marginally stable system, G_0. G_0 has been found to be a passive subsystem, meaning that it is not the source of the instability. However, the dc-network subsystem presents a resonance which interacted with the VSC subsystem. The VSC subsystem has been found passive when the VSC that controls the dc-bus voltage, absorbs power from the dc grid. This means that, when the VSC absorbs power from the dc side, the system is stable even for high DVC gains. The VSC subsystem is non passive when the VSC injects current into the dc grid which means that there is a risk that the dc-network resonance becomes amplified due to the non passive behaviour of the VSC subsystem.

A VSC dc-side PDA has been also defined in this chapter. It has been shown that in the unstable cases, the VSC-subsystem presents a negative dc-side PDC at the frequencies of interest. When the dc-network resonance encounters a negative dc-side PDC, the resonance can be amplified depending on the size of the negative dc-side PDC. It has been shown that the following influences the magnitude of a negative dc-side PDC:

1. The amount of active power injected by the VSC into the dc grid. The more power is injected into the dc grid, the more negative the VSC conductance;

2. The DVC proportional gain. The higher the DVC proportional gain, the more negative the dc-side PDC;

3. The SCR of the ac system to which the VSC it is connected. The weaker the ac system, the more negative the dc-side PDC;

4. Control system delays. The higher the delays the more negative the dc-side PDC in some specific ranges. However, it has been also shown that delays can actually turn the dc-side PDC positive in the dc-network RF but at the expense of decreasing the dc-side PDC further at other frequencies;

5. Other DVC strategies. Different ways of implemented droop controllers can have an impact on the size of the dc-side PDC.

Finally, the analysis has been extended to VSCs driven by discrete time controllers. Theoretically obtained dc-side PDA has been compared with measurements performed in a corresponding EMT model. The comparison showed good agreement between both meaning that either a theoretical or a measured dc-side PDA could be used to perform stability analysis. The analysis of the defined dc-side PDA has been performed for a particular control system. However, this method is not restricted to the control system assumed in this chapter. The advantage of measuring the dc-side PDA is that simulation of a fully modelled point-to-point VSC-HVDC system can be avoided, by performing simulations in one single VSC to obtain the corresponding dc-side PDA. Moreover, if a theoretical model cannot be developed due to non availability of information, measurements can be performed in black box models to obtain the VSC dc-side PDA.

Chapter 4

Analysis through Nyquist stability criterion

In Chapter 2, the use of the dc-network characteristics, represented by the transfer function $G_0(s)$, has been only employed to determine the RFs. These RFs are then used to check if the dc-side PDC is negative at these frequencies, and, if so, it is claimed that there is a risk of instability. The more negative the dc-side PDC, the greater the risk of instability. However, a measure of how negative the dc-side PDC should be for the system to be unstable has not been provided. It is shown in this section that the RP of G_0 provides a good measure of the maximum allowable size of the dc-side PDC such that instability is avoided. Then, the dc-network resonance characteristics, i.e. RF and RP, are studied for dc link topologies composed of a combination of dc cables, OHL and dc-side filters. Finally, based on the analysis performed in this chapter, mitigation measures are suggested. This chapter is based on the work presented in Papers V and VII.

4.1 Analysis in a VSC connected to a strong ac system

As an example, the point-to-point VSC-HVDC system studied in previous chapters is analyzed for the case where the VSCs are connected to strong ac sources. Let us start with the Nyquist plot of G_0 (for positive ω), shown in Figure 4.1 for lengths of 25 km, 50 km and 100 km of the earlier studied dc cable (see Table 2.2). The figure shows that, at very low frequencies, the curve is parallel to the imaginary axis since the dc-network capacitance is dominant. As the frequency approaches the dc-side RF, the curve describes an encirclement, which converges to the origin for very high frequencies. Although not shown in Figure 4.1, it is important to note that, for the 100 km cable case, the encirclement takes place for frequencies between $3-5$ pu, for 50 km between $5-8$ pu, and for 25 km between $8-10$ pu. Figure 4.2 shows the Nyquist plots of the VSC subsystem transfer function $F(s)$, given by (3.38), for positive ω and for three values of P_1: 0, $+0.5$ pu and $+1$ pu;[1] the VSC is connected to an infinitely strong ac source, with DVC PI gains of 9.23 pu and 1.23 pu, re-

[1]Remember that a positive P_1 means VSC_1 injects power into the dc-line

spectively. For very low frequencies, F is parallel to the imaginary axis due to the integral term of the DVC; then, the curve describes a circle-like path as the frequency increases. Finally, for very high frequencies, F lies on the real axis.

Let us consider only F when $P_1 = +1$ pu for analysis purposes. Segments of F corresponding to every cable RF (25 km, 50 km and 100 km) are highlighted in Figure 4.2. As can be seen from the figure, F does not vary largely around the respective RFs. This allows us to approximate G_0 and F around the RF as

$$G_0(\mathrm{j}\gamma) = g_0\angle\theta_0 + g_{0c}(\gamma)\angle\theta(\gamma) \tag{4.1}$$

$$F(\mathrm{j}\gamma) = f_0\angle\phi_0 \tag{4.2}$$

where γ represents the set of frequencies that are around the dc-side RF. In this case, $g_0\angle\theta_0$ is the center of the encirclement and $g_{0c}(\gamma)\angle\theta(\gamma)$ is the encirclement defined by the resonance characteristic with "radius" $g_{0c}(\gamma)$. $F(\mathrm{j}\gamma)$ is approximated as a constant vector $f_0\angle\phi_0$. Therefore, the open-loop frequency response, around the RF, is approximately

$$F(\mathrm{j}\gamma)G_0(\mathrm{j}\gamma) = f_0 g_0\angle(\theta_0 + \phi_0) + f_0 g_{0c}(\gamma)\angle(\theta(\gamma) + \phi_0). \tag{4.3}$$

Equation (4.3) shows that the center of the circle defined by G_0 is displaced to $f_0 g_0\angle(\theta_0 + \phi_0)$ and the radius is increased by f_0. For $90^\mathrm{o} < \phi_0 < 270^\mathrm{o}$ (i.e. $\mathrm{re}[F(\mathrm{j}\omega) < 0]$) the circle defined by $G_0(\mathrm{j}\gamma)$ displaces to the second and third quadrant, which means that FG_0 crosses the negative real axis point in a clockwise direction. If either f_0 or $g_{0c}(\gamma)$ are large enough, FG_0 can enclose the point -1, meaning that the system is unstable. The displacement and increase of the resonance characteristic are observed in Figure 4.3, where the Nyquist plot of FG_0 shows that the circle radius from G_0 has been amplified around 10 times. This amplification corresponds approximately to the value of F at those frequencies (see Figure 4.2). Figure 4.3 demonstrates that, for a cable of 50 km, the system is unstable for VSC_1 injecting 1 pu power, which confirms the instability shown in Figure 2.5(a). Observe also that the size of FG_0 depends on the size of the dc-side RP, which means that, it is not only a negative dc-side PDC, which makes the system prone to instability, but also the magnitude of the dc-side RP.

In previous sections it has been concluded that a negative dc-side PDC represents a risk of instability and that the risk is higher if this dc-side PDC is more negative. With the analysis provided in this section, it can be seen that the corresponding dc-side RP represents a limit of how negative the dc-side PDC can be. That is, if the dc-side RP is large, the size of the dc-side PDC has to be small for the system to remain stable, and vice-versa. This is further clarified in the next section.

4.2 Impact of the dc-network resonance peak

From Figures 4.1 and 4.2, the worst case would be that at the RF, ω^r, the angle ϕ_0 from (4.2) is 180^o, then $F(\mathrm{j}\omega^\mathrm{r}) = -f_0$. Moreover, in a worst case scenario $G_0(\mathrm{j}\omega^\mathrm{r}) = Z_\mathrm{peak}\angle 0^\mathrm{o}$. Then, $F(\mathrm{j}\omega^\mathrm{r})G_0(\mathrm{j}\omega^\mathrm{r})$ would cross the real axis at $-f_0 Z_\mathrm{peak}$. Making $f_0 = |F(\mathrm{j}\gamma)|_\mathrm{max}$[1]

[1] $|F(\mathrm{j}\gamma)|_\mathrm{max}$ is the maximum value of $F(\mathrm{j}\omega)$ for frequencies around the resonance, i.e. γ.

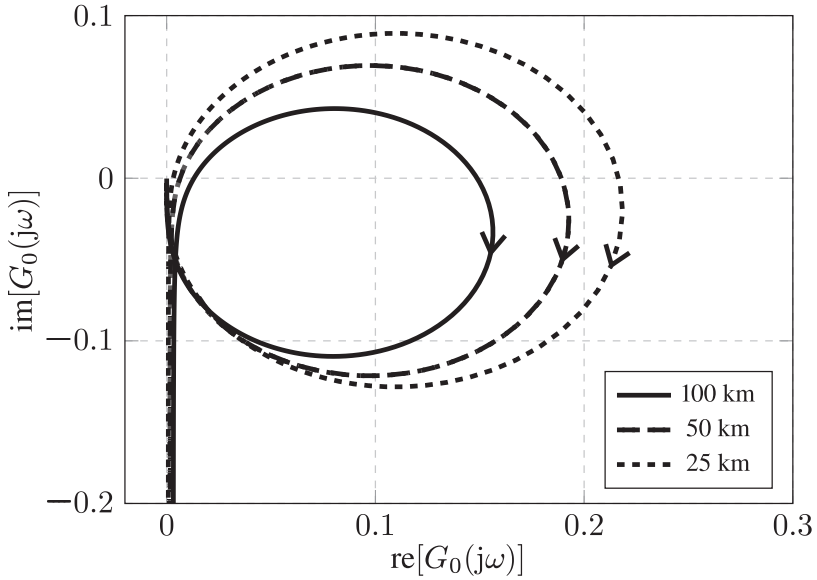

Figure 4.1: Nyquist plots of G_0 for cable lengths of 25 km, 50 km and 100 km.

and considering Nyquist stability criterion, a conservative approach to quantify $|F|$ can be proposed in order to avoid instability. Around the RF, F should fulfill

$$|F(\mathrm{j}\gamma)|_{\max} < \frac{1}{\mathrm{Z}_{\mathrm{peak}}} \tag{4.4}$$

where $\mathrm{Z}_{\mathrm{peak}}$ is the RP of the impedance seen from the point where the VSC is connected. For the particular control system described in Section 2.1.2, and considering that VSC_1 is connected to a strong ac source, it can be shown that the closed loop system is stable if

$$\frac{\alpha_1 |i^d_{\mathrm{f10}}| L_{\mathrm{f1}} k_{\mathrm{pe1}}}{e_{10}} < \frac{1}{\mathrm{Z}_{\mathrm{peak}}} \tag{4.5}$$

Then, (4.5) shows that, for a given VSC subsystem, the system stability is determined by the size of Z_{peak}. Therefore, it is of interest to study the impact on the dc-side RP of other dc-transmission, such as OHL and dc side filters. Moreover, distributed parameter models have other resonance characteristics compared to the Π-section models studied so far. All these aspects are studied in the following section.

4.3 Impact of the dc-network configuration on G_0

The data assumed to model geometrically a dc cable is based on typical values for ac cables such as in [50]. The inner layer is assumed to be aluminum conductor with a resistivity of 39.12 n$\Omega\times$m and cross section area of 2000 mm^2 (corresponding to an ampacity of 1 kA). The second layer is an insulator, assumed to be XLPE, with relative permittivity and permeability of 2.5 and 1, respectively and with a thickness of 24 mm (corresponding to a 300 kV insulation). The third layer is assumed to be a metallic shield with a resistivity of 18.6 n$\Omega\times$m. The last layer is assumed to be an insulating cover, with relative permittivity and permeability of 2.3 and 1, respectively. Other assumed distances and thicknesses are as depicted in Figure 4.4 (left).

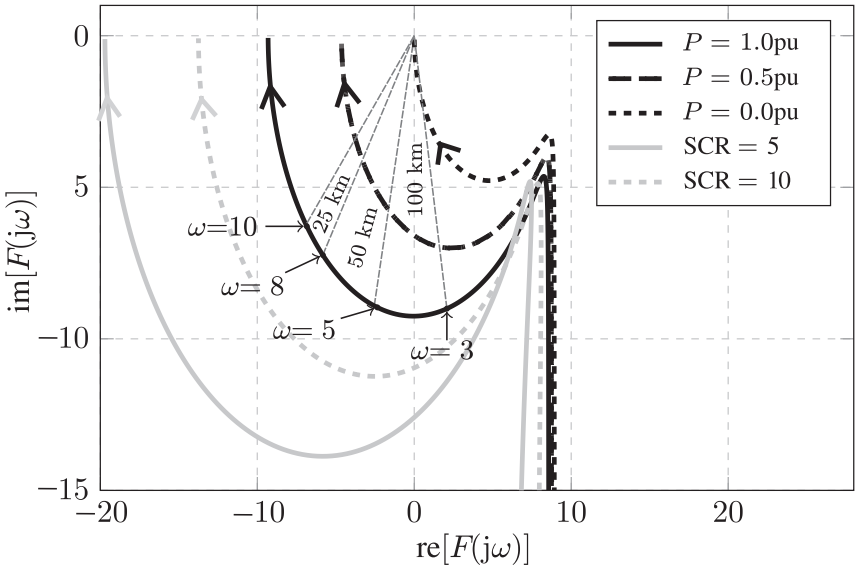

Figure 4.2: Nyquist plots of F for $P_1 = 0$, $+0.5$ pu and $+1$ pu. Gray curves show F for SCRs of 5 and 10 and for $P = +1$ pu.

The geometric configuration of the studied OHL (shown in Figure 4.4(right)) is based also on typical distances of ac system OHL of comparable voltage ratings such as in [51]. The assumed ground wire, G, has a dc resistance of 2.86 Ω/km, a radius of 5.5 mm and sag of 5 m. Conductors C1 and C2 have are assumed to be of Chukar type with dc resistance of 0.0326 Ω/km, a radius of 16.3 mm, and a sag of 10 m. Moreover, C1 and C2 are assumed to be composed of two bundled conductors separated by 0.6 m. For the sake of comparison, lumped parameters at 50 Hz for both, the cable and the OHL, are summarized in Table 4.1. From the table, the main observation is that the OHL inductance is considerably higher than the dc-cable one. Since the VSC capacitors are included in the model, lower RFs are expected for OHL.

Table 4.1: Cable and OHL lumped parameters

Parameter per length	**Value (dc-cable)**	**Value (OHL)**
Pole-to-earth capacitance	0.21 μF/km	4.59 nF/km
Pole-to-pole capacitance	0	0.86 nF/km
Self inductance	0.19 mH/km	1.82 mH/km
Mutual inductance	neglected	0.90 mH/km
Resistance	0.038 Ω/km	0.087 Ω/km

4.3.1 Comparison of transmission line models

In previous works [18, 30, 52], system stability has been studied considering Π-section models for dc-cables. However, line parameters, such as resistances and inductances, are frequency dependent. Thus, it is important to carry out a comparison of the resonance characteristics between lumped and distributed-parameter models of TLs. Impedance frequency scan is performed at the point where VSC_1 is connected, as depicted in Figure

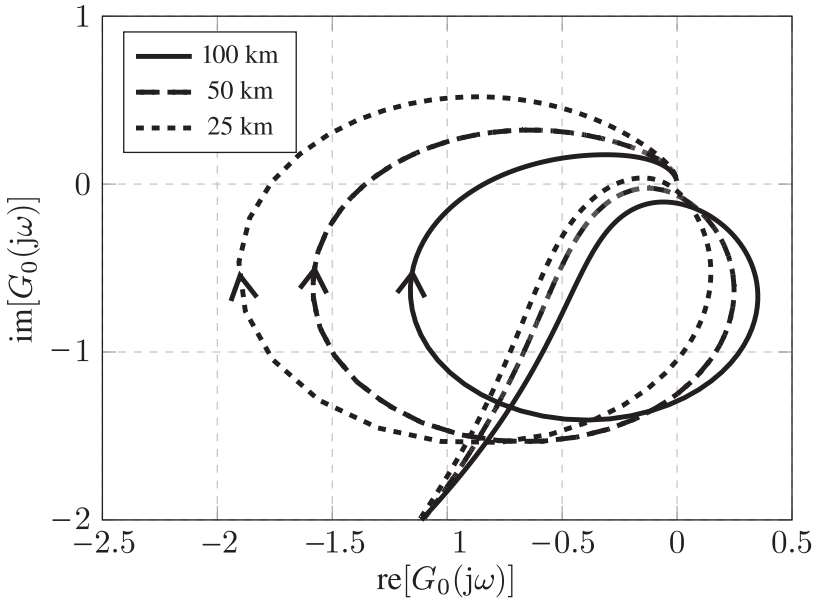

Figure 4.3: Nyquist plots of FG_0 for $P_1 = +1$ pu.

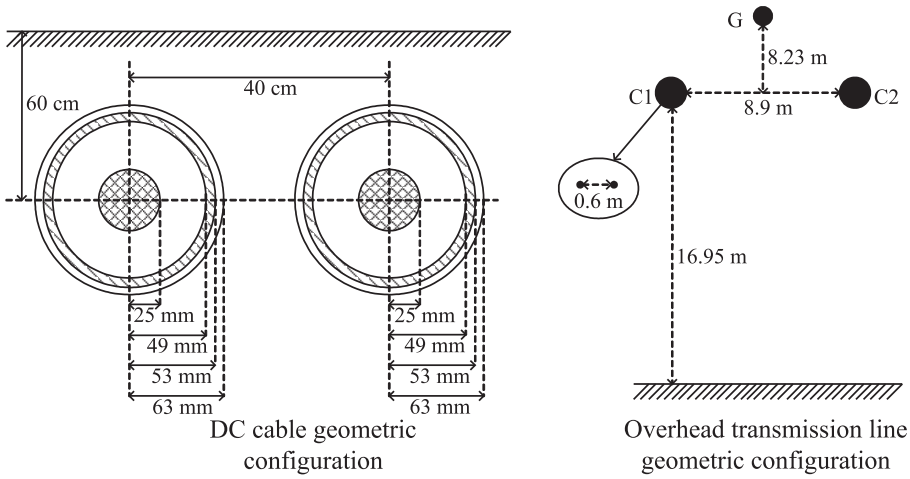

Figure 4.4: Geometric configuration of a dc cable (left) and OHL (right).

4.5. Note that, as shown in the figure, VSC capacitors are included in the measurements. Measurements are performed for line lengths of 25, 50, 75 and 100 km. Three TL models are tested: a distributed-parameter model (frequency dependent -phase- model as described in [53]), a one Π-section model, two Π-section model. The two Π-section model is considered in order to check the impact of adding more resonant components into the model. It should be mentioned that more resonances appear in a cable (or OHL) when considering more accurate models, but only the resonance with the highest dc-side RP is considered in the upcoming figures.

Results concerning the comparison of the dc-cable models are shown in Figure 4.6. It can be seen that the dc-side RF of the distributed parameter model is higher compared to the Π-section models. This means that the resonance of both type of models will coincide with different values of the dc-side PDC so different reactions from the HVDC system are also expected. Another observation is that the dc-side RP of the distributed parameter model is considerably lower than the one of the Π-section models. This means that the risk of

instability is much lower when distributed parameter models are considered in the analysis.

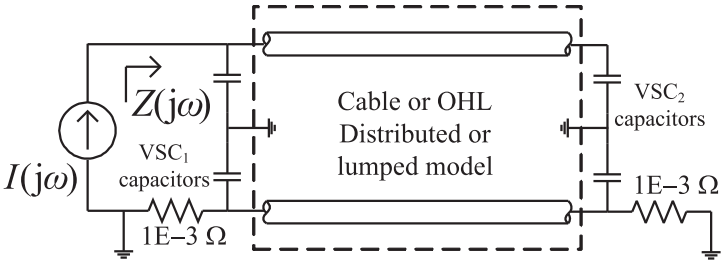

Figure 4.5: Setup for impedance frequency scan

Regarding the OHL, it can be seen from Figure 4.6 that the dc-side RF of the compared models are very close among each other. On the other hand, similarly to the cable, the dc-side RP of the OHL distributed parameter model is considerably lower than the Π-section models. Another aspect to highlight is that the dc-side RF of OHL is lower compared to the cable one and that the dc-side RP is considerable higher. While it is true that for low frequencies re$[F(\mathrm{j}\omega)]$ is less negative and even positive in most of the cases, the considerable size of the dc-side RP still increases the risk of instability, especially if VSCs connected to weaker ac systems, control system delays and ac side capacitors are considered.

From this analysis, we can conclude that the use of Π-section models for stability studies leads to pessimistic scenarios compared to distributed parameter models. This is because the dc-side RP considerably lower when considering the frequency dependency of the TL parameters. This means that, if a certain stability limit is found in studies that consider Π-section models, it is very likely that this limit is much higher when considering distributed-parameter models. Thus, the use of distribute parameter is recommended in order to obtain more realistic results. Furthermore, the results show that the dc-side RPs of the OHLs are considerably higher than the dc-cable ones, which means that OHLs can impose a greater instability risk compared to dc cables.

4.3.2 Combination of dc-cable and OHL

In this case, the resonance characteristic is studied for a dc-transmission link composed by a combination of a dc-cable and an OHL which are implemented as distributed parameter models. The full length of the dc-transmission link is assumed to be 100 km. The composition cable−OHL is varied such that the OHL section is 0%, 25%, 50%, 75% and 100% of the total length. Two cases are studied: 1) Impedance measurement when the dc-cable section is right in front of the VSC_1. 2) Impedance measurement when the OHL section is in front of VSC_1. Results from both cases are plotted in Figure 4.7 for the sake of comparison. It can be seen from the figure that the dc-side RF is the same regardless of the relative position between the cable and OHL. However, the figure also shows that the dc-side RP is higher when the OHL-section is closer to VSC_1 increasing the risk of instability in this case. From the figure, a 10 km OHL section installed in front of VSC_1 results in a dc-side RF of approximately 5 pu and a dc-side RP of 0.25 pu, which, according to Figure 3.5, lies

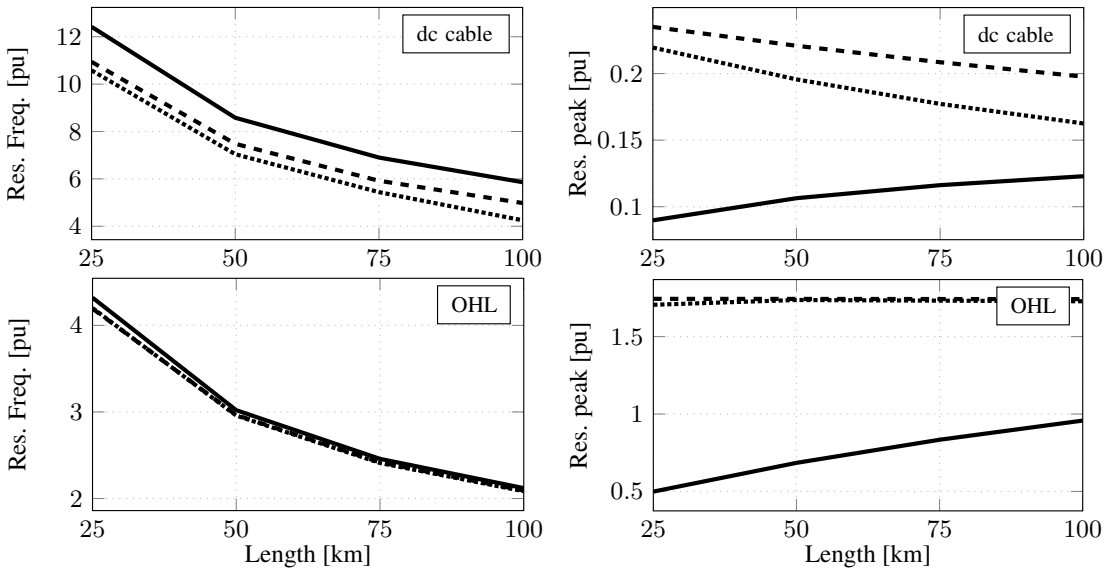

Figure 4.6: DC cable (upper) and OHL (bottom) RF (left) and RP (right). Comparison between between a distributed parameter (solid), one Π-section (dotted) and two Π-section (dashed) models.

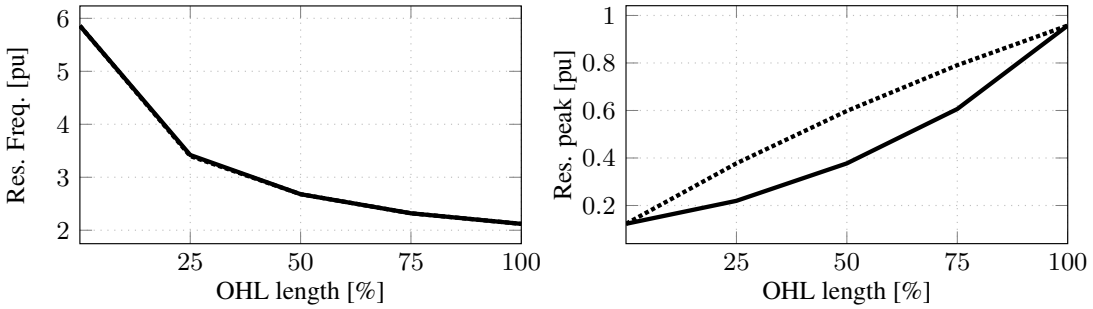

Figure 4.7: RF (left) and RP (right) for a 100 km transmission link composed of an OHL in series with a dc-cable. Case 1 (solid), dc-cable close to VSC_1. Case 2 (dotted), OHL close to VSC_1.

within a risky region in re$[F(\text{j}\omega)]$.

4.3.3 Impact of dc-side filter

The filter setup assumed in this section is based on the one described in [37]. As shown in Figure 4.8, the filter is composed of a smoothing reactor (with a resistance of 0.1 Ω and inductance of 5 mH), a third-harmonic filter (tuned to 150 Hz, quality factor of 5, and 20 MVAr at 50 Hz), and a high frequency filter (tuned to 1950 Hz, quality factor of 5, and 20 MVAr at 50 Hz). Impedances are measured for different lengths of a dc cable and OHL (separately) with dc-side filters connected at both ends. The results are summarized in Figure 4.9 and they can be compared to Figure 4.6, where the resonance characteristics of the cable and OHL without filters are presented. By comparing the two figures, it can be seen that, for the dc-cable case, the impact of the considered dc filter is to decrease the dc-side RF while increasing the dc-side RP. Regarding the OHL case, the impact of the dc filter on the dc-side RF is negligible; however, it increases the dc-side RP. Therefore, in both cases, introducing dc filters increases the dc-side RP, which represents an increase on

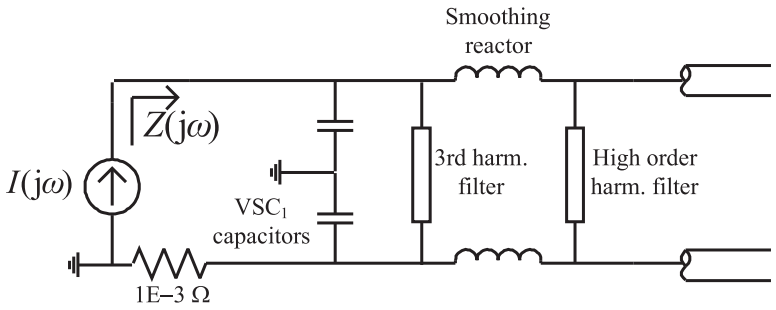

Figure 4.8: Impedance frequency scan including DC-filters.

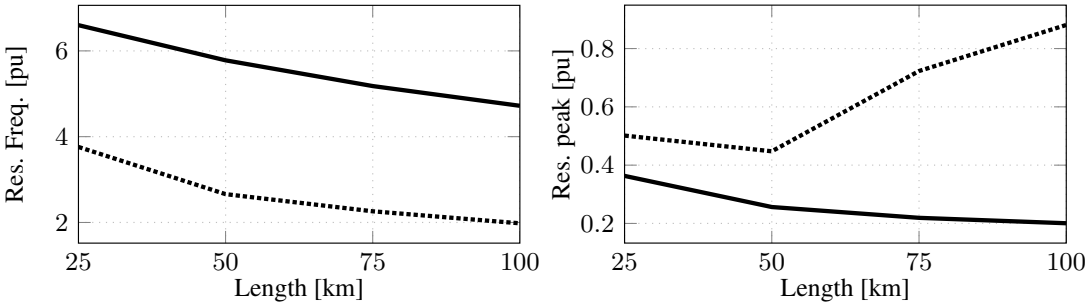

Figure 4.9: RF (left) and RP (right) for a dc cable (solid) and an OHL (dotted) of different lengths, considering a dc-side filter.

the instability risk.

4.4 Mitigation measures and simulations

The analysis performed so far shows that instability is determined by the amount of power transfer, the controller design, the ac system characteristics and the dc-network resonance characteristics. Then, actions to take in order to avoid instability are

1. Limit the size of $|F(j\omega)|$ around the RF such that (4.4) is fultilled. This can be achieved by decreasing the DVC gains and also by adding LPF or notch filters to pre-process the voltage e_i. However, decreasing the size of $|F(j\omega)|$ might lead to undesired dynamic performance for large signal disturbances;

2. Limit the amount of power transfer. When instability takes place, one "online" solution can be to decrease the power injected by the DVC-VSC;

3. Decrease the dc-side RP, Z_{peak}. This can be achieved by installing a physical filter tuned to the RF at the dc bus to which the VSC is connected. However, this solution implies an extra cost and losses to the system. Moreover, the filter can be ineffective if upgrades in the dc-link changes the resonance characteristics.

Now, the usefulness of the stability condition (4.4) is demonstrated in this section through time-domain simulations. The system under study is depicted in Figure 4.10. The VSCs are assumed to be connected to weak ac grids with SCRs of 3 and no ac-side capacitors.

DC-side filters are the same as the ones studied in Section 4.3. The dc-transmission link is composed by 10 km of OHL and 90 km of dc-cable both modeled as distributed parameter with the geometric configurations shown in Figure 4.4. Moreover, VSCs are modeled as two-level converters with switching models. VCC and PLL gains are set as specified in Table 2.4. Furthermore, in this case, DVC gains k_{pe} and k_{ie} are decreased to less aggressive values: $k_{\mathrm{pe}} = 2.31$ pu and $k_{\mathrm{ie}} = 0.31$ pu.

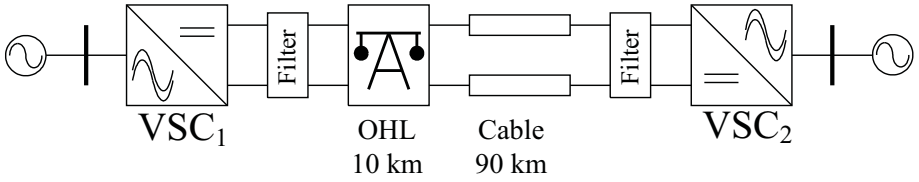

Figure 4.10: VSC-HVDC system under study in Section 4.4.

Power is increased from VSC_1 to VSC_2 at a rate of 0.5 pu/s. VSC_1 dc-bus voltage and power are shown in Figure 4.11. It can be seen that instability occurs when reaching 1 pu power. Voltage e_1 is zoomed in Figure 4.12 and it can be seen that the RF is around 210 Hz (4.2 pu). Moreover, the resonance characteristic of the transmission link is plotted on Figure 4.13 and it can be seen that the dominant RF is 3.88 pu, which is in the order of the frequency shown in Figure 4.12. According to the criterion stated in (4.4), $|F(\mathrm{j}\omega)|$ should

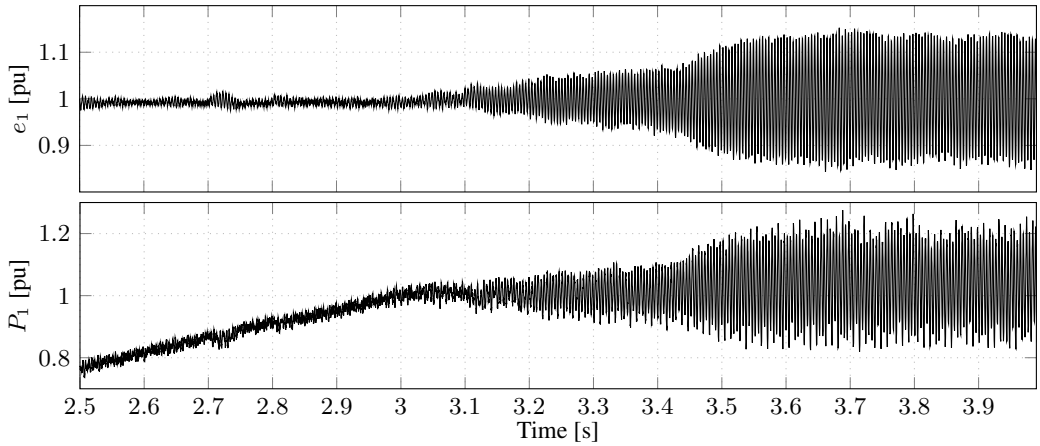

Figure 4.11: Simulation of a power increase from VSC_1 to VSC_2 in the system from Figure 4.10. VSC_1 voltage and power.

be less than $1/\mathrm{Z}_{\mathrm{peak}} = 3.47$ pu. F is obtained for weak ac grids according to (3.19) and its magnitude and real part are shown in Figure 4.13. The figure shows that around the RF, $|F(\mathrm{j}\omega)|$ is 4.38 pu, which is greater than $1/\mathrm{Z}_{\mathrm{peak}}$. One solution to the instability is sketched in Figure 4.14 where a notch filter with the transfer function

$$H_{\mathrm{n}}(s) = \frac{s^2 + 2\epsilon_1\omega_{\mathrm{f}}s + \omega_{\mathrm{f}}^2}{s^2 + 2\epsilon_2\omega_{\mathrm{f}}s + \omega_{\mathrm{f}}^2} \tag{4.6}$$

is added so that voltage e_1 is filtered at the RF. Since the reference e_1^{ref} is constant, the transfer function of the VSC subsystem is in the end

$$F'(s) = F(s)H_{\mathrm{n}}(s). \tag{4.7}$$

The RF is about 4 pu, so, the notch filter is tuned to a frequency of 4 pu. At a frequency of 4 pu the following should be fulfilled

$$4.38H_{\mathrm{n}}(\mathrm{j}4) < 3.47 \tag{4.8}$$

meaning that $\epsilon_1/\epsilon_2 < 0.8$. Then, ϵ_1 and ϵ_2 can be set as 0.1 and 0.13 respectively. The magnitudes of F and F' are also shown in Figure 4.13 and it can be seen that, around 4 pu the magnitude of $F'(\mathrm{j}\omega)$ decreases to 3.42, which is slightly below 3.47 pu, fulfilling (4.4). Figure 4.13 also shows that the magnitude of $F'(\mathrm{j}\omega)$, with $\epsilon_1 = 0.1$ and $\epsilon_2 = 0.3$, decreases further the depth of the notch. While in this case a much smaller $|F'(\mathrm{j}\omega)|$ is obtained, the real parts of F and F', plotted in Figure 4.13, show that re$[F'(\mathrm{j}\omega)]$ decreases considerably at lower frequencies, increasing the risk of instability at these frequencies. Then, the parameters of the notch filter are selected as $\omega_{\mathrm{f}} = 4$ pu, $\epsilon_1 = 0.1$ and $\epsilon_2 = 0.13$.

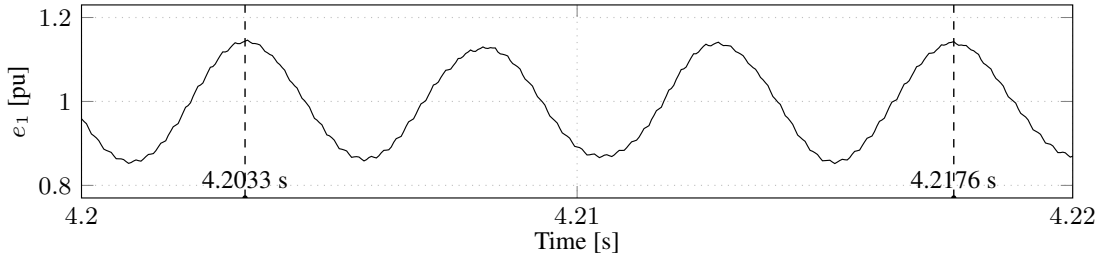

Figure 4.12: Detailed e_1 from Figure 4.11.The oscillation period is 4.7 ms (RF of 210 Hz or 4.2 pu).

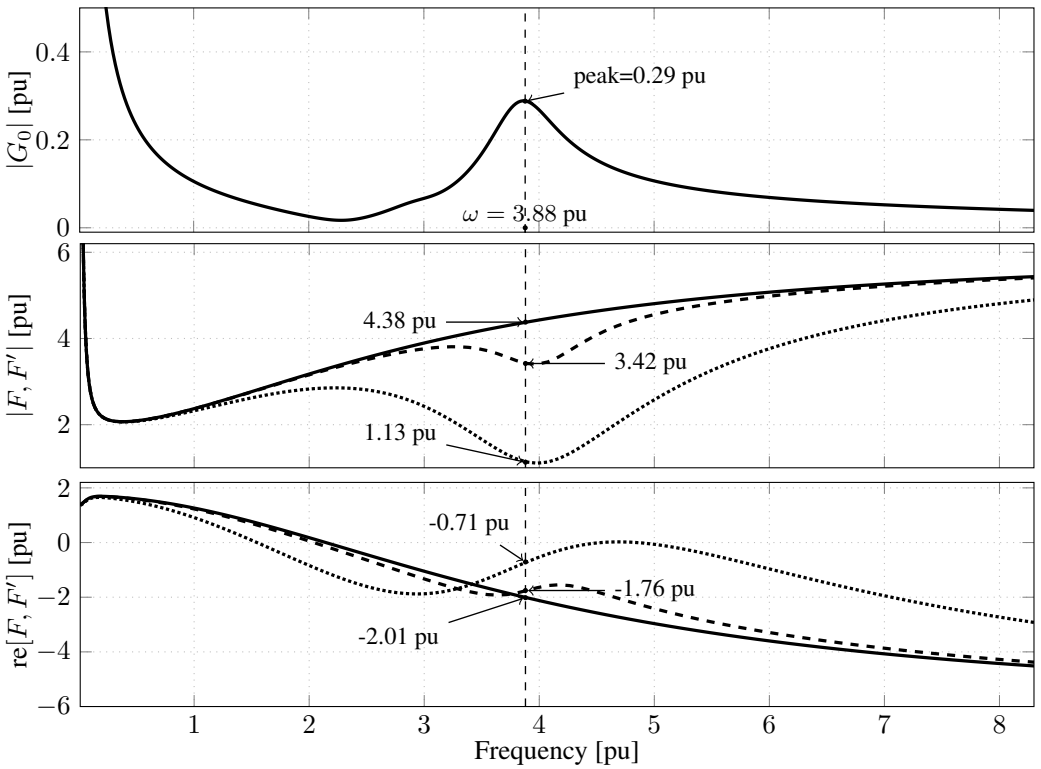

Figure 4.13: Magnitude of $G_0(\mathrm{j}\omega)$ (upper). Magnitude (middle) and real part (bottom) of $F(\mathrm{j}\omega)$ (solid), $F'(\mathrm{j}\omega)$ with $\epsilon_1 = 0.1$ and $\epsilon_2 = 0.13$ (dotted), and $F'(\mathrm{j}\omega)$ with $\epsilon_1 = 0.1$ and $\epsilon_2 = 0.3$ (dotted).

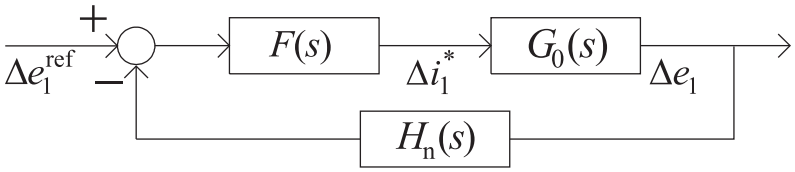

Figure 4.14: Equivalent VSC-HVDC system including a notch filter $H(s)$.

The simulation is repeated with the notch filter implemented and the results are shown in Figure 4.15. As predicted in the analysis, it can be seen that the system becomes stable with the notch filter implemented.

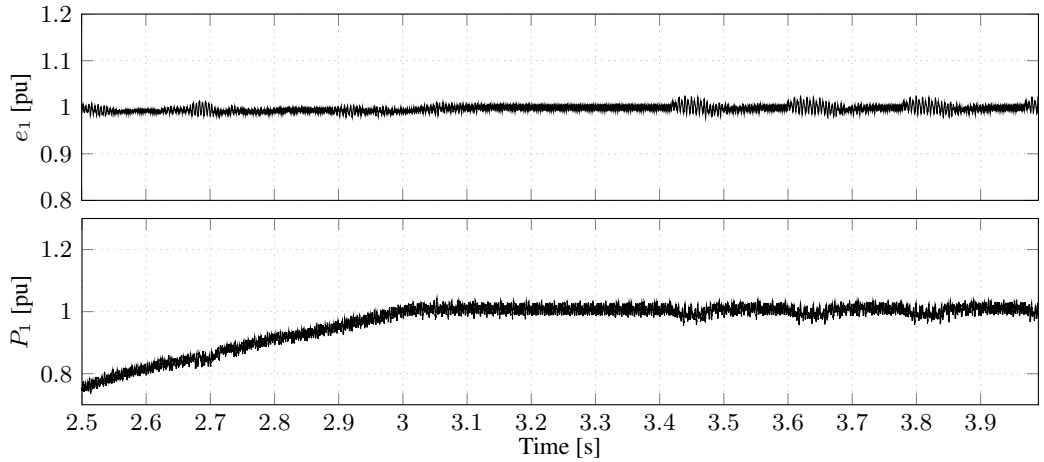

Figure 4.15: Simulation of a power increase from VSC_1 to VSC_2 in the system from Figure 4.10 with the notch filter implemented in VSC_1. VSC_1 voltage and power.

4.5 Conclusion

The analysis performed in this chapter has shown that it is not only negative dc-side PDC that causes instability but also high RPs. Therefore, the impact of different topologies on the dc-network resonance characteristic has been investigated in this chapter. The following has been found:

1. Assuming lumped parameters models for the TL led to pessimistic results. This is due to the fact that lumped models tend to overestimate the dc-side RP of the TL;

2. Including OHL in the dc-network configuration leads to a dc-side RP increase. This means a greater risk for the system stability, even if these dc-side RPs occur at lower dc-side RFs;

3. Including dc-side filters in the dc-network also leads to a dc-side RP increase.

Finally, a conservative stability condition has been presented. This condition provides a measure of the maximum size od the dc-side PDA. The following is suggested to improve stability:

1. Decrease the magnitude of the dc-side PDA to less than the inverse of the dc-side RP, if the dc-side PDC is negative at a certain RF. This can be achieved through pre-processing the dc-bus voltage feedback through a notch filter or a low pass filter. Another option is to decrease the gains of the DVC. However, these measures can turn the DVC-VSC slow to large signal disturbances.

2. Limit to amount of power transfer. This can be an online solution if a dc-network resonance related instability is triggered inadvertently.

3. Decrease the dc-side RP by introducing physical filters at the VSC's dc side. However, this introduces an extra cost to the system and can be ineffective if the dc-network configuration changes.

Chapter 5

Stability analysis in MTDC systems: Theoretical background

In the previous chapters, conditions where instabilities originated from dc-network resonances take place have been investigated in a point-to-point HVDC system. It can be argued, however, that these instabilities are not so critical in these kind of systems due to the fact that the dc-network configuration is rather fixed. So, once a problem is identified and solved, it is less likely that it takes place again. This is not the case in more complex systems such as MTDC, where the dc-network configuration is more variable. Understanding the causes of instability is more relevant in MTDC systems since, for example, taking out of service any cable or OHL from the dc-network change its resonance characteristic. In this regard, a method to study instabilities originated from dc-network resonances in MTDC systems is presented in this chapter. Similarly to the method presented for a point-to-point HVDC system, the method consists of dividing the MTDC system into subsystems. One of the systems is the dc-network, which is composed by cables and OHLs, and the other subsystems are each VSC connected to the dc-network. With the subsystems as defined in this chapter, it is clearly shown what the contribution of each VSC to instability is and the way they interact in resonance cases. This chapter is based on Paper VIII.

5.1 Multivariable representation of MTDC systems

A sketch of an MTDC system is shown in Figure 5.1, where "n" converters, VSC_1, VSC_2, ..., VSC_n are interconnected through a dc network. In this system, some VSCs are set as DVC-VSCs, while the remaining VSCs are set PC-VSCs. The controlled system is the dc network, whose inputs are the currents injected by the VSCs, $\mathbf{i} = [i_1 \ i_2 \dots i_\text{n}]^\text{T}$ and outputs are the voltages $\mathbf{e} = [e_1 \ e_2 \dots e_\text{n}]^\text{T}$, as shown in Figure 5.1. Therefore, the dc network can be modeled as

$$\mathbf{e}(s) = \mathbf{Z}(s)\mathbf{i}(s) \tag{5.1}$$

where $\mathbf{Z}(s)$ is the dc-network transfer matrix with elements $\{z_{ij}(s)\}$. Note that $\mathbf{Z}(s)$ is, in practice, the dc-network impedance matrix. Considering (2.5), the current injected by the

i-th VSC can be linearized as

$$\Delta i_i = \Delta i_i^* - G_{i0}\Delta e_i, \tag{5.2}$$

with $\Delta i_i^* = \Delta P_i / e_{i0}$ and $G_{i0} = P_{i0}/e_{i0}^2$.

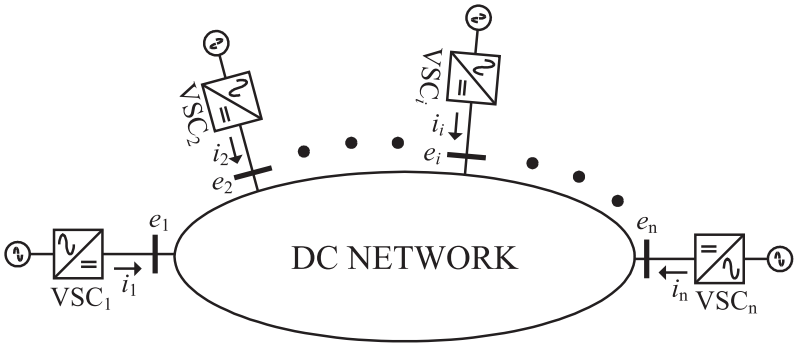

Figure 5.1: Sketch of a multi-terminal HVDC system.

Assume also that the VSCs are driven by the controllers described in Section 2.1.2. Thus, the controller inputs of a DVC-VSC are e_i^{ref} and $i_{\text{f}i}^{q\text{ref}}$, while the controller inputs of a PC-VSC are $i_{\text{f}i}^{d\text{ref}}$ and $i_{\text{f}i}^{q\text{ref}}$. If all references $i_{\text{f}i}^{q\text{ref}}$ are assumed constant, the currents injected by VSC$_i$ to the dc network can be expressed as

$$\Delta i_i = -G_{i0}\Delta e_i + F_{\text{p}i}(s)\Delta P_i^{\text{ref}} \tag{5.3}$$

for PC-VSCs and

$$\Delta i_i = -(G_{i0} + F_{\text{e}i})\Delta e_i + F_{\text{e}i}\Delta e_i^{\text{ref}} \tag{5.4}$$

for DVC-VSCs. $F_{\text{p}i}$ is the transfer function from ΔP_i^{ref} to Δi_i^* and $F_{\text{e}i}$ is the transfer function from Δe_i^{ref} to Δi_i^*.[1] Then, the MTDC system can be represented as the Multiple-Input Multiple-Output (MIMO) system depicted in Figure 5.2. Using (5.1) (expressed in small signal terms) (5.3) and (5.4), the close-loop transfer matrix of the system is

$$\Delta \mathbf{e} = [\mathbf{I} + \mathbf{Z}\mathbf{Y}]^{-1}\mathbf{F}_{\text{r}}\Delta \mathbf{r} \tag{5.5}$$

where the Laplace variable "s" has been dropped for the ease of notation. $\mathbf{Y}$ is a diagonal matrix whose diagonal elements are

$$y_i = \begin{cases} G_{i0} + F_{\text{e}i} & \text{if VSC}_i \text{ is a DVC-VSC} \\ G_{i0} & \text{if VSC}_i \text{ is a PC-VSC} \end{cases} \tag{5.6}$$

Likewise, $\mathbf{F}_{\text{r}}$ is a diagonal matrix with diagonal elements

$$F_{\text{r}i} = \begin{cases} F_{\text{e}i} & \text{if VSC}_i \text{ is a DVC-VSC} \\ F_{\text{p}i} & \text{if VSC}_i \text{ is a PC-VSC} \end{cases} \tag{5.7}$$

[1] Observe that $F_{\text{e}i}$ is the same as the transfer function F defined in the previous chapters.

System (5.5) is stable if $\mathbf{F}_{\mathrm{r}}$ is stable (i.e. each $F_{\mathrm{p}i}$ and $F_{\mathrm{e}j}$ are stable) and if the zeros of

$$\mathcal{S} = \det(\mathbf{I} + \mathbf{ZY}) \tag{5.8}$$

are in the LHP. Expression (5.8) indicates that the dc-network dynamics is determined by the dc-network characteristics ($\mathbf{Z}$), the loading of the system (G_{i0}), and the dynamic characteristics of the DVC-VSCs ($F_{\mathrm{e}i}$). In addition, PC-VSCs ($F_{\mathrm{p}i}$) are not contained in (5.8), hence, they have no impact on the dc-network stability. This agrees with the claim made in Section 2.3.1 and also in [36, 54], which states that PC-VSCs have no impact on dc-network resonance related dynamics.

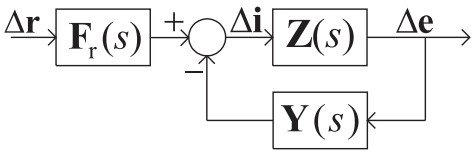

Figure 5.2: MIMO representation of a MTDC system.

5.2 Stability analysis of MTDC systems

According to Nyquist stability criterion, the number of RHP poles of (5.5), i.e. unstable poles, is equal the number of clockwise encirclements of $\mathcal{S}$ around the origin [55], if both $\mathbf{Z}$ and $\mathbf{Y}$ are stable. This is true in this case since $\mathbf{Z}$ is the dc-network impedance matrix, then stable,[1] Matrix $\mathbf{Y}$ is stable since G_{i0} is constant, and $F_{\mathrm{e}i}$, if properly designed, is stable. Then, according to [56], $\det(\mathbf{I} + \mathbf{ZY})$ can be written as

$$\det(\mathbf{I} + \mathbf{ZY}) = \det(\mathbf{I}) + \det(\mathbf{ZY}) + \sum_{i=1}^{\mathrm{n}-1} \Gamma_n^i(\mathbf{ZY}/\mathbf{I}^i) \tag{5.9}$$

where $\Gamma_n^i(\mathbf{ZY}/\mathbf{I}^i)$ is defined as the sum of determinants, where in each matrix the i rows of $[\mathbf{ZY}]$ are substituted by the corresponding rows of $\mathbf{I}$. For example, for a 3 terminal system, (5.8) becomes

$$\mathcal{S} = \det(\mathbf{I}) + \Gamma_3^2(\mathbf{ZY}/\mathbf{I}^2) + \Gamma_3^1(\mathbf{ZY}/\mathbf{I}^1) + \det(\mathbf{Z})\det(\mathbf{Y}).$$

According to the definition stated above

$$\Gamma_3^2(\mathbf{ZY}/\mathbf{I}^2) = \det\begin{bmatrix} 1 & 0 & 0 \\ 0 & 1 & 0 \\ z_{31}y_1 & z_{32}y_2 & z_{33}y_3 \end{bmatrix} + \det\begin{bmatrix} z_{11}y_1 & z_{12}y_2 & z_{13}y_3 \\ 0 & 1 & 0 \\ 0 & 0 & 1 \end{bmatrix} + \det\begin{bmatrix} 1 & 0 & 0 \\ z_{21}y_1 & z_{22}y_2 & z_{23}y_3 \\ 0 & 0 & 1 \end{bmatrix} \tag{5.10}$$

$$\Gamma_3^1(\mathbf{ZY}/\mathbf{I}^1) = \det\begin{bmatrix} 1 & 0 & 0 \\ z_{21}y_1 & z_{22}y_2 & z_{23}y_3 \\ z_{31}y_1 & z_{32}y_2 & z_{33}y_3 \end{bmatrix} + \det\begin{bmatrix} z_{11}y_1 & z_{12}y_2 & z_{13}y_3 \\ 0 & 1 & 0 \\ z_{31}y_1 & z_{32}y_2 & z_{33}y_3 \end{bmatrix} + \det\begin{bmatrix} z_{11}y_1 & z_{12}y_2 & z_{13}y_3 \\ z_{21}y_1 & z_{22}y_2 & z_{23}y_3 \\ 0 & 0 & 1 \end{bmatrix} \tag{5.11}$$

[1] Except for a pole in the origin coming from shunt capacitances; in such a case, the Nyquist path is indented around the origin to avoid including this pole into the RHP area.

from where

$$\Gamma_3^2(\mathbf{ZY}/\mathbf{I}^2) = z_{11}y_1 + z_{22}y_2 + z_{33}y_3 \tag{5.12}$$
$$\Gamma_3^1(\mathbf{ZY}/\mathbf{I}^1) = \gamma_{12}y_1y_2 + \gamma_{13}y_1y_3 + \gamma_{23}y_2y_3 \tag{5.13}$$
$$\text{with} \quad \gamma_{ij} = \det\begin{bmatrix} z_{ii} & z_{ij} \\ z_{ji} & z_{jj} \end{bmatrix} \quad \text{for } i \neq j$$

In a similar fashion, since a four terminal HVDC system is studied later, it can be shown that $\mathcal{S}$ in that case is

$$\begin{aligned}\mathcal{S} = 1 &+ z_{11}y_1 + z_{22}y_2 + z_{33}y_3 + z_{44}y_4 + \\ &\gamma_{12}y_1y_2 + \gamma_{13}y_1y_3 + \gamma_{14}y_1y_4 + \gamma_{23}y_2y_3 + \gamma_{24}y_2y_4 + \gamma_{34}y_3y_4 + \\ &\gamma_{123}y_1y_2y_3 + \gamma_{124}y_1y_2y_4 + \gamma_{134}y_1y_3y_4 + \gamma_{234}y_2y_3y_4 + \\ &\det(\mathbf{Z})y_1y_2y_3y_4\end{aligned} \tag{5.14}$$

$$\text{with} \quad \gamma_{ijk} = \det\begin{bmatrix} z_{ii} & z_{ij} & z_{ik} \\ z_{ji} & z_{jj} & z_{jk} \\ z_{ki} & z_{kj} & z_{kk} \end{bmatrix} \quad \text{for } i < j < k$$

Using (5.9), and defining $\mathcal{T} = \mathcal{S} - 1$, in general

$$\mathcal{T} = \sum_{i=1}^{\mathrm{n}} z_{ii}y_i + \sum_{i=2}^{\mathrm{n-1}} \Gamma^{(i)}(\mathbf{ZY}) + \det(\mathbf{Z}) \prod_{i=1}^{\mathrm{n}} y_i \tag{5.15}$$

where, in this case, $\Gamma^{(i)}$ denotes the sum of the determinants of all possible $i \times i$ different submatrices along the diagonal of $[\mathbf{ZY}]$. For example, considering the above expressions for $[\mathbf{ZY}]$ of 4×4 size, $\Gamma^{(2)}(\mathbf{ZY}) = \gamma_{12}y_1y_2 + \gamma_{13}y_1y_3 + \gamma_{14}y_1y_4 + \gamma_{23}y_2y_3 + \gamma_{24}y_2y_4 + \gamma_{34}y_3y_4$, $\Gamma^{(3)}(\mathbf{ZY}) = \gamma_{123}y_1y_2y_3 + \gamma_{124}y_1y_2y_4 + \gamma_{134}y_1y_3y_4 + \gamma_{234}y_2y_3y_4$. In this thesis, all z_{ii}, γ_{ij}, γ_{ijk}, $\ldots$, $\det[\mathbf{Z}]$ are called $\mathbf{Z}$-terms. In the same fashion, all y_i are called $\mathbf{Y}$-terms. From now on, stability is assessed using $\mathcal{T}$. This means that, an MTDC system is stable if $\mathcal{T}$ does not clockwise encircle the point -1. The properties of the $\mathbf{Z}$-terms are investigated in a four-terminal HVDC system, which is described next.

5.3 Description of a four-terminal HVDC system

In this chapter, resonance-related instabilities in MTDC systems are studied in the radial four-terminal VSC-HVDC system shown in Figure 5.3. In this system, the five TLs are varied between cables or OHLs as indicated in Table 5.1. The geometrical configurations of the cable and OHL used in this study are as indicated previously in Figure 4.4. The power rating of each VSC is 600 MVA and the dc-network nominal voltage is $\pm$300 kV. Moreover, the electrical configuration and control system of each VSC are as considered in Sections 2.1.1 and 2.1.2. The VSCs electrical parameter are as specified in Table 2.3 and the controller parameters are as presented in Table 2.4. The ac system impedances are set as $R_{\mathrm{si}} = 0.025$ pu and $L_{\mathrm{si}} = 0.25$ pu for a SCR of 4, and $R_{\mathrm{si}} = 0.02$ pu and $L_{\mathrm{si}} = 0.2$ pu

for an SCR of 5. These two values of SCRs are chosen to demonstrate that, although the ac system is strong, still small variations in the ac system strength can have complete different impact on the dc-network stability (as will be shown in Section 5.6). A LPF is included in all VSCs with a closed-loop bandwidth of 4 pu. The DVC PI gains are set as 1.54 pu and 0.31 pu, respectively, such that the bandwidth of the closed-loop DVC is 0.4 pu and also an ac-side capacitor with a capacitance of 0.4 pu. The VSC controllers are implemented in discrete time with a sampling frequency of 4 kHz. As control strategy, it is assumed that only VSC_1 is in DVC mode, while the other VSC are in PC mode. For the analysis, (5.14) is used since it corresponds to a four-terminal HVDC system. Distributed-parameter TL models are used in order to obtain more realistic results. Then, a procedure to derive **Z**, and hence the **Z**-terms is presented next.

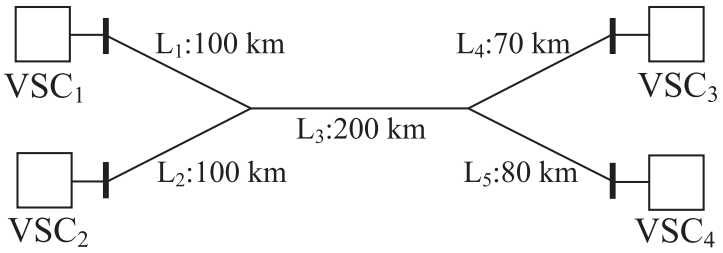

Figure 5.3: Four-terminal VSC-HVDC system studied in this chapter.

Table 5.1: DC network configurations

Cases	L1	L2	L3	L4	L5
Configuration 1	OHL	OHL	Cable	OHL	OHL
Configuration 2	Cable	Cable	OHL	Cable	Cable

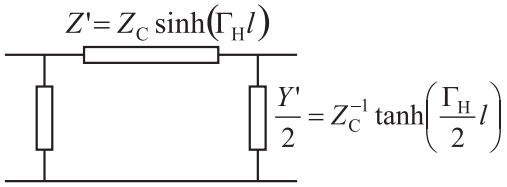

Figure 5.4: Lumped equivalent Π of a distributed-parameter TL model.

5.4 The impedance matrix, Z

The derivation of the dc-network impedance matrix, **Z**, is based on the possibility of representing a distributed-parameter TL model as a lumped-parameter Π equivalent (DPLE-Π) "insofar terminal characteristics are concerned [57]." The DPLE-Π model is shown in Figure 5.4, where Z_{C} is the TL characteristic impedance and Γ_{H} is the propagation function. In our case, both, Z_{C} and Γ_{H}, are frequency-dependent 2×2 matrices with complex elements. Hence Z' and $Y'/2$ are also 2×2 matrices and this represents the relationship between positive and negative poles. Since the positive and negative poles are symmetrical, the order of Z' and $Y'/2$ can be further decreased to 1×1. Z_{C} and Γ_{H} as functions of

frequency can be obtained using computational tools such as the line constants program of PSCAD$^{\mathrm{TM}}$. The dc-network admittance matrix is built from the DPLE-Π model derived for each TL, including the admittances of the VSC capacitors, $\mathrm{j}\omega C_{\mathrm{vsc}i}$. Finally, $\mathbf{Z}$ is found as the inverse of the admittance matrix for each frequency.

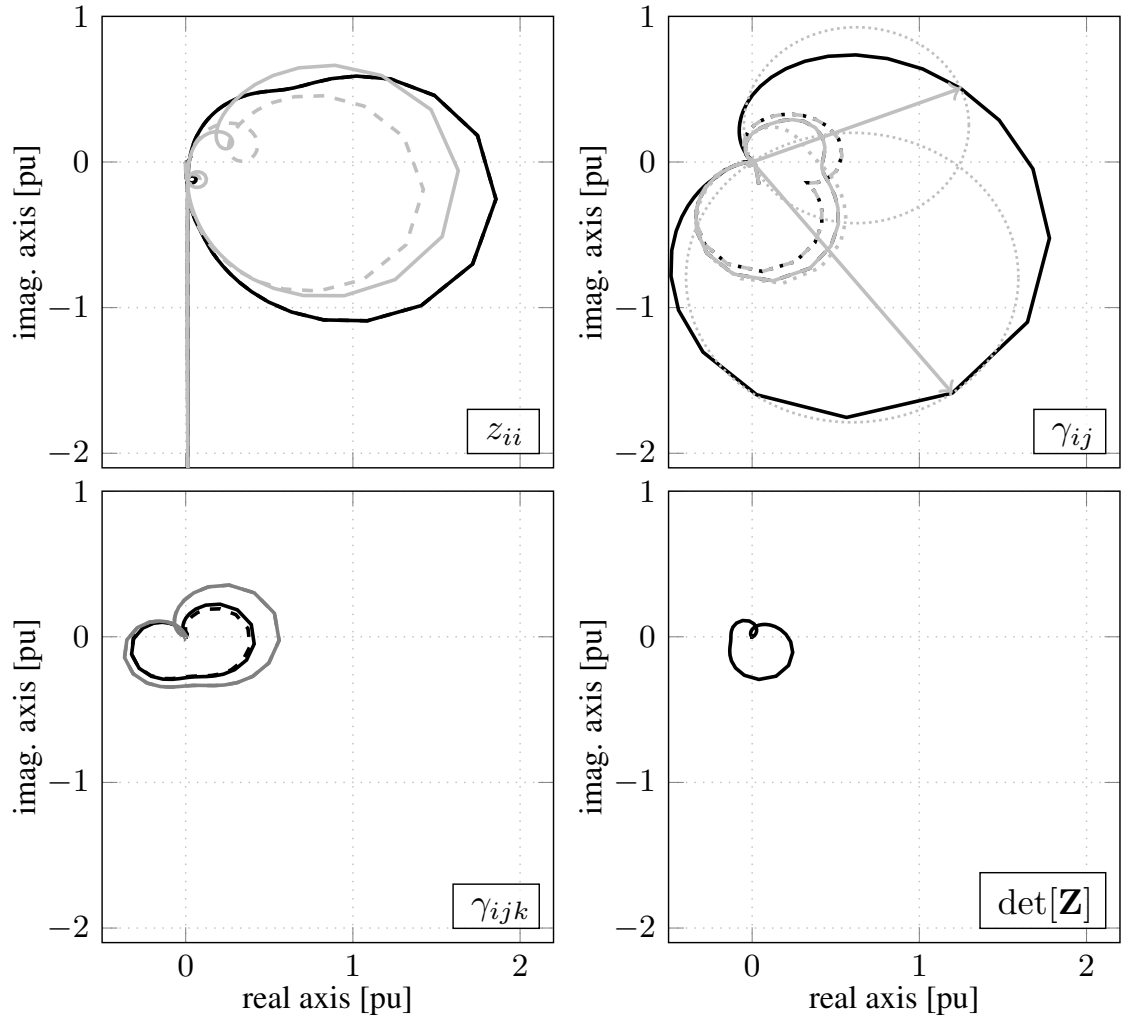

Figure 5.5: $\mathbf{Z}$-terms of the studied MTDC system. Curves are black solid: z_{11}, γ_{12}, γ_{123}, $\det[\mathbf{Z}]$; black dashed: z_{22}, γ_{13}, γ_{124}; black dotted: γ_{14}, gray solid: z_{33}, γ_{23}, γ_{134}; gray dashed: z_{44}, γ_{24}, γ_{234}; gray dotted: γ_{34}.

Nyquist plots of all $\mathbf{Z}$-terms for $\omega > 0$ are shown in Figure 5.5 for network configuration 1 (see Table 5.1). The figure shows for the z_{ii}-terms that, at low ω the curves are parallel to the imaginary axis and then, they describe an encirclement as ω approaches the RF.[1] For large ω, the curves converge to the origin. Note that there are several RFs, which can be seen in the z_{ii}-terms in Figure 5.5 in the form of small circles. In this particular case, the greatest encirclements described by $z_{11} = z_{22}$ takes place around the RF of $\omega_1^{\mathrm{r}} = 1.47$ pu, while the main encirclements of z_{33} and z_{44} occur at $\omega_2^{\mathrm{r}} = 1.71$ pu. Moreover, these encirclements are approximately oriented to the positive real axis. The other $\mathbf{Z}$-terms also

[1]This is very similar to the nyquist plot of G_0 shown in Figure 4.1. This is due to the fact that z_{ii} are actually the impedances seen from the dc-buses to where the VSCs are connected.

describe encirclements at the RFs stated above with different magnitudes and orientations. For instance, γ_{ij}-terms show two superimposed encirclements that take place at the RFs of ω_1^{r} and ω_2^{r}. Their orientation varies for ω_1^{r} and ω_2^{r}, and also their "diameters".

The Nyquist plots presented in this section show that the **Z**-terms can describe encirclement-like plots. Thus, the **Z**-terms can be defined as vectors, as explained in the next section.

5.5 Z-terms defined as encirclements

As argued in the previous section, the **Z**-term encirclements can be defined by their diameters (magnitudes), angle orientation, and frequencies. Therefore, in this thesis, the **Z**-terms are represented by vectors (for each RF), whose angle defines the encirclement orientation, whose magnitude represents the encirclement diameter. The superscript $(\cdot)^{\mathrm{cr}}$ is used[1] to denote these vectors. These vectors can be multiplied by complex numbers and added up, and the resultant is another vector with an associated encirclement. For example, let us consider the following two encirclements

$$z_{11}^{\mathrm{cr}} = z_{11}^{\mathrm{pk}} \angle \phi_{11} \text{ and } z_{22}^{\mathrm{cr}} = z_{22}^{\mathrm{pk}} \angle \phi_{22} \tag{5.16}$$

which, if considered as perfect circles, can be represented parametrically as

$$z_{11}^{\mathrm{cr}} = z_{11}^{\mathrm{pk}} e^{-\mathrm{j}\phi_{11}} \left(\frac{1 - e^{-\mathrm{j}\theta}}{2} \right) \tag{5.17a}$$

$$z_{22}^{\mathrm{cr}} = z_{22}^{\mathrm{pk}} e^{-\mathrm{j}\phi_{22}} \left(\frac{1 - e^{-\mathrm{j}\theta}}{2} \right) \tag{5.17b}$$

with $0 \leq \theta \leq 2\pi$. Now, let us consider the following vector sum, $a z_{11}^{\mathrm{cr}} + b z_{22}^{\mathrm{cr}}$, where a and b are arbitrary complex numbers. Expressed parametrically should lead to

$$a z_{11}^{\mathrm{cr}} + b z_{22}^{\mathrm{cr}} = \left(a z_{11}^{\mathrm{pk}} e^{-\mathrm{j}\phi_{11}} + b z_{22}^{\mathrm{pk}} e^{-\mathrm{j}\phi_{22}} \right) \left(\frac{1 - e^{-\mathrm{j}\theta}}{2} \right) \tag{5.18}$$

comparing (5.18) with (5.16) and (5.17), (5.18) can be expressed in vector form as

$$a z_{11}^{\mathrm{cr}} + b z_{22}^{\mathrm{cr}} = a z_{11}^{\mathrm{pk}} \angle \phi_{11} + b z_{22}^{\mathrm{pk}} \angle \phi_{22} \tag{5.19}$$

which shows that the resulting vector is also an encirclement, whose new magnitude is $|a z_{11}^{\mathrm{pk}} \angle \phi_{11} + b z_{22}^{\mathrm{pk}} \angle \phi_{22}|$ and new angle $\angle(a z_{11}^{\mathrm{pk}} \angle \phi_{11} + b z_{22}^{\mathrm{pk}} \angle \phi_{22})$. A graphical example is shown in Figure 5.6, where $\mathcal{T}^{\mathrm{cr}}$ is defined as

$$\mathcal{T}^{\mathrm{cr}} = a_1 z_{11}^{\mathrm{cr}} + a_2 z_{22}^{\mathrm{cr}} + a_0 \det(\mathbf{Z})^{\mathrm{cr}} \tag{5.20}$$

with z_{11}^{cr} and z_{22}^{cr} with an angle of 0^{o} and $\det(\mathbf{Z})$ with an angle of 90^{o}. Moreover, $a_1 = -0.5$, $a_2 = -0.5$ and $a_0 = 1$. In this example, the more negative a_1 and a_2, the more likely that $\mathcal{T}$ crosses the point -1 pu. Moreover, if a_0 has angle of -90^{o} it will also contribute

[1] Since there are several RFs, numbers are added to this superscript. For example $z_{11}^{\mathrm{cr}1}$, means that this encirclement corresponds to the first RF.

negatively to the system stability. In the general case described by (5.15), each $\mathbf{Z}$-term (e.g. z_{ii}, γ_{ij}, γ_{ijk}, etc) describes encirclements and their directions are changed by their associated $\mathbf{Y}$-terms (e.g. y_i, $y_i y_j$, $y_i y_j$, $y_i y_j y_k$, etc). Finally, the sum of all encirclements yields the resultant $\mathcal{T}$, which might enclose the point -1. Thus, the $\mathbf{Z}$-terms, defined as encirclements with angles and directions, provides useful information on how the VSC dynamics (respresented by the $\mathbf{Y}$-terms) influence in the system stability.

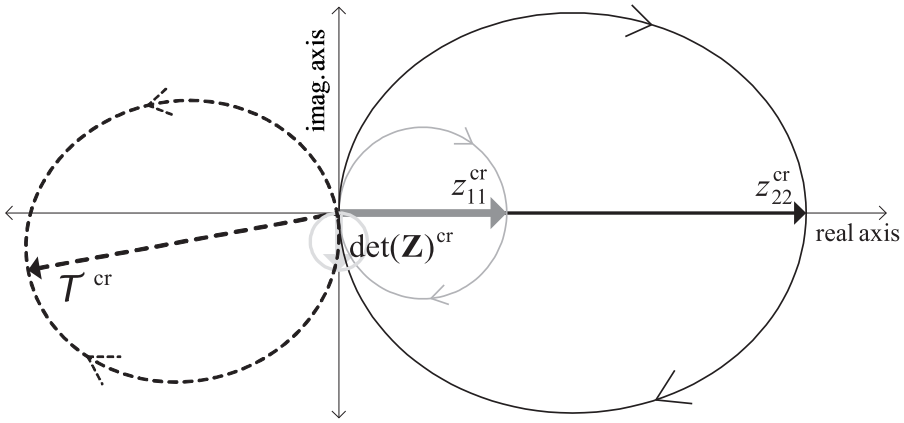

Figure 5.6: Vector representation z_{11}^{cir} (gray), z_{22}^{cir} (black) and $\det(\mathbf{Z})^{\text{cir}}$ (light gray). $\mathcal{T}$ (dashed) is for $a_1 = -0.5$, $a_2 = -0.5$ and $a_0 = 1$.

5.6 Frequency characteristics of y_i

Figure 5.7 shows the frequency response of y_1 for a DVC-VSC for different powers and SCRs and considering the electrical components and controller parameters stated earlier in this section. This is obtained following the procedure presented in Section 3.8, but considering now that $y_i = G_{i0} + F_{\text{e}i}$. In practice, y_i presents the similar characteristics of $F_{\text{e}i}$ (which is the VSC subsystem transfer function defined in Chapter 3), due to the fact that G_{i0} is constant and frequency independent. This means that, compared to $\text{re}[F_{\text{e}i}]$, $\text{re}[y_i]$ is slightly shifted upwards or downwards depending on the sign of G_{i0} (i.e. power direction) Through the study of F presented in Chapter 3, it can be inferred that for $P_{10} < 0$, $\text{re}[y_1] > 0$ for low frequency ranges, since usually $\text{re}[F_{\text{e}i}] > 0$ at low frequencies. Moreover, for $P_{10} \geq 0$, $\text{re}[y_1] < 0$ in some specific low frequency intervals. For instance, for SCR $= 5$ and $P_{10} = 1$ pu, $\text{re}[y_1] < 0$ for frequencies between $1.53 - 2.13$ pu, while for SCR $= 4$ and $P_{10} = 1$ pu, the frequency range is between $1.31 - 1.79$ pu. Then, according to Figure 5.7, with regards to the encirclement z_{11}, there is a risk of instability if $P_{10} = 1$ pu and SCR $= 4$ since $\text{re}[y_1] = -2$ pu for $\omega_1^{\text{r}} = 1.47$ pu. In the case of y_2, y_3 and y_4 (for PC-VSCs), their respective y_i-term is given by G_{i0}, which, assuming $e_{i0} \approx 1$, can be approximated as $G_{i0} = P_{i0}$. For example, with respect to z_{22}^{cr}, there is a risk of instability if $P_{20} = -1$ pu (i.e. $y_2 \approx -1$).

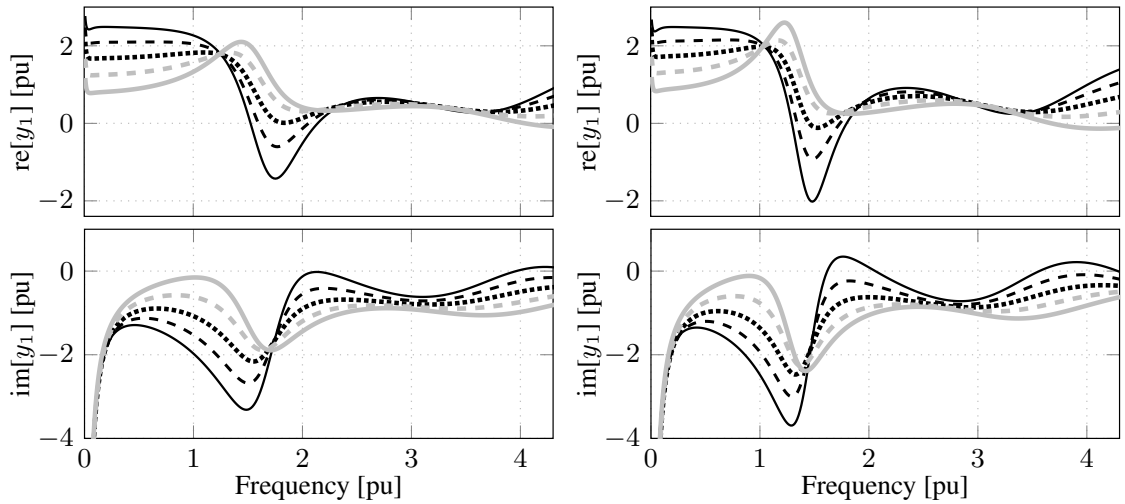

Figure 5.7: Real (upper) and imaginary (bottom) parts of $y_1 = G_{10} + F_{e1}$, with SCR $= 5$ (left) and SCR $= 4$ (right). Curves are given for $P_{10} = +1$ pu (gray solid), $P_{10} = +0.5$ pu (gray dashed), $P_{10} = 0$ pu (black dotted), $P_{10} = -0.5$ (black dashed) pu and $P_{10} = -1$ pu (black solid).

5.7 Resonance characteristics, configuration 1

For the dc-network configuration 1, the magnitudes and angles of the three most dominant resonances are shown in Table 5.2. Figure 5.5 shows that for, z_{11}, z_{22}, z_{33} and z_{44}, the values shown in Table 5.2 are good encirclement representations. The same is true for γ_{13}, γ_{14}, γ_{23}, γ_{24}, γ_{34}, also for all γ_{ijk} and $\det[\mathbf{Z}]$. However, γ_{12} is more complex to be represented as a circle, as the shape of the encirclements corresponding to the two different RFs are not clearly distinguishable as in the other γ_{ij}. In this case, γ_{12} can be represented with two circles, as shown in Figures 5.5, where one circle is represented by the vector $1.35\angle 22.2^{\text{o}}$ and the other by the vector $1.99\angle -53^{\text{o}}$. Table 5.2 shows that for the first RF, $\omega_1^{\text{r}} = 1.47$ pu, the most dominant encirclements are z_{11}^{cr1}, z_{22}^{cr1} and γ_{12}^{cr1}. If only the dominant **Z**-terms are considered, then, for the first RF, $\mathcal{T}$ can be approximated as

$$\mathcal{T}^{\text{cr1}} = z_{11}^{\text{cr1}}(y_1 + y_2) + \gamma_{12}^{\text{cr1}} y_1 y_2 \tag{5.21}$$

where it has been considered that $z_{11}^{\text{cr1}} = z_{22}^{\text{cr1}}$. For $\omega_2^{\text{r}} = 1.71$ pu, the most dominant encirclements are z_{11}^{cr2}, z_{22}^{cr2}, z_{33}^{cr2} and z_{44}^{cr2}, and all γ_{ij}^{cr2}, except γ_{12}^{cr2}. It can be seen that the γ_{ij}^{cr2}-terms have approximately the same magnitude and angle, so they can be approximated to the average value $\gamma_{\text{av}}^{\text{cr2}} = 0.8\angle$-82$^{\text{o}}$ for the sake of simplicity. Other **Z**-related terms can be neglected since they are small compared to z_{ii}^{cr2}, $\gamma_{\text{av}}^{\text{cr2}}$. In such a case, for the second RF, $\mathcal{T}$ can be approximated to

$$\begin{aligned}\mathcal{T}^{\text{cr2}} = z_{11}^{\text{cr2}}(y_1 + y_2) + z_{33}^{\text{cr2}} y_3 + z_{44}^{\text{cr2}} y_4 + \\ \gamma_{\text{av}}^{\text{cr2}}\left[(y_1 + y_2)(y_3 + y_4) + y_3 y_4\right]\end{aligned} \tag{5.22}$$

where it has been considered that $z_{11}^{\text{cr2}} = z_{22}^{\text{cr2}}$. Let us call $\mathcal{T}(z_{ii}^{\text{cr}}) = z_{ii}^{\text{cr}} y_i$, the resulting encirclement related to the z_{ii}-term, and $\mathcal{T}(\gamma_{ij}^{\text{cr}}) = \gamma_{ij}^{\text{cr}} y_i y_j$, and so on. Finally, for the RF of 3.22 pu, the **Z**-related terms are considerably smaller, hence, their impact is not considered.

Table 5.2: Encirclements mag. ($|\cdot|$ [pu]) and angles ($\angle\cdot$ [$^{\text{o}}$]) for configuration 1

freq. [pu]	1.47	1.71	3.22
$z_{11}^{\text{cr}} = z_{22}^{\text{cr}}$	1.87∠-8	0.52∠-78	0.15∠-73
z_{33}^{cr}	0.23∠36	1.63∠-2	0.19∠-63
z_{44}^{cr}	0.29∠5	1.43∠-8	0.17∠-69
γ_{12}^{cr}	1.99∠-53	0.23∠-155	0.02∠-152
$\gamma_{13}^{\text{cr}} = \gamma_{23}^{\text{cr}}$	0.45∠32	0.83∠-81	0.03∠-145
$\gamma_{14}^{\text{cr}} = \gamma_{24}^{\text{cr}}$	0.54∠22	0.75∠-85	0.02∠-149
γ_{34}^{cr}	0.33∠22	0.85∠-78	0.03∠-145
γ_{123}^{cr}	0.40∠12	0.35∠-160	0.00∠131
γ_{124}^{cr}	0.38∠9	0.35∠-161	0.00∠128
$\gamma_{134}^{\text{cr}} = \gamma_{234}^{\text{cr}}$	0.55∠17	0.39∠-159	0.00∠133
$\det(\mathbf{Z})^{\text{cr}}$	0.31∠-62	0.13∠117	0.00∠0.00

5.7.1 Impact of y_i, configuration 1, first resonance

Table 5.3 shows numerical values of y_1, y_2, $\mathcal{T}(z_{11}^{\text{cr1}})$,[1] $\mathcal{T}(\gamma_{12}^{\text{cr1}})$, $\mathcal{T}^{\text{cr1}}$ for four different cases of power flows and SCRs of 5 and 4. The table also shows the actual values at which $\mathcal{T}$ crosses the real axis, denoted as $\mathcal{T}^*$. The power flows considered give the largest values of $y_1 + y_2$ and $y_1 y_2$. Expression (5.21) only considers contributions from z_{11}^{cr}, z_{22}^{cr} and γ_{12}^{cr}, so $\mathcal{T}^*$ is shown for the sake of comparison.

Table 5.3: y_1, y_2, $\mathcal{T}(z_{11}^{\text{cr1}})$, $\mathcal{T}(\gamma_{12}^{\text{cr1}})$, $\mathcal{T}^{\text{cr1}}$ and $\mathcal{T}^*$ for different power flows and SCRs of 5(†) and 4(‡) for the first RF, configuration 1

Cases	P_{10}= 1 P_{20}= 1 P_{30}=−1 P_{40}=−1	P_{10}=−1 P_{20}= 1 P_{30}= 0 P_{40}= 0	P_{10}= 1 P_{20}=−1 P_{30}= 0 P_{40}= 0	P_{10}=−1 P_{20}=−1 P_{30}= 1 P_{40}= 1
†y_1	3.3∠-72$^{\text{o}}$	2.2∠-22$^{\text{o}}$	3.3∠-72$^{\text{o}}$	2.2∠-22$^{\text{o}}$
†‡y_2	1.0	1.0	−1.0	−1.0
†$\mathcal{T}(z_{11}^{\text{cr1}})$	7.1∠-65$^{\text{o}}$	5.9∠-23$^{\text{o}}$	5.9∠-97$^{\text{o}}$	2.5∠-46$^{\text{o}}$
†$\mathcal{T}(\gamma_{12}^{\text{cr1}})$	6.6∠-125$^{\text{o}}$	3.0∠1$^{\text{o}}$	4.5∠130$^{\text{o}}$	3.0∠-181$^{\text{o}}$
†$\mathcal{T}^{\text{cr1}}$	11.9∠-94$^{\text{o}}$	8.7∠-15$^{\text{o}}$	4.4∠-146$^{\text{o}}$	2.2∠-125$^{\text{o}}$
†$\mathcal{T}^*$	−6.5	no cross	−1.4	−0.6
‡y_1	3.2∠-116$^{\text{o}}$	2.8∠-54$^{\text{o}}$	3.2∠-116$^{\text{o}}$	2.8∠-54$^{\text{o}}$
‡$\mathcal{T}(z_{11}^{\text{cr1}})$	5.4∠-105$^{\text{o}}$	6.5∠-48$^{\text{o}}$	7.0∠-137$^{\text{o}}$	4.4∠-82$^{\text{o}}$
‡$\mathcal{T}(\gamma_{12}^{\text{cr1}})$	4.3∠-93$^{\text{o}}$	3.8∠-32$^{\text{o}}$	4.3∠87$^{\text{o}}$	3.8∠148$^{\text{o}}$
‡$\mathcal{T}^{\text{cr1}}$	9.7∠-100$^{\text{o}}$	10.2∠-42$^{\text{o}}$	4.9∠-175$^{\text{o}}$	3.5∠-138$^{\text{o}}$
‡$\mathcal{T}^*$	−7.1	no cross	−3.3	no cross

The first thing to highlight from the results in Table 5.3 is that the safest case is with $P_{10} = -1$ pu and $P_{20} = 1$ pu. This is due to the fact that with these values y_1 lies in the RHP and $y_2 \approx 1$. This means that, in all SCR cases both, $\mathcal{T}(z_{11}^{\text{cr1}})$ and $\mathcal{T}(\gamma_{12}^{\text{cr1}})$, are located in the RHP as well as $\mathcal{T}^{\text{cr1}}$, which is confirmed by $\mathcal{T}^*$ (no cross).

[1]Note that, in this particular case $\mathcal{T}(z_{11}^{\text{cr}}) = z_{11}^{\text{cr}}(y_1 + y_2)$ since $z_{11}^{\text{cr}} = z_{22}^{\text{cr}}$

In the case with SCR = 5, it can be seen that $\mathcal{T}(\gamma_{12}^{\mathrm{cr1}})$ has the most "detrimental" impact regarding instability since it is large and lies in the LHP. On the other hand, $\mathcal{T}(z_{11}^{\mathrm{cr1}})$ locates in the RHP in most of the cases, except when $P_{10} = 1$ pu and $P_{20} = -1$ pu, where it has an angle of 97°. The "favorable" contribution of $\mathcal{T}(z_{11}^{\mathrm{cr1}})$ is expected since, as discussed earlier, for SCR = 5, $\mathrm{re}[y_1] > 0$ around ω_1^{r} in for all P_{10}.

In the case with SCR = 4, the detrimental impact of $\mathcal{T}(z_{11}^{\mathrm{cr1}})$ to stability is more significant compared to $\mathcal{T}(\gamma_{12}^{\mathrm{cr1}})$, particularly in the cases where $P_{10} = 1$ pu. This is expected since $\mathrm{re}[y_1] < 0$ for $P_{10} > 0$ around ω_1^{r}. Note that the other **Z**-terms have also an impact on the system instability. In fact, in the load flow case with $P_{10} = P_{20} = -1$ pu and $P_{30} = P_{40} = 1$ pu, for SCR = 5, $\mathrm{re}[\mathcal{T}^{\mathrm{cr1}}] = -1.3$ while $\mathcal{T}^*$ crosses the real axis at -0.6. The same is true also for the same load flow case with SCR = 4 where $\mathrm{re}[\mathcal{T}^{\mathrm{cr1}}] = -2.6$ while $\mathcal{T}$ does not cross the real axis. Therefore, $\mathcal{T}^{\mathrm{cr}}$ should be taken only as an indication of instability risk.

5.7.2 Impact of y_i, configuration 1, second resonance

Table 5.4 shows the values of y_1, y_2, y_3, y_4, $\mathcal{T}(z_{11}^{\mathrm{cr2}})$, $\mathcal{T}(z_{33}^{\mathrm{cr2}})$, $\mathcal{T}(z_{44}^{\mathrm{cr2}})$, $\mathcal{T}(\gamma_{\mathrm{av}}^{\mathrm{cr2}})$, $\mathcal{T}^{\mathrm{cr2}}$ and $\mathcal{T}^*$ for $\omega_2^{\mathrm{r}} = 1.71$ pu. It can be seen that the most critical condition is when $y_3 = -1$ pu and $y_4 = -1$ pu since, in such a case, both $\mathcal{T}(z_{33}^{\mathrm{cr2}})$ and $\mathcal{T}(z_{44}^{\mathrm{cr2}})$ lie in the LHP. Moreover, in the unstable cases where $P_{30} = -1$ pu and $P_{40} = 1$ pu (or also $P_{30} = 1$ pu and $P_{40} = -1$ pu), the decisive detrimental impact comes mostly from $\mathcal{T}(z_{11}^{\mathrm{cr2}})$. This is because $\mathrm{re}[y_1] < 0$ for $P_{10} = 1$ for all SCRs and $\omega_2^{\mathrm{r}} = 1.71$ pu. In addition, $\mathrm{re}[y_1]$ is more negative for SCR = 5 than the one for SCR = 4, hence unstable cases take place with SCR = 5. The impact of $\mathcal{T}(\gamma_{\mathrm{av}}^{\mathrm{cr2}})$ in this resonance case is not significant since its angle is 90°. Finally, in the case when $P_{30} = 1$ pu and $P_{40} = 1$ pu, significant detrimental impact comes from $\mathcal{T}(\gamma_{\mathrm{av}}^{\mathrm{cr2}})$ and, to some extent, from $\mathcal{T}(z_{11}^{\mathrm{cr2}})$. However, they are all counteracted by the favorable contributions from $\mathcal{T}(z_{33}^{\mathrm{cr2}})$ and $\mathcal{T}(z_{44}^{\mathrm{cr2}})$.

5.8 Resonance characteristics, configuration 2

Table 5.5 presents vector representations of the **Z**-terms encirclements. They show that z_{ii}^{cr}-terms are dominant for the first RF (0.8 pu). Thus, $\mathcal{T}$ can be approximated as

$$\mathcal{T}^{\mathrm{cr1}} = z_{11}^{\mathrm{cr1}} y_1 + z_{22}^{\mathrm{cr1}} y_2 + z_{33}^{\mathrm{cr1}} y_3 + z_{44}^{\mathrm{cr1}} y_4 \tag{5.23}$$

for the first RF. In this case, the worst condition is that the "VSC loads" (VSC inverters) are PC-VSCs and also that the "VSC-sources" are DVC-VSCs, with $\mathrm{re}[y_i] < 0$ at the RF. This is possible if the ac system SCR of the DVC-VSC becomes significantly low. For example, for SCR = 2 and $P_{10} = 1$ pu, the studied VSC has $\mathrm{re}[y_1] \approx -7$ ($y_i = 7.1\angle -169$) for $\omega = 0.84$ pu. In these conditions, if $P_{20} = 1$ pu and $P_{30} = P_{40} = -1$ pu, then $\mathcal{T}^{\mathrm{cr}} \approx 4.6\angle 176°$, which indicates that the risk of instability is very high. Table 5.5 also shows that for the other frequencies the risk of instability is very low since all **Z**-terms are very low.

Table 5.4: $y_1, y_2, y_3, y_4, \mathcal{T}(z_{11}^{\mathrm{cr2}}), \mathcal{T}(z_{33}^{\mathrm{cr2}}), \mathcal{T}(z_{44}^{\mathrm{cr2}}), \mathcal{T}(\gamma_{\mathrm{av}}^{\mathrm{cr2}}), \mathcal{T}^{\mathrm{cr2}}$ and $\mathcal{T}^*$ for different power flows and SCRs of 5(†) and 4(‡) for the second RF, configuration 1

Cases	P_{10}=−1 P_{20}=−1 P_{30}= 1 P_{40}= 1	P_{10}= 1 P_{20}=−1 P_{30}=−1 P_{40}= 1	P_{10}= 1 P_{20}=−1 P_{30}= 1 P_{40}=−1	P_{10}= 1 P_{20}= 1 P_{30}=−1 P_{40}=−1
$\dagger y_1$	$2.2\angle$-57$^{\mathrm{o}}$	$2.4\angle$-123$^{\mathrm{o}}$	$2.4\angle$-123$^{\mathrm{o}}$	$2.4\angle$-123$^{\mathrm{o}}$
$\dagger\ddagger y_2$	-1.0	-1.0	-1.0	1.0
$\dagger\ddagger y_3$	1.0	-1.0	1.0	-1.0
$\dagger\ddagger y_4$	1.0	1.0	-1.0	-1.0
$\dagger\mathcal{T}(z_{11}^{\mathrm{cr2}})$	$1.0\angle$-162$^{\mathrm{o}}$	$1.5\angle$-119$^{\mathrm{o}}$	$1.6\angle$143$^{\mathrm{o}}$	$1.1\angle$-178$^{\mathrm{o}}$
$\dagger\mathcal{T}(z_{33}^{\mathrm{cr2}})$	$1.6\angle$-2$^{\mathrm{o}}$	$1.6\angle$178$^{\mathrm{o}}$	$1.6\angle$-2$^{\mathrm{o}}$	$1.6\angle$178$^{\mathrm{o}}$
$\dagger\mathcal{T}(z_{44}^{\mathrm{cr2}})$	$1.4\angle$-8$^{\mathrm{o}}$	$1.4\angle$-8$^{\mathrm{o}}$	$1.4\angle$172$^{\mathrm{o}}$	$1.4\angle$172$^{\mathrm{o}}$
$\dagger\mathcal{T}(\gamma_{\mathrm{av}}^{\mathrm{cr2}})$	$3.2\angle$-151$^{\mathrm{o}}$	$0.8\angle$98$^{\mathrm{o}}$	$0.8\angle$98$^{\mathrm{o}}$	$3.5\angle$-14$^{\mathrm{o}}$
$\dagger\mathcal{T}^{\mathrm{cr2}}$	$2.2\angle$-109$^{\mathrm{o}}$	$1.2\angle$-148$^{\mathrm{o}}$	$2.2\angle$122$^{\mathrm{o}}$	$1.0\angle$-137$^{\mathrm{o}}$
$\dagger\mathcal{T}^*$	no cross	-1.7	-1.8	-2.1
$\ddagger y_1$	$1.6\angle -79^{\mathrm{o}}$	$0.6\angle$151$^{\mathrm{o}}$	$0.6\angle$151$^{\mathrm{o}}$	$0.6\angle$151$^{\mathrm{o}}$
$\ddagger\mathcal{T}(z_{11}^{\mathrm{cr2}})$	$0.9\angle$-193$^{\mathrm{o}}$	$1.1\angle$-128$^{\mathrm{o}}$	$0.8\angle$91$^{\mathrm{o}}$	$0.3\angle$-45$^{\mathrm{o}}$
$\ddagger\mathcal{T}z_{33}^{\mathrm{cr2}}$	$1.6\angle$-2$^{\mathrm{o}}$	$1.6\angle$178$^{\mathrm{o}}$	$1.6\angle$-2$^{\mathrm{o}}$	$1.6\angle$178$^{\mathrm{o}}$
$\ddagger\mathcal{T}(z_{44}^{\mathrm{cr2}})$	$1.4\angle$-8$^{\mathrm{o}}$	$1.4\angle$-8$^{\mathrm{o}}$	$1.4\angle$172$^{\mathrm{o}}$	$1.4\angle$172$^{\mathrm{o}}$
$\ddagger\mathcal{T}(\gamma_{\mathrm{av}}^{\mathrm{cir2}})$	$2.5\angle$-179$^{\mathrm{o}}$	$0.8\angle$98$^{\mathrm{o}}$	$0.8\angle$98$^{\mathrm{o}}$	$0.5\angle$-163$^{\mathrm{o}}$
$\ddagger\mathcal{T}^{\mathrm{cr2}}$	$0.35\angle$-167$^{\mathrm{o}}$	$1.0\angle$-171$^{\mathrm{o}}$	$1.7\angle$87$^{\mathrm{o}}$	$3.3\angle$-178$^{\mathrm{o}}$
$\ddagger\mathcal{T}^*$	no cross	no cross	no cross	-3.6

5.9 Stability checking conditions and recommendations

The advantage of studying the stability in MTDC systems through the $\mathbf{Z}$-terms and $\mathbf{Y}$-terms, as defined in this thesis, is that the impact of the dc-network resonance characteristics (represented by the $\mathbf{Z}$-terms) and each terminal dynamics (represented by the $\mathbf{Y}$-terms) can be studied independently. Regarding the z_{ii}-terms, the safest condition from a stability point of view is that all $\mathrm{re}[y_i]$ are large and positive. Moreover, it has been shown that the largest contributions typically come from z_{ii}-terms. Then, with $\mathrm{re}[y_i]$ large and positive, the risk of instability is reduced as $\mathcal{T}(z_{ii}^{\mathrm{cr}})$ can counteract the negative impact of all the other encirclements. What can be inferred from the z_{ii}-terms is that, in order to decrease the risk of instability, VSC inverters should be in DVC mode since it is in these conditions that their "terminal conductance" is positive. On the other hand, it is a common practice to set VSC-sources in DVC mode due to the fact that, at these terminals, the voltages are the highest. However, it is in these cases when y_i can have a negative terminal conductance in specific frequency ranges. Thus, if a RF coincides with this range, one solution is to decrease the magnitude of y_i and if possible, to make $\mathrm{re}[y_i] > 0$ in that frequency range. Therefore, considering (5.15) the following condition can be used to check the risk of instability

$$\delta = z_{11}^{\mathrm{pk}}\mathrm{re}[y_1] + z_{22}^{\mathrm{pk}}\mathrm{re}[y_2] + \ldots + z_{\mathrm{nn}}^{\mathrm{pk}}\mathrm{re}[y_{\mathrm{n}}] \tag{5.24}$$

where z_{ii}^{pk} are the RPs. Note that in (5.24), the angles of z_{ii}^{pk} has been assumed zero since they are usually small. Ideally, if the angles of z_{ii}^{pk} are really zero and if the encirclements

Table 5.5: Encirclements mag. ($|\cdot|$ [pu]) and angles ($\angle\cdot$ [°]) for configuration 2

freq. [pu]	0.8	3.9	4.4
$z_{11}^{\rm cr} = z_{22}^{\rm cr}$	0.54∠-14	0.14∠-27	0.09∠-68
$z_{33}^{\rm cr}$	0.64∠-13	0.07∠20	0.13∠-26
$z_{44}^{\rm cr}$	0.65∠-14	0.07∠19	0.13∠-26
$\gamma_{12}^{\rm cr}$	0.02∠27	0.01∠-89	0.01∠-151
$\gamma_{13}^{\rm cr} = \gamma_{23}^{\rm cr}$	0.13∠-86	0.01∠-8	0.01∠-70
$\gamma_{14}^{\rm cr} = \gamma_{24}^{\rm cr}$	0.14∠-86	0.01∠-8	0.01∠-71
$\gamma_{34}^{\rm cr}$	0.02∠29	0.01∠-50	0.01∠-90
$\gamma_{123}^{\rm cr}$	0.01∠-46	0.00∠-87	0.00∠-128
$\gamma_{124}^{\rm cr}$	0.01∠-46	0.00∠-87	0.00∠-128
$\gamma_{134}^{\rm cr} = \gamma_{234}^{\rm cr}$	0.00∠-45	0.00∠-78	0.00∠-117
$\det(\mathbf{Z})^{\rm cr}$	0.00∠4	0.00∠-162	0.00∠102

are perfect circles that passes through origin, and if also the other **Z**-terms are neglectable, then the system is unstable if

$$\delta = z_{11}^{\rm pk}{\rm re}[y_1] + z_{22}^{\rm pk}{\rm re}[y_2] + \ldots + z_{\rm nn}^{\rm pk}{\rm re}[y_{\rm n}] \leq -1 \tag{5.25}$$

Thus, what can be claimed from (5.24) is that, the more negative δ is, the greater the risk of instability. Therefore, to make $\delta > 0$, (i.e. to improve stability) ${\rm re}[y_i]$ should be made positive and large. Expression (5.24), indicates also the way terminals interact. For example, a terminal i has a low impact on the system stability if $z_{ii}^{\rm pk}$ is very small. Moreover, (5.24) says that a negative ${\rm re}[y_i]$ at terminal i can be compensated by a positive ${\rm re}[y_j]$ at terminal j. The other **Z**-related terms, i.e. γ_{ij}, γ_{ijk}, …, $\det[\mathbf{Z}]$, usually decrease in magnitude as the order of the matrix that defines them increases. However, in some cases they have magnitudes comparable to the z_{ii} terms, especially the γ_{ij}-terms such as in configuration 1. In those situations, the following rule can be applied. The system is stable if $\delta > 0$ and

$$\sum |\gamma_{ij}^{\rm pk} y_i y_j| < 1 + \delta \tag{5.26}$$

This contradicts (5.24) since (5.26) does not allow $|y_i|$ a large value while (5.24) recommends to make ${\rm re}[y_i] > 0$ and large if possible. So, while (5.26) might be difficult to achieve, not fulfilling it does not mean that the system is unstable. In such cases, it is recommended to minimize $\sum |\gamma_{ij}^{\rm pk} y_i y_j|$ and perform a full Nyquist stability analysis. Note that (5.24), and in some cases (5.26), should be evaluated for every RF.

From the analysis performed in this chapter, the next steps can be followed in order to improve the system stability:

1. Obtain the **Z**-terms and determine the elements that have the highest impact on the system stability. In addition, determine the dc-network RFs;

2. Study the frequency response of every terminal. In the DVC-VSC studied in this thesis it follows that, typically, ${\rm re}[y_i] > 0$ for $P_{i0} < 0$. This means that stability can be improved by setting in DVC mode as many VSC inverters as possible. In the case of DVC-VSCs acting as sources, ${\rm re}[y_i] < 0$ must be avoided, and, if not possible, $|y_i|$ must be decreased around dc-network RFs;

3. If $\mathrm{re}[y_i] > 0$, stability can be improved by making $|y_i|$ greater. In the DVC-VSC studied in this thesis, this can be achieved by increasing the gains of the DVC. The impact will be higher if this is done at terminals with the highest z_{ii}^{pk}. However, consider also the impact of the γ_{ij}-terms;

4. In case of $\mathrm{re}[y_i] < 0$, the size of $|y_i|$ can be decreased by using filters tuned to the respective RF or by decreasing the DVC gains. However, this means also that the control of the system dc-bus voltage will be slower. This could be acceptable if some VSC inverters are in DVC mode with high gains meaning that they will be faster. On the other hand, to decrease the instability risk due to $\mathrm{re}[y_i] < 0$, the size of the respective z_{ii}^{pk} can be decreased by adding physical filters at the terminals. However, this adds an extra cost and losses to the system.

5.10 Simulation verifications

The system investigated in Section 5.3 with the dc-network configuration 1 from Table 5.1 is studied in this section. The VSCs are connected to an ac systems with SCR = 5, except VSC_1 which is connected to an ac system with SCR = 4. VSC_1 is in DVC mode, while the others are in PC mode. The VSC controllers are implemented as explained in Section 5.3. In addition, the VSCs are modeled as two-level converters with a switching frequency of 2 kHz. In the first simulated case, VSC_3 and VSC_4 maintain their power references to zero, while VSC_2 decreases its power to -1 pu. This sets the final powers as $P_1 = 1$ pu, $P_2 = -1$ pu, $P_3 = 0$ pu and $P_4 = 0$ pu, which, according to Table 5.3 is an unstable case due to the detrimental contribution from $\mathcal{T}(z_{11}^{\mathrm{cr}})$. In fact, using (5.24),

$$\delta = z_{11}^{\mathrm{pk}}(\mathrm{re}[y_1] + \mathrm{re}[y_2]) = 1.87(-1.4 - 1) = -4.5 \tag{5.27}$$

Figure 5.8 shows the simulation results, where it can be seen that instability takes place once VSC_1 reaches $P_1 = 1$ pu. Note that the RF is 1.78 pu (see Figure 5.13) and that the magnitude of the oscillations are considerably higher in voltages e_1 and e_2 compared to e_3 and e_4. According to (5.24), $\mathrm{re}[y_1] > 0$ improves stability. This can be achieved by decreasing the bandwidth of the ac voltages LPFs of VSC_1, α_{fl}. Figure 5.12 shows that for $\alpha_{\mathrm{fl}} = 1$ pu, then $y_1 = 1.14\angle -75^{\mathrm{o}}$. This means that $\delta = 1.87(0.29 - 1) = -1.33$, which is greater than the value in (5.27). In this case, $\mathcal{T}^* = -0.83$, meaning that system is stable, as shown in Figure 5.9. Stability could be further improved if VSC_2 is set to DVC mode, making δ even greater. Note that decreasing α_{fl} to 1 pu means that VSC_1 responds slower to ac side disturbances.

In the second simulation, VSC_1 is still the only one in DVC mode keeping $\alpha_{\mathrm{fl}} = 1$ pu. Powers references are decreased at both VSC_3 and VSC_4 from 0 to -1 pu. Furthermore, the power at VSC_2 is increased to 1 pu. The final power flow is $P_1 = 1$ pu, $P_2 = 1$ pu, $P_3 = -1$ pu and $P_4 = -1$ pu, which, according to Table 5.4 is unstable, mainly due to the detrimental contributions from $\mathcal{T}(z_{33}^{\mathrm{cr2}})$ and $\mathcal{T}(z_{44}^{\mathrm{cr2}})$. In fact

$$\delta = 1.63(-1) + 1.43(-1) = -3.06 \tag{5.28}$$

This is shown in Figure 5.10 that instability takes place when $-P_3$ almost reaches 1 pu. In this case, the RF is 2.05 pu (see Figure 5.13) and it can be seen that the magnitude of

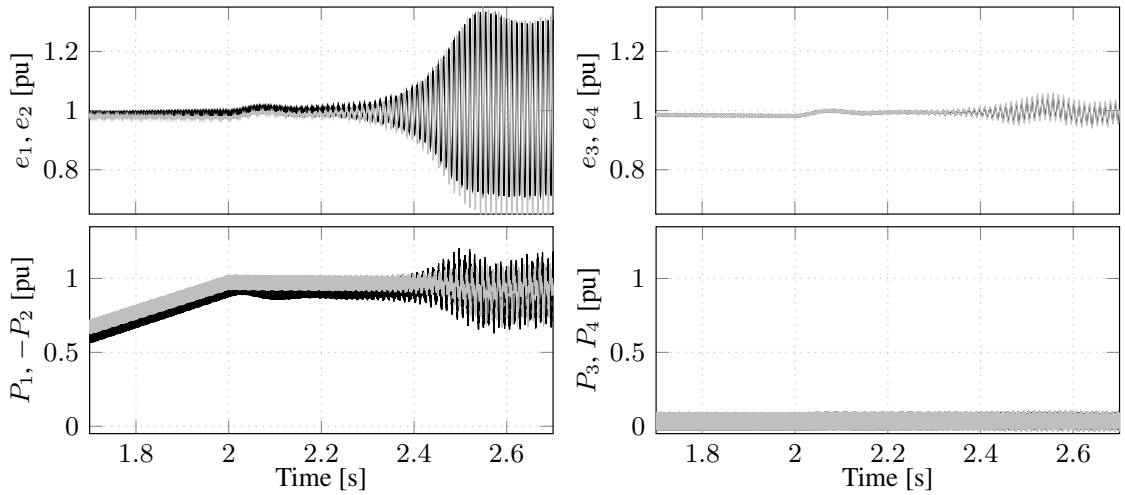

Figure 5.8: VSCs voltages (upper) and powers (bottom). Final powers $P_1 = +1$ pu, $P_2 = -1$ pu and $P_3 = P_4 = 0$. Black curves: e_1, e_3, P_1, P_3. Gray curves: e_2, e_4, P_2, P_4.

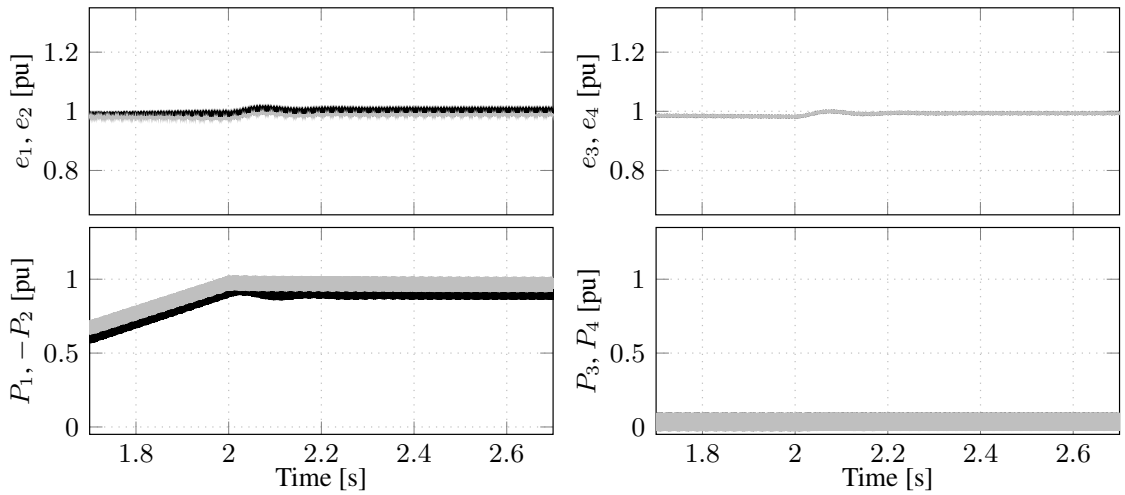

Figure 5.9: VSCs voltages (upper) and powers (bottom). Final powers as indicated in Figure 5.8. α_{f1} changed to 1 pu.Black curves: e_1, e_3, P_1, P_3. Gray curves: e_2, e_4, P_2, P_4.

the oscillations is more pronounced in voltages e_3 and e_4 compared to e_1 and e_2. Again, according to (5.24), one way to improve stability is to turn either y_3 or y_4 (or both together) to the RHP. In this case, this is achieved by turning VSC_3 to DVC mode due to the fact that z_{33}^{pk} pu has the greatest impact (see Table 5.2). The DVC of VSC_3 is implemented as a the droop controller DVC 3 of Figure 3.9, with parameters $e_3^{\mathrm{nl}} = 0.96$ pu and $k_{\mathrm{d}} = 0.05$ pu (with still SCR $= 5$ and LPF bandwidth of 4 pu). Moreover, the voltage reference of VSC_1 (still in DVC mode) is set to $e_1^{\mathrm{ref}} = 1.05$ pu. Figure 5.12 shows that for this type of DVC-VSC and $\omega_2^{\mathrm{r}} = 1.71$ pu, $y_1 = 2.04\angle -59^{\mathrm{o}}$. Then, $\delta = 1.63(1.06) + 1.43(-1) = 0.3$, which is much greater than (5.28), improving the system stability considerably. With this setup, i.e. VSC_1 and VSC_3 in DVC mode and VSC_2 and VSC_4 in PC mode, the same previous simulations are performed and the results, depicted in Figure 5.11, show that the system is stable for the final power flow.

One thing to highlight is that the RFs in both simulated cases are different, i.e. in the first

case it is 1.78 pu while in the second case it is 2.05 pu. The fact that the RFs are different in the simulation indicate that the instabilities shown in this section are due to two different resonance phenomena, as argued in Section 5.3. Moreover, in the first case, it can be seen that the resonance is more pronounced in e_1 and e_2 compared to e_3 and e_4. This clearly shows the dominant impact that z_{11} and z_{22} (impedances seen from terminals 1 and 2, in practice) have in the first RF, ω_1^{r}. On the other hand, in the second case, resonances are more pronounced in e_3 and e_4, which shows the dominant impact of z_{33} and z_{44} (impedances seen from terminals 3 and 4) in the second RF, ω_2^{r}. Note that, in the dc-network, RFs are 1.47 and 1.71 for the dc-network configuration 1 (see Table 5.2). This difference is due to the fact that the dc-network resonance characteristics are changed when the VSCs are connected to the network.

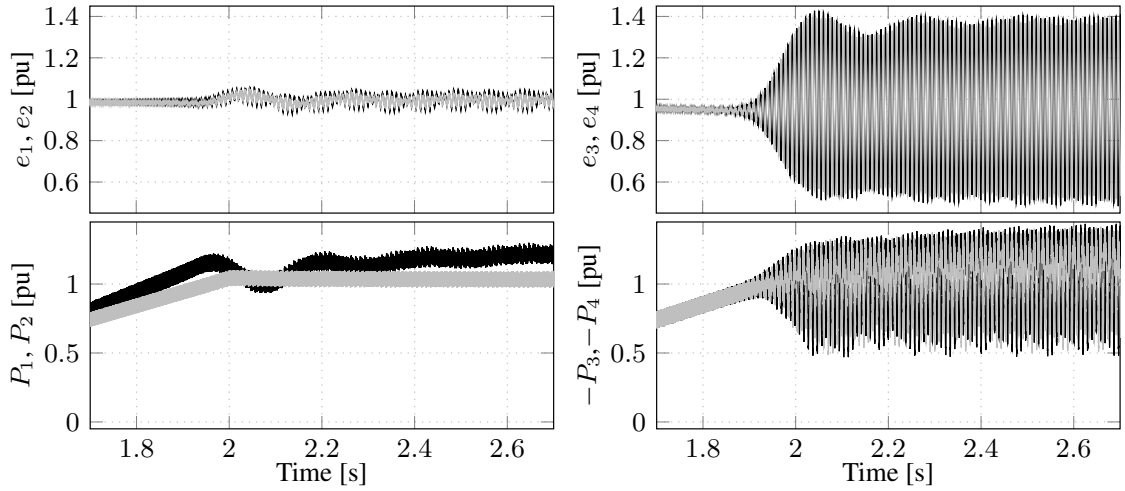

Figure 5.10: VSCs voltages (upper) and powers (bottom). Final powers $P_1 = P_2 = +1$ pu and $P_3 = P_4 = -1$. $\alpha_{\mathrm{f1}} = 1$ pu. Black curves: e_1, e_3, P_1, P_3. Gray curves: e_2, e_4, P_2, P_4.

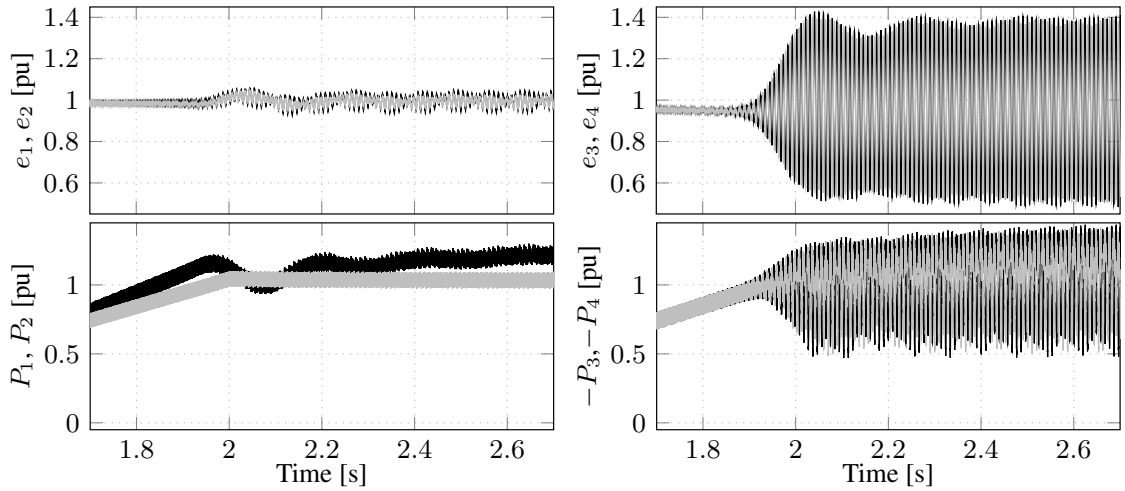

Figure 5.11: VSCs voltages (upper) and powers (bottom). Final powers as indicated in Figure 5.10. VSC_3 changed to DVC droop control. Black curves: e_1, e_3, P_1, P_3. Gray curves: e_2, e_4, P_2, P_4.

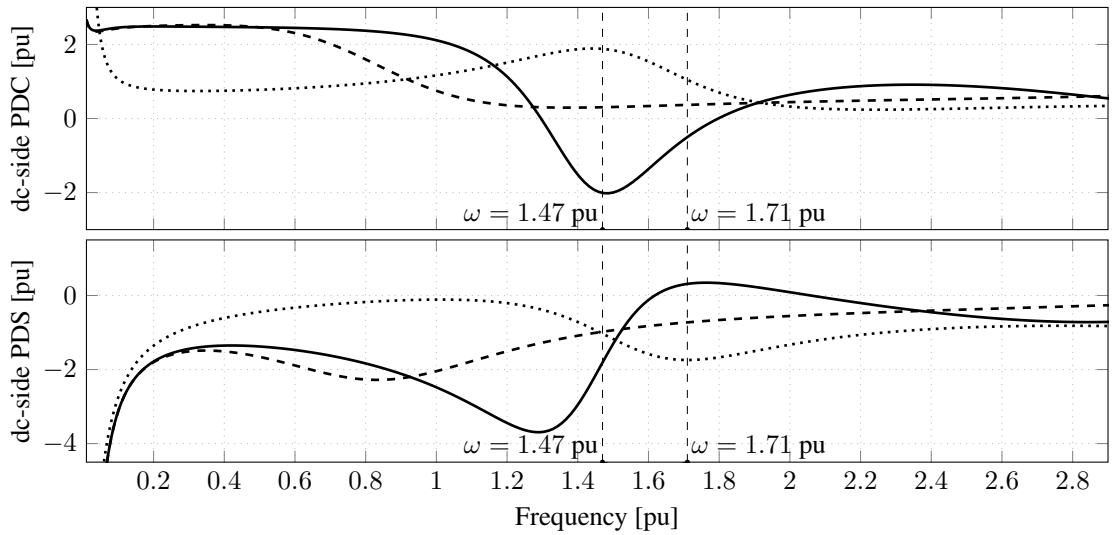

Figure 5.12: DC-side PDC and PDS for VSC with SCR = 4 and LPF with $\alpha_{\mathrm{f1}} = 4$ pu (solid), with SCR = 4 and LPF with $\alpha_{\mathrm{f1}} = 1$ pu (dashed), and with SCR = 5 and LPF, $\alpha_{\mathrm{f1}} = 4$ pu and with droop DVC with $k_{\mathrm{d}} = 0.05$ pu (dotted).

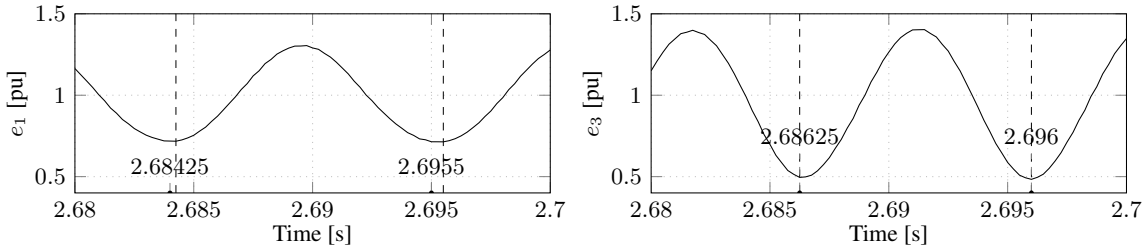

Figure 5.13: Detailed e_1 from Figure 5.8 (Left) and e_3 from Figure 5.10 (Right). The oscillation period for e_1 is 11.25ms (RF of 1.78 pu) and for e_3 is 9.75 ms (RF of 2.05 pu).

5.11 Conclusions

In this chapter, instabilities originated from dc-network resonances have been investigated in MTDC systems. Subsystems referred to as $\mathbf{Z}$, which represents the dc-network and $\mathbf{Y}$, which represents the VSCs, have been defined. Subsequently, $\mathbf{Z}$-terms have been defined and interpreted as encirclements that take place around the RFs. The advantage of the $\mathbf{Z}$-terms is that they clearly revealed the impact of each terminal on the system stability. For instance, the $\mathbf{Z}$-terms show that instabilities related to resonances can be triggered independently at different terminals. This is shown theoretically in Section 5.3 for a four-terminal HVDC system, where, for dc-network configuration 1, z_{11} and z_{22} have the greatest impact on the first resonance, while for the second resonance z_{33} and z_{44} are the ones with greatest impact. In fact, the simulations presented in Section 5.10 show that, if instability related to the first resonance is triggered, voltages in terminal 1 and 2 oscillated more pronouncedly, compared to voltages in terminals 3 and 4. Consistent results are shown when instability is triggered for the second resonance. The analysis of the $\mathbf{Z}$-terms also shows the way different terminals interact. For example, in the dc-network configuration 1, it has been shown that terminals 1 and 2 contribute to instabilities related to the first resonances. This means that a problem introduced in one terminal, let us say terminal 1, could be alleviated through

actions in terminal 2. This also means that, actions taken in terminal 3 or 4 would have very little, or almost no effect on improving the system stability.

Regarding the $\mathbf{Y}$-terms, the way they influence on the system stability is rather similar to the dc-side PDA defined in Chapter 2. Basically, instability risk increases in cases where a negative real part of a $\mathbf{Y}$-term coincides with a dc-network RF. This occurs for some scenarios in DVC-VSCs and always for PC-VSCs acting as inverters. Then, through simulations, it has been shown that making the real parts of the $\mathbf{Y}$-terms positive contribute to turning the system stable. With the VSCs assumed in this thesis, it is recommended to set the VSC inverters in DVC mode whenever possible, and to watch for the real parts of the corresponding $\mathbf{Y}$-term of VSC sources acting in DVC mode.

Chapter 6

Stability analysis in MTDC systems: Verifications in RTDS

The aim of this Chapter is to provide further evidence of the theoretical findings presented in Chapter 5. This is carried out through an laboratory setup implemented in an RTDS. In this setup, a four-terminal HVDC system is implemented and it is interfaced with a Digital Signal Processor (DSP), which controls two of the VSCs. Distributed parameter models are implemented in RTDS to represent cables and OHL, meaning that the DSP operates in a quasi-real scenario. The impact of various factors is investigated, such as: dc-network configuration, strength of the ac system to which the VSCs are connected, and dc-bus voltage control strategies. It should be mentioned that these experiments have been performed in the laboratory facilities of the FREEDM center of North Carolina State University and that the results presented in this chapter are the outcome of our cooperation. This chapter is based on the work presented in Paper IX.

6.1 Hardware setup

The system under study is depicted in Figure 6.1, where it can be seen that VSC_1 and VSC_3 are externally driven by a DSP. Moreover, consider that the ratings and the electrical configurations of each VSC are similar to the ones stated in Chapter 5. The hardware test setup implemented for this study is displayed in Figure 6.2, where it can be seen the physical connections between the RTDS, an interface card and a controller card. This is better appreciated in the schematic shown Figure 6.3, where the functionality of each component is indicated along with the signals exchanged between them. The controller card is a DSP, model TMS320F28335 [58], which is used to externally control VSC_1 and VSC_3. This DSP needs an interface card in order to send digital signals to the RTDS and receive analog signals from the RTDS. This is due to the fact that the voltage range of the RTDS analogue outputs/inputs is ± 10 V while the voltage range of the DSP card analog inputs/outputs is $0-3$ V. The analogue signals are then discretized in the DSP and used in the control algorithm, which is implemented as the discrete time controller explained in Section 3.8. Fourteen analog signals are sent from the RTDS to the DSP (seven for each

VSC): the three phases of each u_{g1} and u_{g3}, the three phases of i_{f1} and i_{f3}, and the pole-to-pole terminal voltages e_1 and e_3. The controller then generates twelve firing signals (six for each VSC), which are conditioned through the interface card and then sent to the RTDS digital inputs. The firing signals are generated through the synchronous and asymmetric sampling PWM explained in Section 3.8 and in Figure 3.14. In our case, the carrier's frequency is 2 kHz (also the VSC switching frequency), so the DSP sampling frequency is 4 kHz. VSC_2 and VSC_4 are controlled internally through continuous time control blocks available in RTDS with controllers implemented as in Section 2.1.2.

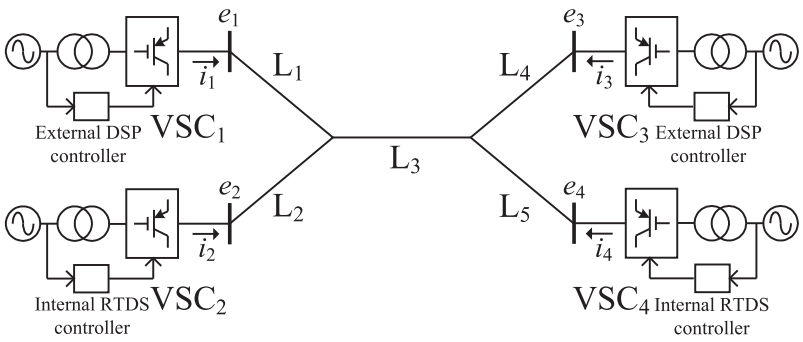

Figure 6.1: Four-terminal VSC HVDC under study.

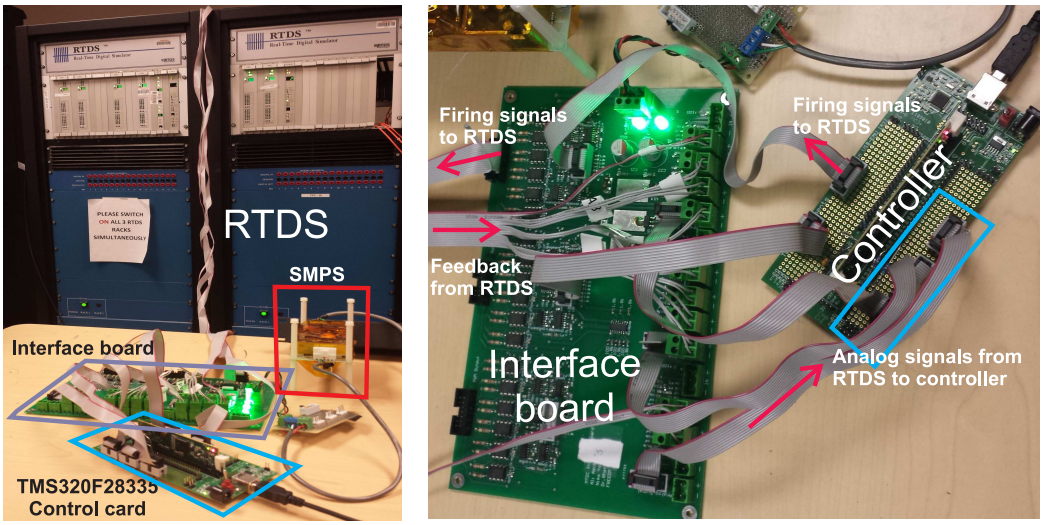

Figure 6.2: RTDS setup with the DSP control card and interface board.

6.2 RTDS models

In order to reduce the RTDS computation time, it is possible to model *only* the group of elements that has small time constants as small time-step (small-DT) models. This is the case of the two-level VSCs that have a switching period of 500 µs. For the amount of components modeled as small-DT models, a time step of 3.47µs is obtained for our model. Thus, the switches, together with the VSC ac side elements and the dc-side capacitors[1] are

[1] All the elements depicted in Figure 2.2 are modelled as small-DT.

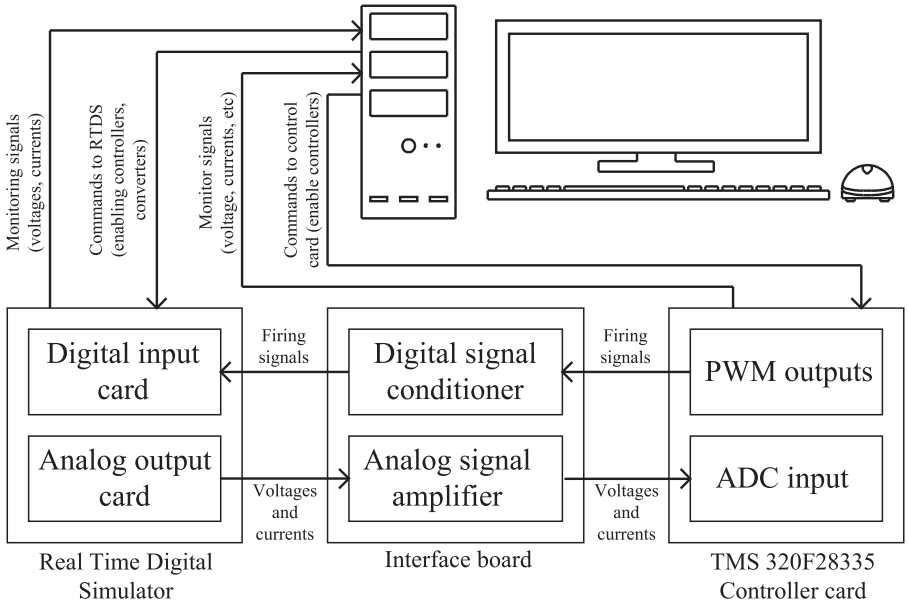

Figure 6.3: Schematic of the test setup

modelled in small-DT. On the other hand, other elements with larger time constants can be modeled as large time step (large-DT) models in order to relieve the computational burden for the RTDS. The "smallest" time step obtained for the large-DT models is 66µs. This is suitable for cables and OHLs modeled in large-DT since their RFs are between 1-5 pu (periods of 4ms - 20ms).

Table 6.1: DC network configurations

Cases	L1-km	L2-km	L3-km	L4-km	L5-km
Configuration 1	OHL-100	OHL-100	Cable-200	OHL-70	OHL-80
Configuration 2	OHL-30	OHL-30	Cable-200	OHL-50	OHL-60
Configuration 3	Cable-50	Cable-50	Cable-200	Cable-50	Cable-60

6.3 Results and analysis

Three different dc-network configurations, as indicated in Table 6.1, are studied. The geometrical configurations of the cable and the OHL mentioned in Table 6.1 are as indicated in Figure 4.4. In order to identify dc-network resonances, the frequency response of the z_{ii}-terms is obtained. This is achieved through applying a sinusoidal voltage at the bus of interest and measuring the respective current, as indicated in Figure 6.4. The block called "interface" in the figure represents a model introduced by RTDS as an interface between small-DT with large-DT models. This interface is a TL Bergeron model with a travelling time equal to the large-DT time step, 66µs. This block has a small impact on the z_{ii}-terms, but non-neglectable, so it has to be considered in the analysis.

The following power flow (PF) sequences are tested in different conditions:

PF sequence 1: Initially $P_1{=}P_2{=}P_3{=}P_4{=}0$. Then, P_4 is changed to -0.5 pu;

PF sequence 2: Initially $P_1{=}P_2{=}P_3{=}P_4{=}0$. Then, P_2 is changed to -1;

PF sequence 3: Initially $P_1{=}P_2{=}P_3{=}P_4{=}0$. Then, P_3 and P_4 are varied to -0.5 pu.

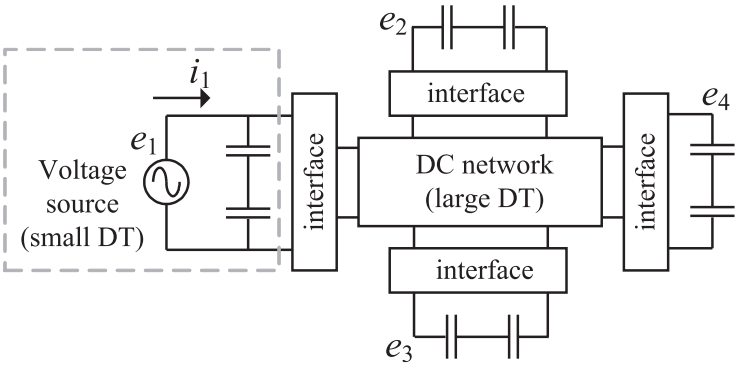

Figure 6.4: Measurement setup to obtain the frequency response of z_{11}

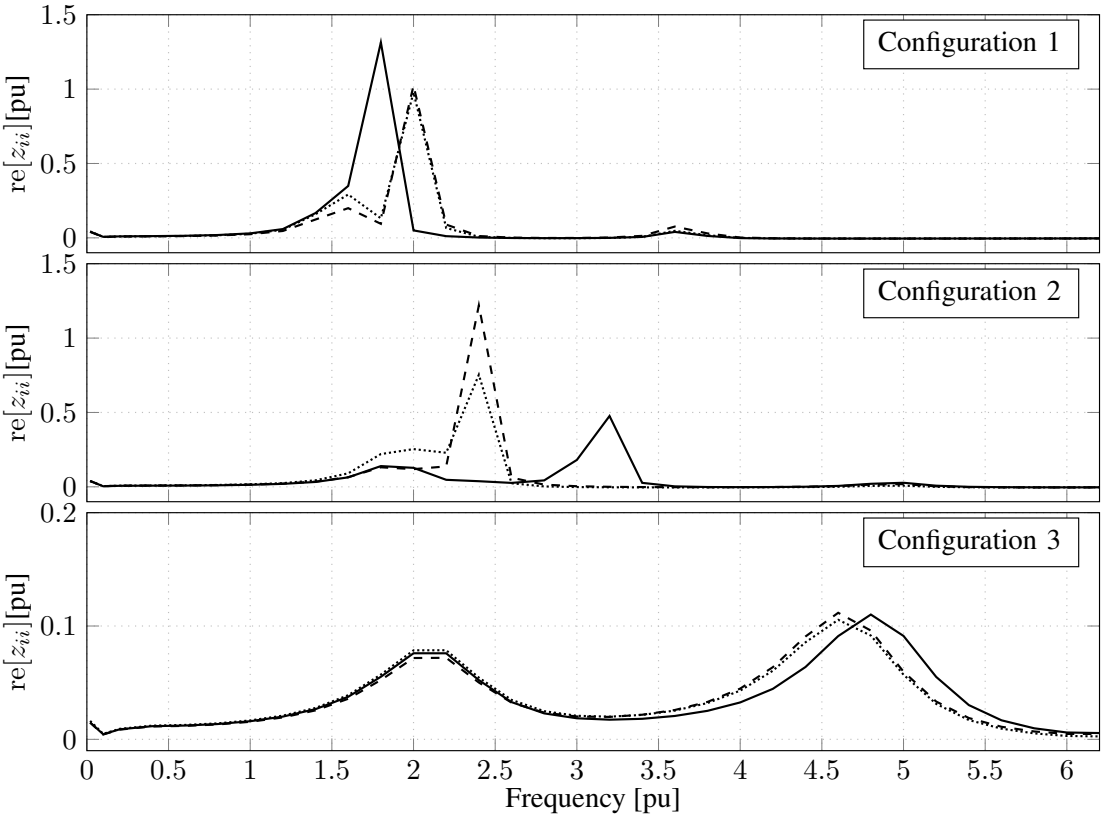

Figure 6.5: $\mathrm{re}[z_{11}] = \mathrm{re}[z_{22}]$ (solid), $\mathrm{re}[z_{33}]$ (dashed) and $\mathrm{re}[z_{44}]$ (dotted) and for dc-network configuration 1 (upper), configuration 2 (middle), and configuration 3 (bottom).

6.4 Analysis of dc-network configuration 1

The results of the frequency scan for each configuration are shown in Figure 6.5 and numerical values of z_{ii} for each resonance are presented in Table 6.2. It can be seen that,

for the first configuration, there are two dominant RFs, $\omega_1^{\mathrm{r}} = 1.8$ pu and $\omega_1^{\mathrm{r}} = 2$ pu. For $\omega_1^{\mathrm{r}} = 1.8$ pu, the values in Table 6.2 show that z_{11} and z_{22} are dominant, which means that VSC_1 and VSC_2 are more likely to trigger an instability for this resonance. In this case, (5.24) can be simplified as

$$\delta^1 = z_{11}^{\mathrm{pk1}}\mathrm{re}[y_1] + z_{22}^{\mathrm{pk1}}\mathrm{re}[y_2] \tag{6.1}$$

This can be shown through a test in the four-terminal HVDC system. For this test, VSC_1 is in DVC mode, while VSC_2, VSC_3 and VSC_4 are in PC mode. PF sequence 1 is tested and,

Table 6.2: RPs and RFs for the configurations in Table 6.1

RF [pu]	z_{11}^{pk}	z_{22}^{pk}	z_{33}^{pk}	z_{44}^{pk}
(configuration 1) $\omega_1^{\mathrm{r}} = 1.8$	1.31	1.31	0.09	0.13
(configuration 1) $\omega_2^{\mathrm{r}} = 2.0$	0.08	0.08	1.02	0.97
(configuration 2) $\omega_1^{\mathrm{r}} = 2.4$	0.04	0.04	1.22	0.75
(configuration 2) $\omega_2^{\mathrm{r}} = 3.2$	0.47	0.47	0.00	0.00
(configuration 3) $\omega_1^{\mathrm{r}} = 2.0$	0.08	0.08	0.07	0.08
(configuration 3) $\omega_2^{\mathrm{r}} = 4.6$	0.09	0.09	0.11	0.11

as a consequence, VSC_1 increases P_1 to around 0.5 pu. Figure 6.6 shows the voltages and powers of the four terminals, and it can be seen that voltages start oscillating even before reaching $P_1 = 0.5$ pu. Moreover, it can be seen that the oscillations are more pronnounced in voltages e_1 and e_2. Considering that $P_2 = 0$ (i.e. $y_2 = 0$) in this test, (6.1) indicates that VSC_1 is triggering the instability. Figure 6.7 shows $\mathrm{re}[y_1]$ for different conditions[1], and curve 1 corresponds to this test (SCR = 5 and with a LPF bandwidth of $\alpha_{\mathrm{f1}} = 4$ pu). In fact, Figure 6.7 shows that for frequencies between 1.5 and 2 pu, $\mathrm{re}[y_1] < 0$ and that the minimum value of $\mathrm{re}[y_1]$ is -1.43 pu for a frequency of 1.75 pu, which is around the RF of 1.8 pu. This actually makes $\delta = 1.31(-1.43) = -1.87$ pu, which indicates that there is a high risk of instability.

6.4.1 Impact of increasing $\mathrm{re}[y_1]$

According to (6.1), one solution is to increase $\mathrm{re}[y_1]$ so that it turns positive around the RF of interest. This is achieved by changing $\alpha_{\mathrm{f1}} = 0.4$ pu, as shown by curve 2 of Figure 6.7, where it can be seen that $\mathrm{re}[y_1]$ is positive around the RF of 1.8 pu. PF sequence 1 is tested again with $\alpha_{\mathrm{f1}} = 0.4$ pu for VSC_1, and it can be seen in Figure 6.8 that the system remains stable. Actually, in this case, $\delta = 1.31(0.49) = 0.64$ which indicates that the system stability improves with this change in the control system. Another test that can show how much stability has improved by making $\alpha_{\mathrm{f1}} = 0.4$ pu is by testing the PF sequence 2. With this test only the impact of the first resonance is observed since $P_3 = P_4 = 0$. The results of this test, depicted in Figure 6.9, show that the system reaches the setpoint without turning unstable. In fact, $\delta = 1.31(0.49) + 1.31(-1) = -0.67$, which is negative but still greater than the very first tested case, which means that the risk of instability has decreased.

[1] A procedure to obtain the frequency response of y_i for DVC-VSCs is presented in [59]

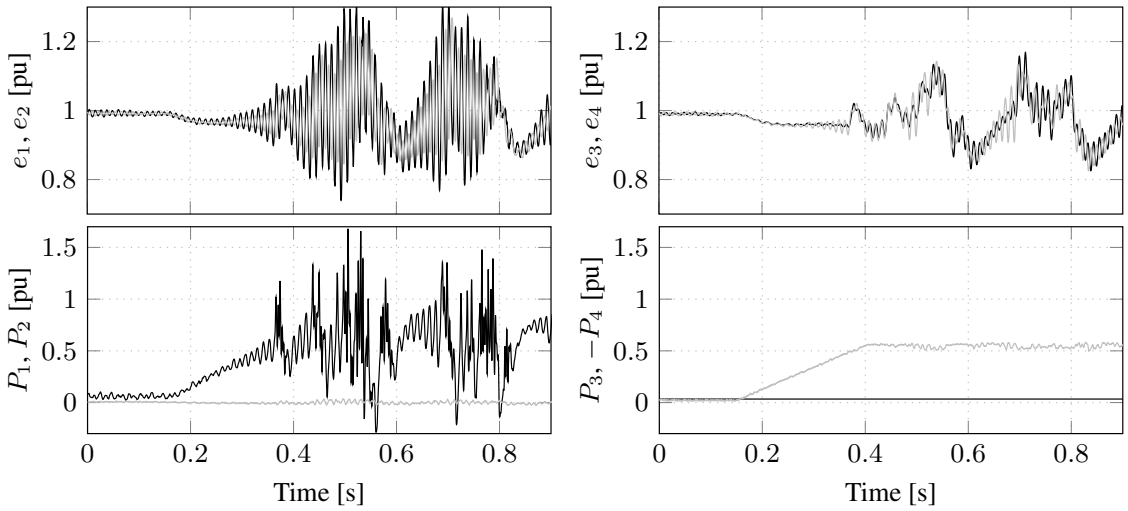

Figure 6.6: First dc-network configuration. Test for PF sequence 1. VSC_1 is in DVC, while VSC_2, VSC_3 and VSC_4 are in PC mode. In VSC_1, SCR=5 and $\alpha_{\text{f1}} = 4$ pu. Black curves: e_1, e_3, P_1 and P_3. Gray curves: e_2, e_4, P_2, P_4.

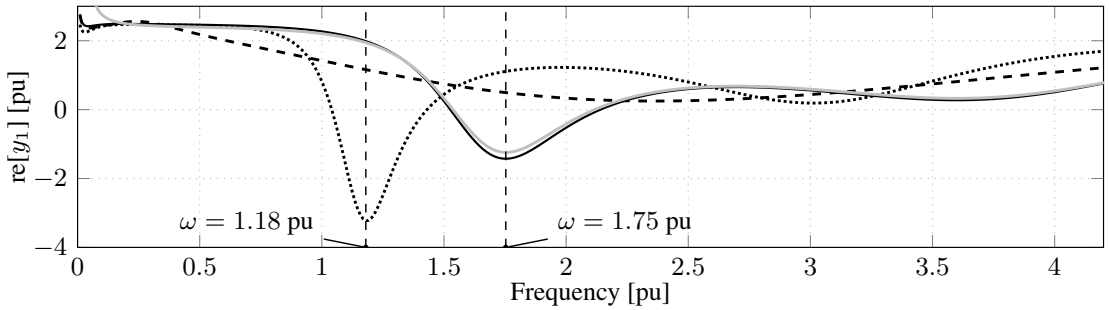

Figure 6.7: $\text{re}[y_1]$ for $P_1 = 1$ and for four cases. Curve 1 (solid black): SCR = 5, $\alpha_{\text{f1}} = 4$ pu. Curve 2 (dashed): SCR=5, $\alpha_{\text{f1}} = 0.4$ pu. Curve 3 (dotted): SCR=3 and $\alpha_{\text{f1}} = 4$ pu. Curve 4 (solid gray): droop control with $k_{\text{d}} = 0.05$, SCR=5 and $\alpha_{\text{f1}} = 4$ pu.

6.4.2 Impact of the second resonance

Regarding the second resonance, $\omega_2^{\text{r}} = 2$ pu, it can be seen from Table 6.2 that z_{33} and z_{44} are more dominant, which means that instability related to the second resonance is triggered mainly by VSC_3 and VSC_4. In this case, (5.24) can be simplified as

$$\delta^2 = z_{33}^{\text{pk}}\text{re}[y_3] + z_{44}^{\text{pk}}\text{re}[y_4] \tag{6.2}$$

This condition can be tested by keeping VSC_1 in DVC mode with $\alpha_{\text{f1}} = 0.4$ pu. As shown in the previous tests, this guarantees that instability related to the first resonance is not triggered. PF sequence 3 is tested, which means that $\delta = 1.02(-0.5) + 0.97(-0.5) = -1$ for the second RF. The result of the test is shown in Figure 6.10 and it can be seen that when P_4 reaches -0.5 pu, oscillations start in voltages e_3 and e_4. A close look to the figures shows that the oscillation frequency of the voltages in Figure 6.6 is 1.66 pu while in Figure 6.10 it is 1.98 pu. In addition, for the first resonance instability, oscillations in e_1 and e_2 are more pronounced than in e_3 and e_4, and similarly for the second resonance instability. These two facts clearly show that the two unstable cases are due to two different resonance phenomena.

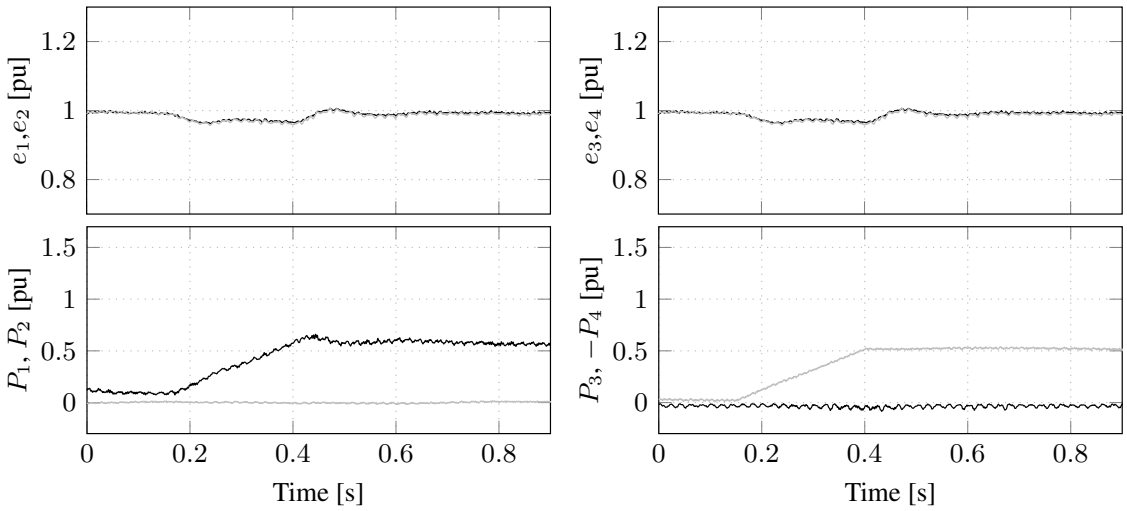

Figure 6.8: First dc-network configuration. Test for PF sequence 1. VSC_1 is in DVC, while VSC_2, VSC_3 and VSC_4 are in PC mode. In VSC_1, SCR=5 and $\alpha_{f1} = 0.4$ pu. Black curves: e_1, e_3, P_1 and P_3. Gray curves: e_2, e_4, P_2, P_4.

6.4.3 Impact of SCR

Let us go back to the first resonance case, i.e. $\omega_1^r = 1.8$ pu. In this case, the LPF bandwidth is changed back to $\alpha_{f1} = 4$ pu in VSC_1, but, at the same time, the ac system SCR is changed to 3. Curve 3 of Figure 6.7 shows that, for this case, $\mathrm{re}[y_1]$ is positive for frequencies around 1.8 pu. In fact $\delta = 1.31(1.16) = 1.52$. However, observe that Figure 6.7 also shows that the frequency range where $\mathrm{re}[y_i] < 0$ has switched to lower frequencies with the minimum $\mathrm{re}[y_i]$ taking place at frequency of 1.18 pu. The PF sequence 1 is tested again, and, it can be seen that, despite VSC_1 having the same controller configuration as in the very first test ($\alpha_{f1} = 4$ pu) instability does not take place due to the fact that $\mathrm{re}[y_1]$ has become positive for SCR=3.

6.4.4 Impact of droop controller

In order to investigate whether instability with respect to resonance 1 (and resonance 2) can be improved by having more than one VSC in DVC mode, VSC_1 and VSC_3 are switched to voltage droop control (DVC 3 from Section 3.6). VSC_1 droop DVC parameters are $e_1^{nl} = 1.07$ pu and $k_{d1} = 0.05$ pu. VSC_3 droop DVC parameters are $e_3^{nl} = 1$ pu and $k_{d3} = 0.05$ pu. These droop DVC parameters give initially $P_1 = 0.25$ pu, $P_2 = 0$ pu, $P_3 = -1$ pu, and $P_4 = 0.85$. Then, VSC_4 power setpoint is changed to 0 giving the following powers at t = 0.8 s: $P_1 = 0.6$ pu, $P_2 = 0$, $P_3 = -0.52$ pu and $P_4 = 0$ pu. It can be seen that instability takes place when VSC_1 reaches around 0.6 pu. This is in agreement with (6.1), which indicates that the other terminals have almost no impact on the system instability with respect to the first resonance. Therefore, the control mode of either VSC_3 and VSC_4 does not have any impact on the system stability in this case. In addition, curve 4 of Figure 6.7 shows that there is almost no difference with the corresponding $\mathrm{re}[y_i]$ for a VSC-DVC with no droop control. Hence, instability occurs almost at the same power level

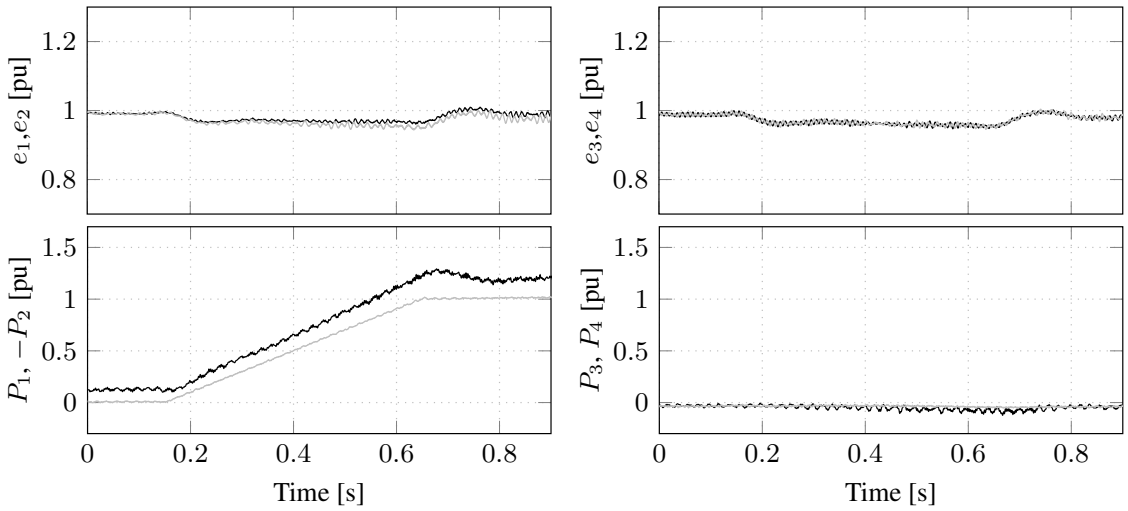

Figure 6.9: First dc-network configuration. Test for PF sequence 2. VSC_1 is in DVC, while VSC_2, VSC_3 and VSC_4 are in PC mode. In VSC_1, SCR=5 and $\alpha_{\text{f1}} = 0.4$ pu. Black curves: e_1, e_3, P_1 and P_3. Gray curves: e_2, e_4, P_2, P_4.

of VSC_1 compared to the case depicted in Figure 6.6. Instability with respect to the second resonance and having VSC_1 and VSC_3 in droop DVC mode can be tested with a reverse power flow. In this case the droop DVC parameters are $e_1^{\text{nl}} = 1$ pu and $k_{\text{d1}} = 0.05$ for VSC_1, and $e_3^{\text{nl}} = 1.15$ pu and $k_{\text{d3}} = 0.1$ pu for VSC_3. With this settings, the initial powers are $P_1 = -1.18$ pu, $P_2 = 0$ pu, $P_3 = 0.55$ pu and $P_4 = 0.55$ pu. Then, P_4 is changed to 0 pu which leads to P_3 to increase to around 0.85 pu before losing stability. Oscillations appear and they are more pronounced in e_3 and e_4. Figure 6.14 shows a close look at voltage e_1 from Figures 6.12 and e_3 from Figure 6.13. This figure shows that the RF in the first case is around 1.76 pu, while in the second case the RF is around 2.1 pu. Again, this clearly shows that the instabilities are due to two different resonance phenomenon. Moreover, with regards to the first resonance, VSC_3 and VSC_4 have no impact on the system stability, as implied by (6.1). Likewise, the same is true with respect to the second resonance, i.e. VSC_1 and VSC_2 have no impact in this case, which is also implied by (6.2).

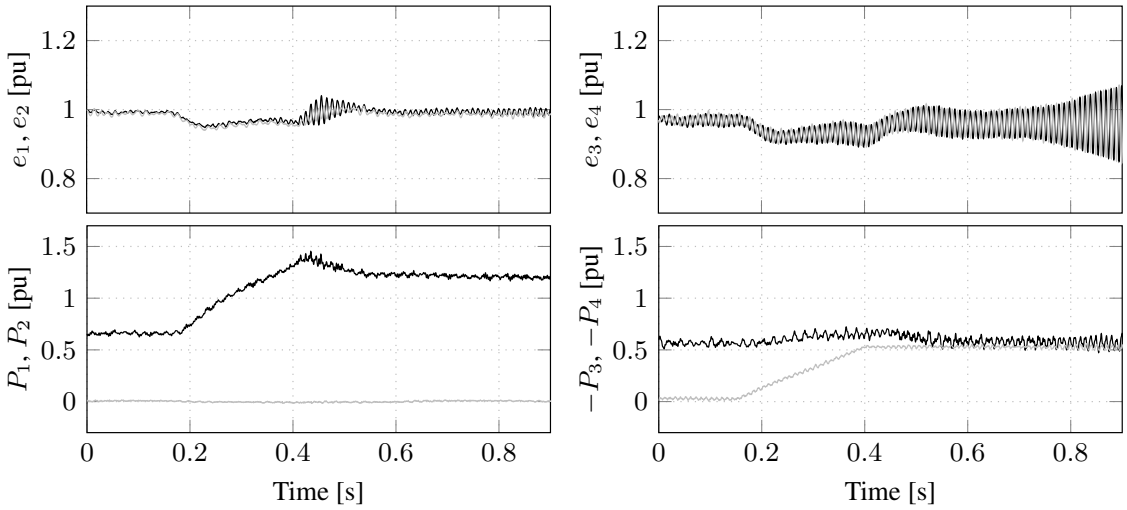

Figure 6.10: First dc-network configuration. Test for PF sequence 3. VSC_1 is in DVC, while VSC_2, VSC_3 and VSC_4 are in PC mode. In VSC_1, SCR=5 and $\alpha_{\text{f1}} = 0.4$ pu. Black curves: e_1, e_3, P_1 and P_3. Gray curves: e_2, e_4, P_2, P_4.

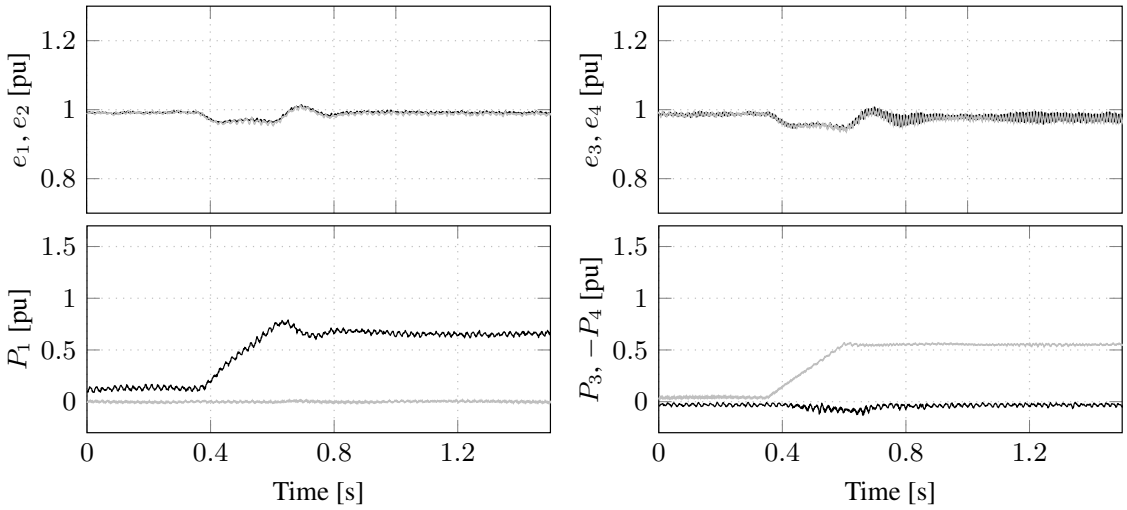

Figure 6.11: First dc-network configuration. Test for PF sequence 1. VSC_1 is in DVC, while VSC_2, VSC_3 and VSC_4 are in PC mode. In VSC_1, SCR=3 and $\alpha_{\text{f1}} = 4$ pu. Black curves: e_1, e_3, P_1 and P_3. Gray curves: e_2, e_4, P_2, P_4.

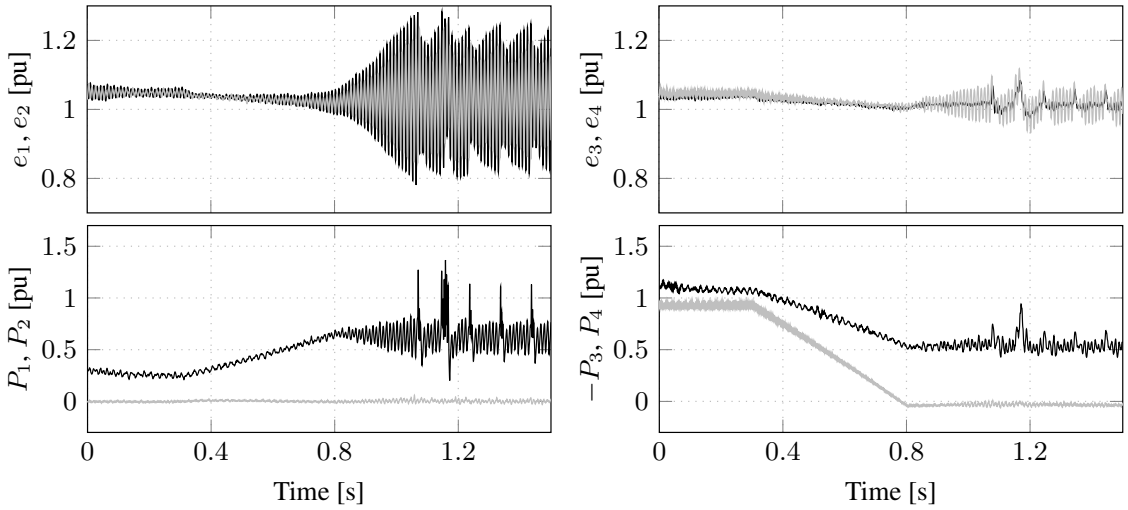

Figure 6.12: First dc-network configuration. VSC_1 and VSC_3 implemented with droop DVCs. The final powers are $P_1 = 0.6$ pu, $P_2 = 0$ pu, $P_3 = -0.52$ pu, $P_4 = 0$ pu. Black curves: e_1, e_3, P_1, P_3. Gray curves: e_2, e_4, P_2, P_4.

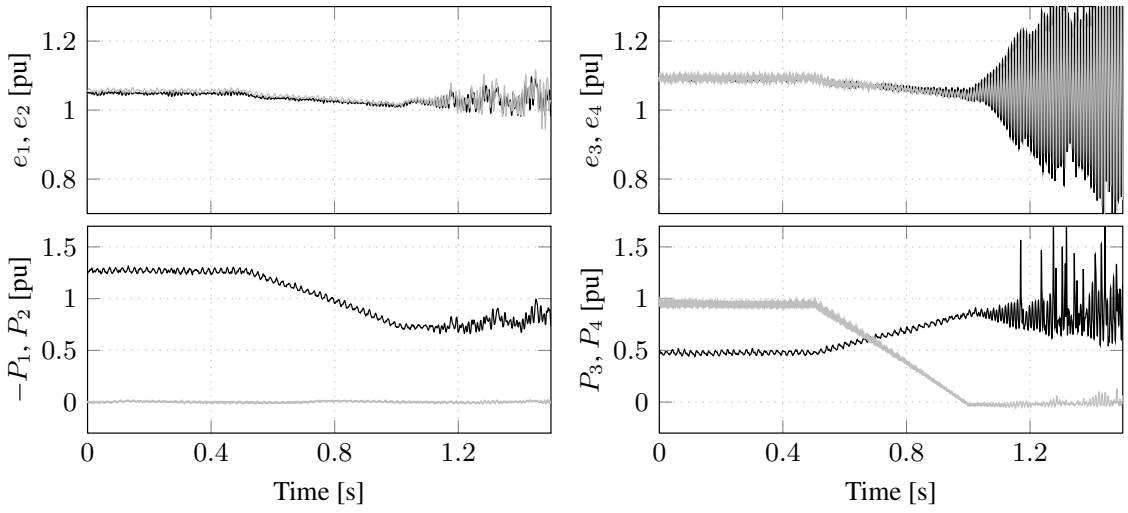

Figure 6.13: First dc-network configuration. VSC_1 and VSC_3 implemented with droop DVCs. The final powers are $P_1 = -1.18$ pu, $P_2 = 0$ pu, $P_3 = 0.55$ pu, $P_4 = 0.55$ pu. Black curves: e_1, e_3, P_1, P_3. Gray curves: e_2, e_4, P_2, P_4.

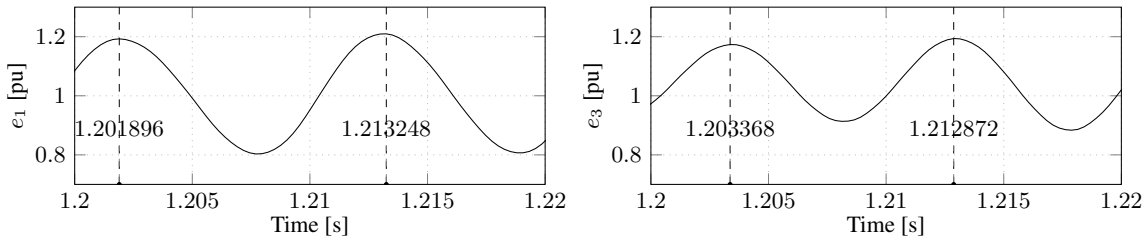

Figure 6.14: Zoomed voltages: e_1 from Figure 6.12 (Left) and e_3 from Figure 6.13 (Right). Oscillation period for e_1 in this figure is 11.35ms (RF of 1.76 pu) and for e_3 is 9.5 ms (RF of 2.10 pu).

6.5 Analysis of dc-network configuration 2 and 3

In the second dc-network configuration (see Table 6.1), the lengths of the TLs are changed, resulting in the frequency responses of z_{ii} depicted in Fig. 6.5. As shown in Table 6.2, there are two RF, $\omega_1^{\mathrm{r}} = 2.4$ pu and $\omega_2^{\mathrm{r}} = 3.2$ pu. Let us beging with the second resonance. It can be seen that the instability risk is low since the RPs are low. The worst scenario is that both, VSC_1 and VSC_2, are in PC mode and act as load with a power setpoint of -1 pu. Having any of those VSCs in DVC mode decreases the risk of instability since, as shown in Figure 6.7, for $\omega_2^{\mathrm{r}} = 3.2$ pu, $\mathrm{re}[y_1]$ is positive for all the analyzed cases. Regarding the first resonance, $\omega_1^{\mathrm{r}} = 2.4$ pu, terminals 3 and 4 are the ones with the greatest impact in this case. Then, the worst scenario again would be that VSC_3 and VSC_4 are in PC mode and acting as load. A VSC in DVC mode is not a risk from stability point of view due to the fact that $\mathrm{re}[y_1] > 0$ for $\omega_2^{\mathrm{r}} = 2.4$ pu. A similar test as the one corresponding to Fig. 6.10 is performed with VSC_1 in DVC mode, $\alpha_{\mathrm{f1}} = 4$ pu and SCR=5. The other VSCs are in PC mode. Figure 6.15 shows the obtained results and it proves that the system remains stable. It is interesting to note that, with the same setup, but with the first dc-network configuration, instability would have occurred from both fronts, i.e. resonance 1 and 2.

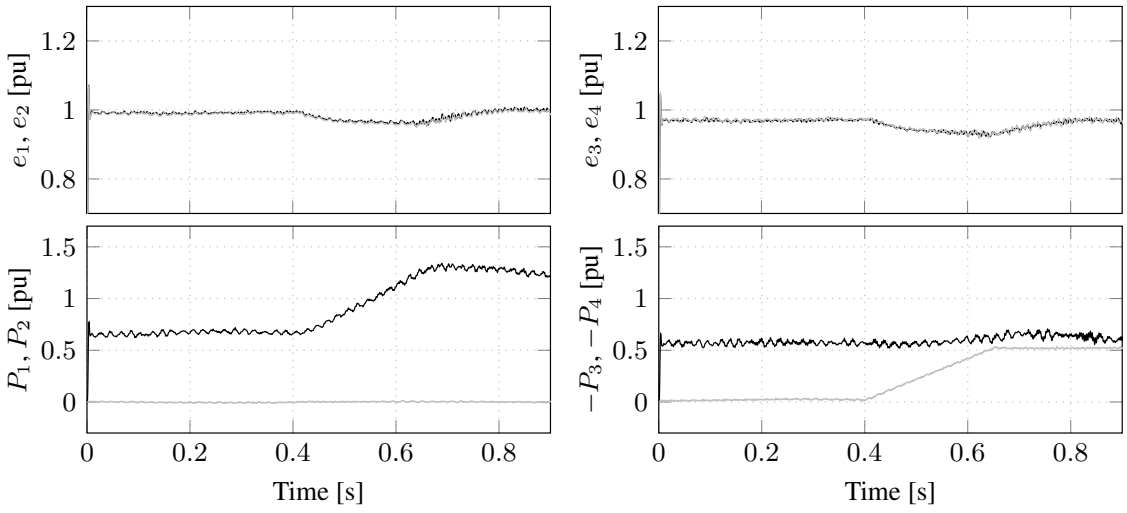

Figure 6.15: Second dc-network configuration. Test for PF sequence 2. VSC_1 is in DVC mode, while VSC_2, VSC_3 and VSC_4 are in PC mode. In VSC_1, SCR=5 and $\alpha_{\mathrm{f1}} = 4$ pu. Black curves: e_1, e_3, P_1, P_3. Gray curves: e_2, e_4, P_2, P_4.

In the third dc-network configuration all the OHLs are replaced by cables. It can be seen from Figure 6.5 and Table 6.2 that the RPs are much smaller compared to the previous cases. This indicates that the instability risk is very low for this network configuration. As an example, Figure 6.16 shows a test considering PF sequence 1 for this configuration and it can be seen that the system reaches the final power setpoints without losing stability. All the PF sequences mentioned earlier has been tested, along with some others, and this system has been always found stable, thus no more results are shown for this configuration.

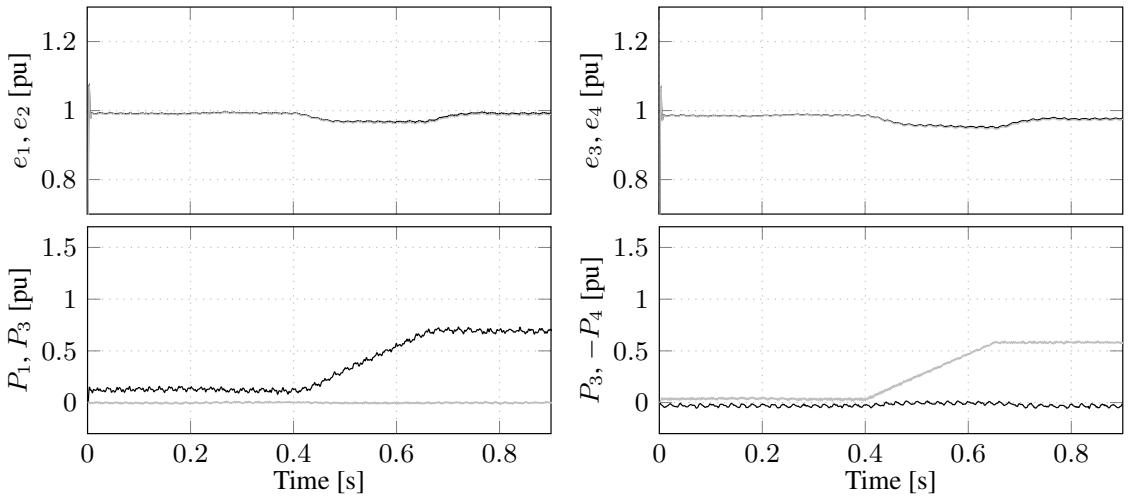

Figure 6.16: Third dc-network configuration. Test for PF sequence 2. VSC_1 is in DVC mode, while VSC_2, VSC_3 and VSC_4 are in PC mode. In VSC_1, SCR=5 and $\alpha_{\text{fl}} = 4$ pu. Black curves: e_1, e_3, P_1, P_3. Gray curves: e_2, e_4, P_2, P_4.

6.6 Conclusions

In this chapter, the theoretical findings presented in the previous analysis, with regards to dc-network stability in MTDC systems, have been verified through laboratory tests in RTDS. In this regard, a four-terminal HVDC system has been implemented in RTDS with two VSCs driven by an external DSP. With this setup, stability analysis has been performed using the method proposed in Chapter 5 under various scenarios. For the first studied dc-network configuration, two resonances are found from the frequency response of the z_{ii}-terms obtained from the RTDS dc-network model. Using (5.24), it has been deduced theoretically that VSC_1 and VSC_2 are implicated on the instability related to the first resonance (RF of 1.8 pu), while VSC_3 and VSC_4 are with the second resonance (RF of 2.0 pu). The tests performed in RTDS confirm these theoretical conclusions since, for the first resonance, oscillations are more pronounced in voltages e_1 and e_2, and consistent results are obtained for the second resonance. Regarding the first resonance, the analysis has shown that instability is mainly introduced by a negative $\text{re}[y_i]$ of the DVC-VDC, i.e. VSC_1. Then, it has been suggested that the stability can be improved by decreasing the speed of the LPF implemented in the DVC-VSC controller. Corresponding tests are performed in RTDS and it is found that the system turns stable with a slower LPF. Furthermore, it has been shown that VSC_1 in DVC mode and connected to a weaker ac system (SCR $= 3$) does not introduce instability. This is due to the fact that, in this case, resonances do not coincide with a negative $\text{re}[y_i]$. Likewise, it has been concluded that turning VSC_3 to DVC mode does not improve the system stability with respect to the first resonance, as argued in Section 6.4.4. Verifications in RTDS have confirm these theoretical statement. Finally, the theoretical analysis shows that unstable cases were less likely to occur in dc-network configurations 2 and 3 and this is confirmed with tests in RTDS.

Chapter 7

Conclusions and future work

In this thesis, dc-network stability of VSC based-HVDC grids has been thoroughly investigated. Preliminary investigations have been performed through time domain simulations in a point-to-point HVDC system. The simulation results show that resonance related instability takes place when the VSC that controls the dc-bus voltage injects power into the transmission link. Moreover, it has been found that the instability is related to the dc-network resonance. Eigenvalue analysis has been applied to theoretically confirm the findings in the time domain simulations.

Although eigenvalue analysis is a powerful tool to study the system stability, it does not give a clear insight on the causes of the detected instability. This has been achieved through the method presented in this thesis. In this method, a point-to-point VSC-HVDC system is divided into two subsystems, and modelled as a single-input single-output feedback system where the passivity properties of each system can be separately studied. The dc-network subsystem has been defined, which is, in practice, the impedance seen from the point where the VSC that controls the dc-bus voltage (DVC-VSC) is connected. The main characteristic of this subsystem is the presence of resonances and that it is a passive system. On the other hand, it has been found that the VSC subsystem, whose frequency response is named dc-side Power Dependent Admittance (PDA), is not passive in the whole frequency range in some conditions, or, in other words, when the dc-side Power Dependent Conductance (PDC) becomes negative. It has been concluded then that unstable cases took place when the dc-network resonance coincides with a negative dc-side PDC. Physically, this can be interpreted as follows: if a dc-network resonance finds a positive conductance, then the resonance is damped. On the other hand, if the resonance finds a negative conductance there is a risk that it is amplified. Moreover, it has been identified that the more negative the dc-side PDC, the greater the risk of instability.

Since the sign of the dc-side PDC is one of the main causes of instabilities, the factors that turn the dc-side PDC negative have been investigated. It has been found that the dc-side PDC becomes negative, primarily, when the corresponding DVC-VSC injects power into the transmission link. Weak ac systems to which DVC-VSCs are connected have a negative impact on the dc-side PDC since, the weaker the ac system, the more negative the dc-side PDC. Control system delays are also found to have an influence on the dc-

side PDC. Including time delays into the model leads to turning more negative the dc-side PDC, but only at specific frequency ranges. Thus, in order to decrease the risk of instability, it is suggested to manipulate the VSC transfer function in order to guarantee a positive dc-side PDC (or, at least, in order to increase it) for frequencies around the dc-network Resonance Frequency (RF). This can be achieved through decreasing the gains of the DC bus Voltage Controller (DVC) and preprocessing the dc-bus voltage through notch filters, for example. The implemented measures are tested through simulations and their effectiveness in mitigating the instability has been shown.

Theoretically derived dc-side PDAs have been compared to measurements in EMT models and the results have shown good agreements. This means that, if a theoretical dc-side PDA cannot be derived due to non availability of information, measurements can be performed in black box models to obtain the VSC dc-side PDA. The advantage of performing stability analysis through either calculating or measuring the dc-side PDA instead of traditional extensive simulation studies is that the dc-side PDA can be obtained performing simulations in one single VSC, which saves considerable amount of simulation time.

Through Nyquist stability criterion, it has been found that the dc-side Resonance Peak (dc-side RP) of the dc-network subsystem also plays an important role on the system stability. The dc-side RP, in fact, provides a measure of the maximum size that the dc-side PDA must have in order to avoid instability. A stability condition has been provided and it states that, if the dc-side PDC is negative, the dc-side PDA magnitude must be less than the inverse of the dc-side RP. Then, different dc-network configurations have been investigated in order to determine their impact on the dc-side RP. It has been found that lumped-parameter TL models lead to lower RPs compared to distributed-parameter TL models. This means that studies performed with lumped-parameter TL models will lead to conservative measures, where the mitigation of a certain stability might not be critical in reality. Thus, in order to obtain more realistic results, the use of distributed parameter TL models are recommended. Moreover, it has been found that including OHL, as well as dc-side filters, in the dc-network configuration increase the dc-side RP, thereby increasing the risk of instability. Therefore, with regards to dc-network stability especial attention must be paid to dc-networks that are composed of large amounts of OHLs.

The method presented for the point-to-point VSC-HVDC system has been extended to MTDC systems. In this case, the dc-network has been modelled as one subsystem while each VSCs connected to this dc-network as other subsystems. The expression that defines the dc-network subsystem is, in practice, the dc-network impedance $\mathbf{Z}$, and, from it, $\mathbf{Z}$-terms have been defined. The advantage of these $\mathbf{Z}$-terms is that they show the contribution of each VSC connected to the dc-network to the system stability. For example, two different terminals can have a resonance with the same RF and different RP. In this case, the VSCs connected to these two terminals contribute to the system stability. The level of contribution depends on the RP at each terminal, meaning that the VSC associated to a terminal with a the greatest RP has the greatest impact on the system stability. Moreover, the $\mathbf{Z}$-terms also show that different resonances can take place at different sets of terminals. These conclusions are observed in the four-terminal HDVC system investigated in this thesis, one resonance characteristic is associated to terminals 1 and 2, while another one is associated to terminals 3 and 4. Then, instability associated with the first resonance can be only

triggered by VSCs connected to terminals 1 and 2 and that VSCs connected to terminal 3 and 4 have negligible impact on the stability related to this first resonance. $\mathbf{Y}$-terms have been also defined and, similarly to the point-to-point HVDC system case, these terms can be seen as admittances and if their conductances are negative, then, there is a risk of instability. The presence of the two different resonance phenomena identified theoretically in the studied four-terminal HVSC system is confirmed through EMT simulations and Real Time Digital Simulator (RTDS) tests. In both verification tools, it has been observed that when the first resonance is triggered, voltage oscillations are more pronounced in terminals 1 and 2, as compared with terminals 3 and 4. Analogous results have been obtained for the second resonance. In the case of the first resonance related instability, one recommended solution from the theoretical analysis is to increase the "terminal conductance." This is achieved by decreasing the bandwidth of the low pass filter (to $\alpha_{\mathrm{fl}} = 1$ pu) located in the vector current controller of VSC_1. The EMT simulations show that this indeed turns the system stable. Regarding the second resonance, the theoretical analysis suggests that one solution to turn the system stable is to switch VSC_3 intro dc-bus voltage droop control, and this is confirmed through simulations. Similar cases and mitigation measures have also been tested in RTDS and consistent results are obtained.

Finally, aside from identifying the main causes of instabilities in dc-networks, the outcome of this study provides the following guidelines to perform dc-network stability studies in HVDC grids:

1. The dc-network has to be modelled, preferably, with distributed parameter models. This models are usually available to transmission system operators responsible for the operation of the HVDC grid. With these models, RFs and RPs at each terminal can be determined. These quantities will tell us at which frequencies especial attention should be paid for the design of a VSC system;

2. DC-side PDAs, or y_i-terms must be obtained. If information is fully available, the best choice is to derive the dc-side PDA or the y_i-terms mathematically. Otherwise, they can be obtained through measurements in black box models. Once the dc-side PDC or y_i-terms are obtained, they should be compared with the corresponding dc-network RFs and RPs;

3. The steps provided presented in this thesis to check the system stability can be applied, and mitigation measures can be implemented if necessary.

Moreover, the main advantage of the method presented in this thesis is that, by defining individual subsystems, the system components that cause instability can be identified. Thus, developing mitigation measures can be focused only onto these components. In fact the analysis results provide useful information for the stability analysis in MTDC systems. They tell us which VSCs are likely to "cooperate" to the system stability and to what extent.

7.1 Future work

To the best of author's knowledge, one of the main contribution of this thesis has been the definition of the $\mathbf{Z}$-terms. A next step in this line is to characterize these $\mathbf{Z}$-terms for other configurations such as meshed grids, combination of meshed and radial, etc. For instance, it can be seen in Chapter 5 that, usually, the magnitude of the $\mathbf{Z}$-terms decreases with the increase of the order of the matrices that defines them. However, this has not been generalized in this thesis. Gaining knowledge on when to neglect higher order $\mathbf{Z}$-terms will facilitate the analysis since the stability condition could be simplified to (5.24). Thus, only the impedances seen from the terminal where a VSC is connected is needed (not the full impedance matrix) together with the VSC subsystems frequency responses around the resonance frequency. Furthermore, dc/dc converters are expected to be part of dc-networks, which are not passive but "active" components. Therefore, the impact on the system stability of such converters should be investigated.

Moreover, in this work, the vector current controller method has been implemented for VSCs. Further analysis can be performed for other controller structures such as stationary frame controllers, power synchronizing controllers, etc, in order to determine what control strategy performs more favourable in the presence of dc-network resonances. In addition, the mitigation measures applied in this thesis have been to pre-process the feedback dc-bus voltage through LPF or notch filters. The disadvantage of these methods is that, if the dc-network changes, the filters will be ineffective until they are re-tuned. Thus, other alternatives, such as adaptive filters, should be investigated in order to provide "plug and play" features to VSCs willing to connect to an existing dc-network.

Experimental verifications are needed in order to give more strength to the findings pointed out in this thesis. In particular, the measurement of dc-side PDA in a physical converter is important since this might help on devising connection requirements for new VSCs that are to be connected to a dc-network. $\mathbf{Y}$-terms can be requested from manufacturers so that it can be shown that a negative dc-side PDC do not coincide with dc-network resonances.

References

[1] U. Axelsson, A. Holm, C. Liljegren, K. Eriksson, and L. Weimers, "Gotland HVDC Light Transmission - World's First Commercial Small Scale dc Transmission," in *CIRED, 15th International Conference and Exhibition on Electricity Distribution*, Nice, France, 1-4, 2010.

[2] ABB, "It is time to connect-Technical description of HVDC Light Technology," Dec. 2012.

[3] Alstom, *Think Grid-Sharing Alstom Grid Innovation and Practices*. Technical Magazine, no. 8, Spring/Summer, 2011.

[4] B. Jacobson, P. Karlsson, G. Asplund, L. Harnefors, and T. Jonsson, "VSC-HVDC Transmission with Cascaded Two-Level Converters," in *Cigré Session*, Paris, France, Aug.22–27, 2010.

[5] B. Gemmell, J. Dorn, D. Retzmann, and D. Soerangr, "Prospects of Multilevel VSC Technologies for Power Transmission," in *Transmission and Distribution Conference and Exposition*, Milpitas, CA, Apr.21–24, 2008.

[6] ABB, "It is time to connect-Technical description of HVDC Light Technology," Mar. 2008.

[7] E. K. amd M. Hyttinen, "Challenges on the Road to an Offshore HVDC Grid," in *Nordic Win d Power Conference*, Bornholm, Denmark, 10–11, 2009.

[8] G. Asplund, B. Jacobson, and K. L. B. Berggren, "Continental overlay HVDC-grid," in *Cigré Session*, Paris, France, Aug. 22–27, 2010.

[9] A. L'Abbate, G. Migliavacca, U. Häger, C. Rehtanz, S. Rüberg, H. Ferreira, G. Fulli, and A. Purvins, "The role of facts and HVDC in the future paneuropean transmission system development," in *9th IET International Conference on AC and DC Power Transmission*, London, UK, Oct. 19-21, 2010.

[10] D. Van Hertem, M. Ghandhari, and M. Delimar, "Technical Limitations towards a SuperGrid - A European Prospective," in *IEEE International Energy Conference and Exhibition (EnergyCon)*, Manama City, Baharain, Dec. 18-22, 2010.

[11] N. Ahmed, A. Haider, D. Van Hertem, L. Zhang, and H. Nee, "Prospects and Challenges of Future HVDC SuperGrids with Modular Multilevel Converters," in *14th*

European Conference on Power Electronics and Applications, Birmingham, UK, Aug.30, 2011.

[12] A. Noman, S. Norga, H. Nee, A. Haider, D. Van-Hertem, L. Zhang, and L. Harnefors, "HVDC SuperGrids with modular multilevel converters — The power transmission backbone of the future," in *9th International Multi-Conference on Systems, Signals and Devices (SSD)*, Chemnitz, Germany, Mar. 20–23, 2012.

[13] 50 HERTZ, Energinet.dk, and Svenska Kraftnät, "Kriegers Flak Combined Grid Solution Feasibility Study," Feb. 2010. [Online]. Available: http://www.50hertz.com/en/file/2010-02-24_Final_Feasibility_Study_Public.pdf

[14] H. Latorre, "Modeling and Control of VSC-HVDC Transmissions," Ph.D. dissertation, Department of Electrical Engineering, Royal Institute of Technology, Stockholm, Sweden, Apr. 2011.

[15] M. Beza, "Control of Energy Storage Equipped Shunt-Connected Converter for Electric Power System Stability Enhancement," Ph.D. dissertation, Department of Energy and Environment, Chalmers University of Technology, Jan. 2015.

[16] L. Harnefors, M. Bongiorno, and S. Lundberg, "Input Admittance Calculation and Shaping for Controlled Voltage-Source Converters," *IEEE Trans. on Industrial Electronics*, vol. 54, no. 6, pp. 3323–3334, Dec. 2007.

[17] L. Harnefors, M. Bongiorno, and S. Lundberg, "Stability Analysis of Converter-Grid Interaction using the Converter Input Admittance," in *European Conference on Power Electronics and Applications*, Aalborg, Denmark, Sep.2–5, 2007.

[18] L. Tang, "Control and protection of multi-terminal dc transmission systems based on voltage-source converters," Ph.D. dissertation, University of McGill, Montreal, Québec, Canada, Jan. 2003.

[19] A. Emadi and M. Ehsani, "Multi-Converter Power Electronic Systems: Definition and Applications," in *Power Electronic Specialist Conference*, Vancouver, BC, Jun.17–21, 2001.

[20] A. Emadi, M. Ehsani, and J. M. Miller, *Vehicular Electric Power Systems: Land, Sea, Air, and Space Vehicles*. CRC Press, Dec.12, 2003.

[21] A. Emadi, A. Khaligh, C. Rivetta, and G. Williamson, "Constant power loads and negative impedance instability in automotive systems: definition, modeling, stability, and control of power electronic converters and motor drives," *IEEE Transactions on Vehicular Technology*, vol. 55, no. 4, pp. 1112–1125, Jul. 2006.

[22] A. Kwasinski and C. N. Onwuchekwa, "Dynamic Behavior and Stabilization of DC Microgrids With Instantaneous Constant-Power Loads," *IEEE Trans. On Power Electronics*, vol. 26, no. 3, pp. 822–834, Mar. 2011.

[23] J. R. LeSage, R. G. Longoria, and W. Shutt, "Power System Stability Analysis of Synthesized Complex Impedance Loads on an Electric Ship," in *IEEE Electric Ship*

Symposium, Alexandria, VA, Apr.10–13, 2011.

[24] S. Sudhoff, S. Glover, P. Lamm, D. Schmucker, and D. Delisle, "Admittance space stability analysis of power electronic systems," *IEEE Transactions on Aerospace and Electronic Systems*, vol. 36, no. 3, pp. 965–973, Jul. 2000.

[25] S. Sudhoff and S. Glover, "Stability analysis methodologies for dc power distribution systems," in *Proceedings of the 13th international Ship Control System Symposium*, Orlando, FL, Apr. 7–9, 2003.

[26] P. Rault, F. Colas, X. Guillaud, and S. Nguefeu, "Method for small signal stability analysis of VSC-MTDC grids," in *IEEE PES General Meeting*, San Diego, CA, Jun. 22–26, 2012.

[27] G. Kalcon, G. P. Adam, O. Anaya-Lara, S. Lo, and K. Uhlen, "Small-signal stability analysis of multi-terminal VSC-based dc transmission systems," *IEEE Trans. on Power Systems*, vol. 27, no. 4, pp. 1818–1830, Nov. 2012.

[28] A. S. A. M. Alsseid, D. Jovcic, "Small Signal Modelling and Stability Analysis of Multiterminal VSC-HVDC," in *European Conference on Power Electronics and Applications*, Birmingham, UK, Aug.30, 2011.

[29] F. Thams, J. Suul, S. D'Arco, M. Molinas, and F. Fuchs, "Stability of DC voltage droop controllers in VSC HVDC systems," in *PowerTech*, Eindhoven, Netherlands, Jun. 29–Jul 2, 2015.

[30] M. Zadeh, M. Amin, J. Suul, M. Molinas, and O. Fosso, "Small-Signal Stability Study of the Cigre DC Grid Test System with Analysis of Participation Factors and Parameter Sensitivity of Oscillatory Modes," in *Power System Computation Conference*, Wroclaw, Poland, Aug. 18–22, 2014.

[31] J. Beerten, S. D'Arco, and J. Suul, "Frequency-dependent cable modelling for small-signal stability analysis of VSC-HVDC systems," *IET Generation, Transmission and Distribution*, vol. 10, no. 6, pp. 1370–1381, May 2016.

[32] J. Beerten, S. D'Arco, and J. Suul, "Identification and Small-Signal Analysis of Interaction Modes in VSC MTDC Systems," *IEEE Trans. on Power Delivery*, vol. 31, no. 2, pp. 888–897, Apr. 2016.

[33] J. Sun, "Autonomous Local Control and Stability Analysis of Multiterminal DC Systems," *IEEE Journal of Emerging and Selected Topics in Power Electronics*, vol. 3, no. 4, pp. 1078–1089, Dec. 2015.

[34] E. Prieto-Araujo, A. Egea-Alvarez, S. Fekriasl, and O. Gomis-Bellmunt, "DC voltage droop control design for multi-terminal HVDC systems considering AC and DC grid dynamics," *IEEE Trans. on Power Delivery*, vol. 31, no. 2, Apr. 2016.

[35] W. Wang, M. Barnes, O. Marjanovic, and O. Cwikowski, "Impact of DC Breaker Systems on Multiterminal VSC-HVDC Stability," *IEEE Transactions on Power Delivery*, vol. 31, no. 2, pp. 769–779, Apr. 2016.

[36] G. Pinares, "On the Analysis of DC Network Dynamics of VSC-based HVDC Systems," Licentiate of Engineering thesis, Department of Energy and Environment, Chalmers University of Technology, Gothenburg, Sweden, Apr. 2014.

[37] I. Mattsson, A. Ericsson, B. Railing, J. Miller, B. Williams, G. Moreau, and C. Clarke, "Murray Link-The longest underground HVDC cable in the world," in *Cigré conference*, Paris, France, Aug. 2004.

[38] L. Harnefors and H.-P. Nee, "A General Algorithm for Speed and Position Estimation of AC Motors," *IEEE Trans. on Industrial Electronics*, vol. 47, no. 1, pp. 77–83, Feb. 2000.

[39] L. Ängquist and M. Bongiorno, "Auto-normalizing Phase-Locked Loop for Grid-connected Converters," in *Energy Conversion Congress and Exposition*, San Jose, CA, Sep.24–29, 2009.

[40] L. Harnefors and H.-P. Nee, "Model-based current control of ac machine using the internal model control method," *IEEE Trans. on Industry Applications*, vol. 34, no. 1, pp. 133–141, Jan. 1998.

[41] L. Zhang, "Modeling and Control of VSC-HVDC Links Connected to Weak AC Systems," Ph.D. dissertation, Royal Institute of Technology, Stockholm, Sweden, Apr. 2010.

[42] G. Pinares, "Analysis of the dc dynamics of VSC-HVDC systems connected to weak ac grids using a frequency domain approach," in *Power Systems Computation Conference PSCC*, Aug. 18–22, 2014.

[43] MathWorks, "Documentation of control system toolbox." [Online]. Available: http://www.mathworks.se/help/control/ref/setdelaymodel.html

[44] J. Koppinen and M. Hinkkanen, "Impact of the switching frequency on the dc-side admittance in three-phase converter systems," in *16th European Conference on Power Electronics and Applications (EPE'14-ECCE Europe)*, Lappeenranta, Finland, Aug. 26–28 2014, pp. 1–10.

[45] L. Xu, L. Fan, and Z. Miao, "DC impedance-model-based resonance analysis of a VSC-HVDC system," *IEEE Transactions on Power Delivery*, Nov. 2014.

[46] G. Pinares, L. A. Tuan, L. Bertling-Tjernberg, and C. Breitholtz, "Analysis of the dc dynamics of VSC-HVDC systems using a frequency domain approach," in *IEEE Asia Pacific Power and Energy Conference*, Hong Kong, China, Dec. 8–11, 2013.

[47] J. Slotine and W. Li, *Applied Nonlinear Control*. Prentice Hall, 1991.

[48] T. Glad and L. Ljung, *Control theory – Multivariable and Nonlinear Methods*. CRC PRess, 2000.

[49] V. Blasko, V. Kaura, and W. Niewiadomski, "Sampling methods for discontinuous voltage and current signals and their influence on bandwidth of control loops of electric drives," in *Applied Power Electronics Conference and Exposition*, Atlanta, GA,

Feb. 23–27, 1997.

[50] ABB, "XLPE Land Cable Systems, Rev. 5." [Online]. Available: https://library.e.abb.com/public/ab02245fb5b5ec41c12575c4004a76d0/XLPE%20Land%20Cable%20Systems%202GM5007GB%20rev%205.pdf

[51] C. F. Kumru, C. Kocatepe, and O. Arikan, "An investigation on electric field distribution around 380 kv transmission line for various pylon models," *International Journal of Electrical, Computer, Energetic, Electronic and Communication Engineering*, vol. 9, no. 8, pp. 138 – 141, 2015. [Online]. Available: http://iastem.com/Publications?p=104

[52] G. Pinares and M. Bongiorno, "Modeling and analysis of VSC-based HVDC systems for dc network stability studies," *IEEE Trans. on Power Delivery*, vol. 31, no. 2, pp. 848–856, Apr. 2016.

[53] Manitoba HVDC Research Centre, *PSCAD On-Line Help System*, Oct. 2010.

[54] G. Pinares, L. Bertling, T. A. Le, and C. Breitholtz, "On the analysis of the dc dynamics of multi-terminal VSC-HVDC Systems using small signal modeling," in *IEEE PowerTech Conference*, Grenoble, France, Jun.16-20, 2013.

[55] S. Skogestad and I. Postlethwaite, *Multivariable Feedback Control*. John Wiley & Sons, Ltd, 2005.

[56] S. Xu, M. Darouach, and J. Schaefers, "Expansion of det(A+B) and Robustness Analysis of Uncertain State Space Systems," *IEEE Trans. on Automatic Control*, vol. 38, no. 11, pp. 1671–1675, Nov. 1993.

[57] J. J. Grainger and W. D. Stevenson, *Power System Analysis*. McGraw-Hill Book Co., 1994.

[58] Texas Instruments, "TMS320F28335, TMS320F28334, TMS320F28332, TMS320F28235, TMS320F28234, TMS320F28232 Digital Signal Controllers (DSCs) Data Manual," Jun. 2007. [Online]. Available: http://www.ti.com/lit/ds/sprs439m/sprs439m.pdf

[59] G. Pinares and M. Bongiorno, "Definition of a voltage-source converter dc-side admittance and its impact on dc-network stability," in *International Conference on Power Electronics (ECCE-Asia)*, Seoul, South Korea, 1–5, 2015, pp. 2072–2078.